

Characterisation of a palaeovalley system in
Anangu Pitjantjatjara Yankunytjatjara (APY) Lands
of South Australia using
ground-based hydrogeophysical methods

Aaron Davis, Brady Flinchum, Tim Munday, Kevin Cahill,
Luk Peeters, Jorge Martinez, Teagan Blaikie,
Mat Gilfedder and Tania Ibrahimi

Goyder Institute for Water Research
Technical Report Series No. 20/05



Goyder Institute for Water Research Technical Report Series ISSN: 1839-2725

The Goyder Institute for Water Research is a partnership between the South Australian Government through the Department for Environment and Water, CSIRO, Flinders University, the University of Adelaide, and the University of South Australia. The Institute enhances the South Australian Government's capacity to develop and deliver science-based policy solutions in water management. It brings together the best scientists and researchers across Australia to provide expert and independent scientific advice to inform good government water policy and identify future threats and opportunities to water security.



This project was also supported by CSIRO's Deep Earth Imaging Future Science Platform.

Enquires should be addressed to: Goyder Institute for Water Research
Level 4, Rundle Mall Plaza, 50 Rundle Mall,
Adelaide, SA 5000
tel: 08 8313 5020
e-mail: enquiries@goyderinstitute.org

Citation

Davis, A., Flinchum, B., Munday, T., Cahill, K., Peeters, L., Martinez, J., Blaikie, T., Gilfedder, M., and Ibrahim, T. (2020) *Characterisation of a palaeovalley system in Anangu Pitjantjatjara Yankunytjatjara (APY) Lands of South Australia using ground-based hydrogeophysical methods*. Goyder Institute for Water Research Technical Report Series No. 20/05.

© Crown in right of the State of South Australia, Department for Environment and Water.

Disclaimer

The CSIRO as the project partner, advises that the information contained in this publication comprises general statements based on scientific research and does not warrant or represent the completeness of any information or material in this publication. The project partners do not warrant or make any representation regarding the use, or results of the use, of the information contained herein about to its correctness, accuracy, reliability, currency or otherwise and expressly disclaim all liability or responsibility to any person using the information or advice. Information contained in this document is, to the knowledge of the project partners, correct at the time of writing.

Contents

Acknowledgments	viii
1 Introduction and overview	1
1.1 Introduction	1
1.2 Previous ground geophysical studies for palaeovalleys in the Musgrave Province	2
1.3 Overview and aim	2
2 Study area	3
2.1 Climate	3
2.2 Geology	3
2.3 Hydrogeology	5
3 Ground-based hydrogeophysical methods	10
4 Active seismic method	11
4.1 Methods	11
4.2 Field data acquisition	19
4.3 Results	20
4.4 Data synthesis	25
5 Borehole nuclear magnetic resonance (BNMR)	29
5.1 Borehole nuclear magnetic resonance technology	29
5.2 Borehole nuclear magnetic resonance inversion	32
Hydraulic permeability	32
5.3 Field data acquisition	33
5.4 Borehole nuclear magnetic resonance interpretation	35
6 Time domain electromagnetics (TDEM)	48
6.1 The ground time domain electromagnetic (TDEM) method	48
6.2 Time domain electromagnetic (TDEM) workflow	49
6.3 Field data acquisition	50
6.4 Time domain electromagnetic inversion	54
6.5 Time domain electromagnetic interpretation	55
7 Discussion and conclusions	57
References	59

Figures

Figure 1. Location of boreholes and ground geophysical traverse across the Lindsay East Palaeovalley and its tributaries which were the focus for this study.....	4
Figure 2. Pseudocoloured airborne magnetics total magnetic Intensity (TMI) image modulated by intensity variations from the 1 st vertical derivative of the magnetics data for the study area.	6
Figure 3. Interpreted basement geology in study area overlain on image of 1 st vertical derivative magnetics.	7
Figure 4. Pseudocoloured airborne electromagnetic (AEM) conductivity-depth interval (50-60 m) modulated in intensity by the 1 st vertical derivative of the airborne magnetics. The main linear conductive feature runs north to south and comprises conductive valley fill within the Lindsay East Palaeovalley (see also Figure 1). The correspondence between the orientation of the palaeovalley fill and structure (de-magnetised zones represented as dark areas in the image) is apparent.	8
Figure 5. Interpreted surface regolith geology in the study area. Source: Krapf .et al. (2012).	9
Figure 6. The layout of equipment employed in a refraction seismic survey, illustrating ray paths of direct and critically refracted P-waves through the subsurface. For this study the P-wave source energy was generated by a Propelled Energy Generator 40 kg (PEG-40) accelerated weight drop mounted on the rear end of a field 4WD. The seismic response was recorded by Geode seismic recorders (Figure adapted from Goodwin et al. (2017)).	12
Figure 7. A shot from 912 m along the main profile showing the first arrival picks. These picks are done manually for each shot in the survey. If the trace is too noisy a pick is not made.	13
Figure 8. (a) Theoretical drawing demonstrating a common midpoint (CMP) gather. A single shot gather is shown in magenta, where energy is reflected of a boundary between the source and all the receivers. With many shots it is possible to collect all source and receiver pairs that share a common midpoint. A supergather can be created by combining any number of adjacent CMP locations. (b) The stacking chart used to design the survey geometry for these data. The CMP fold of the data set is presented in the diagonal space. Colors represent increasing CMP locations.	15
Figure 9. Common midpoint (CMP) fold of the data. The maximum fold possible is 58. The higher the fold the higher the signal-to-noise.	16
Figure 10. This figure shows the impact of using supergathers. (A) common depth point (CDP) from 1254 m; (B) Supergather from the same location (including two adjacent CMPs); (C) Supergather from (B) which has been filtered to remove surface wave noise.....	16
Figure 11. Two-way travel time of the picked reflection (with aid of semblance plot) coloured by the moveout velocity. Note the continuity between gathers.	18
Figure 12. The normal move out (NMO) velocity plotted for each common depth point (CDP) number. The black dots are the raw moveout velocity and the grey line is a smoothed out version that was used for the moveout and stacking. Red vertical lines indicate the supergathers shown in Figure 13.	18
Figure 13. Supergathers from common depth point (CDP) number 4650 (left), and CDP 12540 (right). The red dashed line shows the moveout curve from the velocity profile shown in Figure 12.	19
Figure 14. Location of the seismic surveys. (a) Underlying 10 m elevation data from Shuttle Rader Topographic Mission (SRTM). Overlaid on top of the elevation map is a conductivity depth section from 60-70 m below the surface. Electrical conductivity values greater than 55 $\mu\text{S}/\text{m}$ are marked out to highlight the palaeovalley location. The airborne data were inverted using 400x400 m pixels, but a minimum curvature interpolation was applied for visualisation. The seismic profile running perpendicular to the channel was collected from southeast to northwest because we were required to shoot along the road. The yellow circles represent starts of profiles where the reference locations is near the centre of the palaeovalley and is marked accordingly. (b) Image of a geometrics Geode and cable	

along the side of the road. The image is taken looking toward the northwest. (c) Image of the PEG and steel plate used as the source. Here it is shown mounted onto the CSIRO vehicle and the 40 kg weight drop is fully extended.....20

Figure 15. (a) First-arrival picks for the entire data set. Each roll is highlighted by a rectangular box. In an ideal and noise-free environment the entire rectangle would be filled. This highlights the generator noise on Roll -1. The cooler colours represent shorter travel times and the warmer colours are longer travel-times. (b). Plot of the reciprocal travel-times. This is calculated by comparing the travel time at a geophone where the shot and receiver are reversed. In an ideal and noise-free environment all the picks should lie on a 1:1 line. This plot shows that overall the data quality is very good.....21

Figure 16. P-wave velocity. (a) Results for the entire seismic refraction profile shown with no vertical exaggeration. The gap in the line was due to a corner that we were uncomfortable operating on because of road traffic the location of the drill holes has been plotted for reference. The thick part at the bottom of DH-1 and DH-2 is where the log marked, "Weathered granitic rock, possibly gneissic. Coarse to very coarse-grained quartz sand sized fragments and kaolinitic clay". Panels b-e are shown so that more details can be observed. Y-axis scale for all panels is in metres (i.e. all of these panels are shown with no vertical exaggeration); (b) The first short profile; (c) -90–532 m; (d) 532–1154 m; (e) 1154–1776 m.....22

Figure 17. P-wave velocity, re-scaled to emphasise the shallow high velocity structures. (a) Results for the entire seismic refraction profile are shown with no vertical exaggeration (Y-axis units are in metres). The gap in the line was due to a corner that we were uncomfortable operating on because of road traffic the location of the drill holes are plotted for reference. The thick part at the bottom of DH-1 and DH-2 is where the drill-log marked "Weathered granitic rock, possibly gneissic. Coarse to very coarse-grained quartz sand sized fragments and kaolinitic clay". Panels b–e show sub-survey details; (b) The short profile; (c) -90–532 m; (d) 532–1154 m; (e) 1154–1776 m.....23

Figure 18. a) Seismic reflection results for the entire profile shown with no vertical exaggeration. Note that these are depth converted sections using a picked velocity model and uncertainty is probably +/- 5–7 m in the vertical direction. Panels (b) to (e) are zoom images so that some detail can be observed. All these sections are shown at zero vertical exaggeration: (b) The short profile. (c) -90–532 m; (d) 532–1154 m; (e) 1154–1776 m.24

Figure 19. (a) Overlay plot showing the seismic refraction (same colour scale as Figure 16) on top of the Seismic reflection results (from Figure 18). All profiles are shown with no vertical exaggeration. A depth to bedrock prediction has been added manually (black solid line) to illustrate the match between the two methodologies; (b) to (e) are zoom images so that more detail can be observed. All these sections are shown at zero vertical exaggeration: (b) the short profile; (c) -90–532 m; (d) 532–1154 m; (e) 1154–1776 m. seismic reflection colour scale.25

Figure 20. (a) Regional map showing 60–70 m depth section with conductivity greater than 45 $\mu\text{S}/\text{m}$ masked out; (b) Perspective view of the palaeo-topography with line location shown at 10x vertical exaggeration. The surface topography has been shifted up for visualisation; (c) Final inset showing the location of seismic line and the two boreholes. Start of the lines are from 0–1701 m and from 0–558 m. This is overlaid on a depth to bedrock map (instead of elevation of ground surface) from the airborne electromagnetics.26

Figure 21. Results from the seismic reflection survey. Data were processed following a basic flow: 1) band-pass filtered, 2) trace normalised, 3) CMP sorted, 4) muted surface waves, 5) NMO moveout applied (one velocity per gather), 6) stacked, and 7) a time to depth conversion was applied using a single velocity. The main reflector (clearly visible in the raw CMP gathers) is highlighted in yellow. The boreholes are shown as black vertical lines. Where the black line gets thicker is where drillers intersected saprolite (*in situ* rock). The blue line is the extracted depth to bedrock value (from airborne electromagnetics) —note the large difference between 1000 and 1250 and -500 and -250 m along the profile.27

Figure 22. Results for the seismic refraction survey. The velocity model was inverted using travel-time tomography and is comprised of ~20,000 picks. Regions that are white have no ray paths passing

through them. The main reflection from (Figure 21) is plotted on the image as a grey line, the blue line is from the AEM data, and the boreholes are shown as in panel a. The match between the strong reflector and strong velocity change means that the depth conversion is done well.27

Figure 23. Preliminary conceptualisation based on the combination of airborne electromagnetics (AEM) and seismic reflection data. The base of the deposited sediments are defined by the AEM data. The saprolite is defined as the region between the reflection boundary and AEM boundary. The saprock/fractured rock is the region that has a lot of reflections. Fresh bedrock was defined by a notable lack of reflections. The biggest difference to the conceptualisation is that the saprolite thickness is not uniform (it is thickest at the edges of the valley and thinnest in the centre).28

Figure 24. Cylindrical shell of uniform magnetic field strength that targets the formations outside the disturbed zone to water content and pore size/porosity (adapted from Vista Clara Inc. 2017).29

Figure 25. Diagram of the spin echo train from a CPMG pulse sequence for nuclear magnetic resonance (NMR) measurement. The time decay measured by the borehole NMR tool is the T2 decay, which is estimated from the peak amplitude of every echo in the spin echo train. Image from: <http://www.iomonitoring.pro/mrphysics.htm>30

Figure 26. Measured, stacked, and filtered T2 decay curve for a borehole nuclear magnetic resonance (NMR) measurement in (black line) and the linear best fit model that is used to fit the decay data (red line).31

Figure 27. Basis function of the exponential decays used in creating the red curve in Figure 26. Note there are two distributions of T2 in the basis set, indicating both bound (left) and mobile (right) water.31

Figure 28. The JD350 borehole nuclear magnetic resonance tool acquires data for four frequencies to obtain measurements away from the disturbed zone. Data from each shell can be combined to improve data quality or they can be examined and interpreted separately. Adapted from Vista Clara Inc. (2017).34

Figure 29. Setting up of the Vista Clara Borehole nuclear magnetic resonance logging tool over DH1a.34

Figure 30. Winch and Borehole nuclear magnetic resonance controller in field data acquisition configuration.35

Figure 31. Borehole nuclear magnetic resonance logging for DH1a2, compared to drilling lithology and an inductive conductivity log. Location of borehole given in Figure 1. Lithology log is sourced from Keppel et al. (2019).37

Figure 32. Borehole nuclear magnetic resonance logging for DH1b, compared to drilling lithology and an inductive conductivity log. Location of borehole given in Figure 1. Lithology log is sourced from Keppel et al. (2019).38

Figure 33. Borehole nuclear magnetic resonance logging for DH1c, compared to drilling lithology and an inductive conductivity log. Location of borehole given in Figure 1. Lithology log is sourced from Keppel et al. (2019).39

Figure 34. Borehole nuclear magnetic resonance logging for DH1d, compared to drilling lithology and an inductive conductivity log. Location of borehole given in Figure 1. Lithology log is sourced from Keppel et al. (2019).40

Figure 35. Borehole nuclear magnetic resonance logging for DH1f, compared to drilling lithology and an inductive conductivity log. Location of borehole given in Figure 1. Lithology log is sourced from Keppel et al. (2019).41

Figure 36. Borehole nuclear magnetic resonance logging for S22i, compared to drilling lithology and an inductive conductivity log. Location of borehole given in Figure 1. Lithology log is sourced from Keppel et al. (2019).42

Figure 37. Lithology log of borehole DH1a with accompanying nuclear magnetic resonance, inductive conductivity and gamma logs. Lithology interpretation from Krapf et al. (2019).43

Figure 38. Comparison between fine scale TinyPerm derived measures of vertical and horizontal hydraulic conductivity (K_v and K_h) shown in the left-hand panel overlain on the borehole nuclear magnetic resonance modelled estimates of K using the Sum of Echoes (SOE) and Schlumberger-Doll Research (SDR) methods. TinyPerm results courtesy of Andy Love (Flinders University of South Australia).	45
Figure 39. The Conductivity-depth sections for the Lindsay East Palaeovalley transect for a smooth 30-layer inversion. Drill hole lithology (adapted from Keppel et al. (2019)) and inductive conductivity logs are overlain on the AEM section in the top panel. Water contents from the borehole nuclear magnetic resonance are overlain on the section in the middle panel and modelled hydraulic conductivity estimates (Schlumberger Doll Research (SDR) and Sum of Echoes (SOE)) are overlain on the section in the lower panel. Adjustments to the predicted lithology textures (whether fining or coarsening upwards) have been made based on the borehole nuclear magnetic resonance logs.....	46
Figure 40. The Conductivity-depth section for airborne electromagnetic line adjacent to bore s22i. The airborne electromagnetic model is a smooth 30-layer inversion. Drill hole lithology (adapted from Keppel et al. (2019)) and inductive conductivity log is overlain on the airborne electromagnetic section in the top panel. Water contents from the borehole nuclear magnetic resonance are overlain on the section in the middle panel and modelled hydraulic conductivity estimates (Schlumberger Doll Research (SDR) and Sum of Echoes (SOE)) are overlain on the section in the lower panel.	47
Figure 41. The principles of a time domain electromagnetic sounding.	48
Figure 42. Schematic representation of the time domain electromagnetic (TDEM) acquisition (A), measurement (B), inversion (C) workflow, with section/traverse of pseudocoloured soundings to aid interpretation (D).	49
Figure 43. Layout of transmitter/receiver loops used in this study.	50
Figure 44. Transmitter current waveform (a) and receiver windows (b) of the NanoTEM electromagnetic system.....	51
Figure 45. Location of NanoTEM survey soundings in the study area. Inset map shows their locations relative to the AEM flightlines.	53
Figure 46. Conductivity-depth model for blocky layered inversion approach.	54
Figure 47. Conductivity-depth models resulting from smoothly constrained 19-layer 1D inversion.	54
Figure 48. Smooth-model conductivity depth section from the inverted NanoTEM soundings (top panel) and the interpreted geology for the transect (lower panel). The geological section was determined from the combined interpretation of the drillhole and the conductivity section data. Geological linework is superimposed on the conductivity-depth soundings for added clarity.	56

Tables

Table 1: Bore name and depth of logging for borehole nuclear magnetic resonance logging.	33
Table 2: Well construction detail for bores logged with borehole nuclear magnetic resonance. Source: Keppel et al. (2019).....	33
Table 3: Coefficients and cut-off times used in borehole NMR processing.	35
Table 4: Locations of ground-based NanoTEM time-domain electromagnetic soundings.	51
Table 5: Window start, end, and centre times for the NanoTEM time-domain electromagnetic system.....	52
Table 6: Layer thicknesses and depths used in 19-layer smooth-model inversions.	55

Executive summary

A regional airborne electromagnetic survey across the Musgrave Province of South Australia identified the presence of a complex palaeovalley system filled with (electrically) conductive alluvial and colluvial materials. Previous hydrogeological investigations have suggested that this system has significant groundwater resource potential, but relatively little is known about its stratigraphy nor of the hydraulic properties and the character of the sediments present. Recent drilling in one of the main palaeovalley trunk systems (the Lindsay East Palaeovalley) provided an opportunity to better understand the aquifers present and how they varied. This also presented an opportunity to characterise these systems from a hydrogeophysical perspective, with the recent drilling providing data to help constrain the interpretation of results generated from the application of different ground and borehole geophysical techniques. Hydrogeophysical methods are increasingly being employed to supplement information about aquifer systems acquired through more conventional and accepted hydrogeological investigations.

This report describes the first stage of an ongoing systematic study to define the merits of different surface and subsurface geophysical technologies to help understand the hydraulic properties of the palaeovalley aquifers in the Musgrave Province and to provide a basis for extending local (point or bore-) scale hydrogeological data to areas where invasive investigative approaches may be difficult whether for access or economic reasons.

The report focuses on the Lindsay East Palaeovalley, where we examine results obtained from a shallow seismic refraction and reflection transect that crossed perpendicular to the valley orientation. The transect also passed close to several bores that were drilled into the sedimentary system for hydrogeological investigation. The bores drilled into the palaeovalley sediments in the main trunk and in a tributary to the main valley were also examined using borehole nuclear magnetic resonance (BNMR) and inductive conductivity tools. Along the same transect as the seismic traverse a set of soundings were also sampled using a ground time domain electromagnetic (TDEM) system optimised for near surface investigations.

The shallow seismic study, involving seismic reflection and refraction, was undertaken to obtain an independent measurement of the location of bedrock and to help elucidate details about the fill within the main palaeovalley. The seismic refraction results show significant variation in the near surface (upper 10 m) velocity structure and a deep (~100 m) refractor that is believed to be the top of bedrock. The seismic reflection results show significant variability, both lateral and vertical, in the top of bedrock reflector and reveal prominent and clear reflections down to depths greater than 400 m. In contrast to the airborne electromagnetic (AEM) data, the seismic data appear to define an interface between weathered and unweathered basement rocks at a depth significantly greater depth. The AEM data may not effectively resolve the boundary between the regolith and the basement in this situation, perhaps because we encounter a limit to its depth of investigation. Nonetheless the AEM data does appear to resolve the depth of the transported regolith, thereby defining the lower limits of the palaeovalley fill aquifer. The seismic data in contrast may define the boundary between the saprock and underlying bedrock. Given that the saprock, the overlying saprolite and the transported sediments above that represent the full aquifer (excluding the fractured rock component) this is also useful information to know.

BNMR results for the bores drilled into the Lindsay East main trunk valley indicate that the finer scale hydraulic properties of the palaeovalley sediments vary significantly vertically and laterally, reflecting the heterogeneity of the sediment package. Free water content in the upper part of the sedimentary sequence appears to be relatively consistent between bores but there is a suggestion that water contents may be slightly lower on the margins of the palaeovalley. The BNMR results supports a model for a higher water yielding layer, which may be relatively thin (<5 m) within the overall aquifer sequence. Results also suggest there are several higher yielding layers at different depths through the sedimentary sequence. Further work is required to test this. Modelled K values from the BNMR are consistent with those determined from aquifer testing, but more detailed testing employing multilevel slug tests (MLST), dipole-flow tests, and/or well bore flow (WBF) logging would be beneficial, and would provide a basis for deriving calibration values for the NMR data. This would then permit the spatial extension of BNMR logging to other parts of the

region to derive more representative information on the hydraulic properties of the alluvial aquifer systems present.

Results from the ground-based time domain electromagnetic (TDEM) methods show a similar conductivity structure for the transect across the Lindsay East Palaeovalley as was observed in the airborne EM data processed and inverted independently. The similarities between the two methods lends support to the effectiveness of the AEM inversion results in defining the conductivity structure associated with the palaeovalleys even though a wide line spacing was employed for the airborne survey. Together the airborne and ground methods support the model for a deeper conductive zone within the central part of the palaeovalley, including sediments comprising the confining mudstones and sandier units above that. The ground TDEM data suggest that a crude indication of the standing water level could be determined by mapping the depth to the top of the first conductive layer; interpreted as being related to a zone of higher salinity through evapotranspiration.

While this study has demonstrated the potential of different hydrogeophysical techniques to elucidate the hydrostratigraphy and nature of the groundwater present in the Lindsay East Palaeovalley system, the value of more systematic studies such as this will only be realised through further hydrological investigations of the aquifers, and through additional combined analysis of the geophysical data.

Acknowledgments

This study was carried out as part of the G-Flows Stage-3 Project. This project was funded jointly by the Goyder Institute for Water Research, and its partner organisations, including: Department for Environment and Water (DEW), Commonwealth Scientific and Industrial Research Organisation (CSIRO), and Flinders University, South Australia (FUSA). Linked to the project was work undertaken by Mark Keppel, Adrian Costar and Kent Inverarity of DEW, and Carmen Krapf of DEM who planned and initiated and interpreted the drilling and borehole geophysics that was instrumental in helping understand and interpret the ground geophysical data acquired. Andy Love (FUSA) provided information on the fine-scale hydraulic measurements of the core.

We acknowledge the support of CSIRO's Deep Earth Imaging Future Science Platform in undertaking this research.

We acknowledge the traditional owners of the Anangu Pitjantjatjara Yankunytjatjara (APY) Lands, the Pitjantjatjara, Yankunytjatjara and Ngaanyatjarra people. We would also like to thank the APY General Manager and the entire APY Executive Board who were supportive of the G-Flows Stage-3 project.

We thank the Goyder Institute Research Advisory Committee members: Kane Aldridge (Goyder Institute), Justin Brookes (The University of Adelaide), Jennie Fluin (DEW), Jim Cox (SARDI), Dirk Mallants (CSIRO), Neil Power (DEW), Darryl Day (ICE WaRM), Craig Simmons (Flinders University), Jacqueline Frizenschaf (SA Water), and Peter Teasdale (UniSA).

We are extremely grateful for the support of a wide range of people, organisations, companies, and departments who all aided help undertake and complete this project.

1 Introduction and overview

1.1 Introduction

Groundwater resources in remote arid areas of South Australia such as the Musgrave Province are the only available water resources to support the livelihood of communities as well as economic development. However, in a setting where knowledge of both groundwater recharge and storage is relatively limited, in part related to the regions aridity but also to a geological setting dominated by crystalline basement at shallow depths covered by extensive transported materials, the extension of our understanding of the groundwater resource potential remains challenged. Over the past two decades several important geological and hydrogeological studies varying from desktop analyses, drilling investigations, geophysical surveys and groundwater quality and resource assessments have taken place. These studies while varying in nature have all contributed to evaluating the opportunities and risks for future groundwater resource development in either isolated parts of the province or across extensive areas. They have also demonstrated that key among the knowledge gaps is an appreciation of the variability of the aquifers present, as well as their characteristics.

Recent airborne geophysical, particularly airborne electromagnetics surveys (see, for example, Soerensen et al. 2018) have indicated the presence of extensive sequences of relatively thick (>100 m) palaeovalley fill which offer potential for significant groundwater resource. With their general location identified, more detailed on-ground investigations are warranted to firm up the understanding of this potential. These investigations include conventional hydrogeological approaches, which could be informed by local hydrogeophysical (surface and borehole) studies to better target areas for drilling and to identify parts of the aquifer that may be higher yielding and or provide better quality water.

To assist this understanding the G-Flows Stage-3 project sought to test several hydrogeophysical methods as a means of informing more conventional hydrogeological studies and helping conceptualise the hydrogeology. In this context, several ground-based geophysical methods are being examined specifically to better understanding the aquifer characteristics that define the palaeovalley systems occurring across the region. It is expected that the techniques examined, and the resulting findings will have application in other areas of South Australia and elsewhere in Australia. More specifically, the work undertaken here considered the application of both surface and borehole geophysical techniques, with the idea that the study area becomes a case-study site for new hydrogeophysical technologies, as and when they emerge. Access to detailed drill hole information (including diamond core and hydraulic testing data (see Keppel et al., 2019) provides an invaluable constraint on interpretation (processing and inversion) methods that can be applied to ground-based geophysical techniques. The use of coincident methods also allows consideration of conjunctive or joint inversion methods for the characterisation of the subsurface (see, for example, Vilhelmsen et al. (2014), Gallardo and Meju (2003), Kowalsky et al. (2006)).

1.2 Previous ground geophysical studies for palaeovalleys in the Musgrave Province

While there is an extensive literature on the application of ground-based geophysical methods for characterisation of aquifer systems and groundwater resources, there are few systematic studies on the relative merits of different approaches for these purposes, and more specifically in relation to the sedimentary systems (palaeovalleys) that are encountered in the Musgrave Province.

Most geophysical studies targeting the aquifer systems, specifically concerning stratigraphic definition and water quality have employed transient time domain electromagnetic (TDEM) methods and borehole geophysical logging. TDEM studies have had limited success (see, for example, Nelson (1974); Dodds (1996, 1997); Clarke (2000); Tewkesbury and Dodds (1996, 1997)). Borehole logging approaches, employing natural gamma, neutron and density logging have helped define water bearing units where used (see, for example, Dodds and Sampson 2000).

More recently, Parsekian et al. (2014) reported on the application of surface nuclear magnetic resonance (NMR) and TDEM soundings in a study of water-bearing sediments associated with the infilling of a wrench-graben located NNW of Fregon/Kaltjiti.

1.3 Overview and aim

The aim of this report is to detail the results from the application of several ground hydrogeophysical methods (both surface and borehole) to characterise the nature and variability associated with palaeovalley hydrogeology in the Musgrave Province of north-west South Australia. More specifically, the intent was to assess the merits of different hydrogeophysical methods with respect to their ability to define characteristics of the sediment fill, including their hydraulic aspects. This work forms part of a longer-term *systematic* study focussing on an area where surface and sub-surface geophysical methods could serve as a valuable adjunct to conventional hydrogeological investigations. Potentially the findings of this work will inform the application of hydrogeophysics in other remote parts of South Australia, as well as in other jurisdictions in Australia and overseas.

2 Study area

The ground hydrogeophysical test site is located ~5 km southeast of Kaltjiti/Fregon in close proximity to the Kaltjiti–Mimili road (Figure 1). The road transects the entire Lindsay East Palaeovalley perpendicular to its mainly N–S-orientation, as exemplified by the more conductive zone indicated in the airborne electromagnetic (AEM) interval conductivity image (Figure 1). An additional site for study (using borehole NMR) was located at the S22i drill hole, ~5 km north of Kaltjiti near the Kaltjiti–Umuwa road (Figure 1). This bore targeted a tributary to the main palaeovalley in a topographically high palaeo-interfluvial area overlying shallow basement.

Lying between the Musgrave and Everard ranges are extensive plains and rangelands (~550 m AHD), dominated by aeolian sand dunes and dune fields, sandplains and alluvial plains. Several creeks drain the Musgrave Ranges to the south and Officer Creek which crosses the study area just west of Kaltjiti, is one of the more prominent of these (Figure 1). For most of the year these creeks are dry, and only flow under high rainfall conditions often linked with episodic cyclonic conditions. Vegetation cover comprises predominantly grassland, shrub-land and open woodlands.

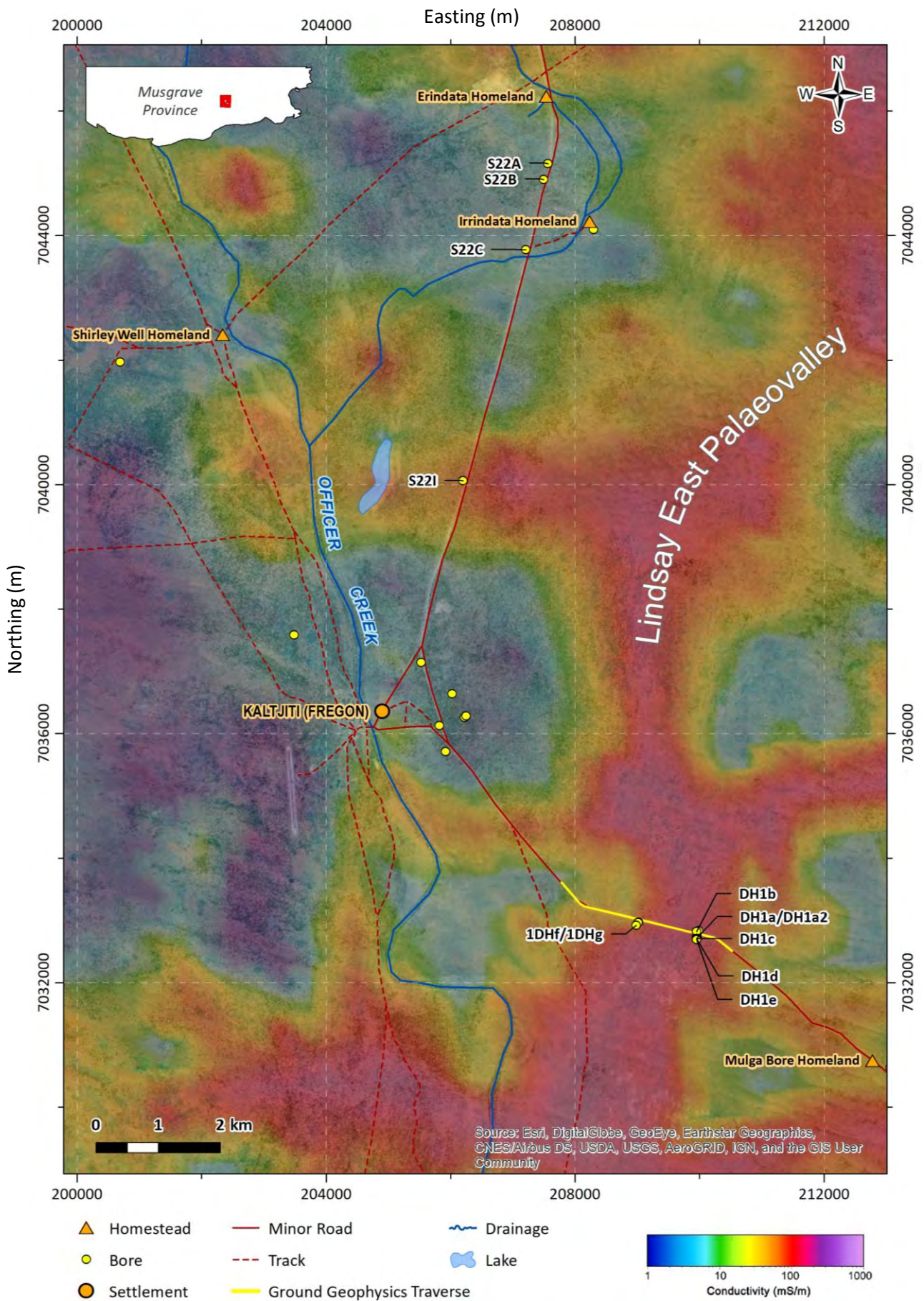
2.1 Climate

The climate of the study area is semi-arid to arid. Mean annual rainfall is generally below 300 mm/year and the mean annual temperature is 27 °C (BOM, 2018). Temperatures in the region can reach extremes, for example, in arid zones frosts are not uncommon during winter, with overnight lows several degrees below zero °C having been recorded. In summer, extremely high temperatures (up to 49°C) are also reached during the day. Most rainfall in the region occurs in the summer months and is linked to cyclonic activity (BOM, 2018). Rainfall also varies greatly on a local scale, with heavy falls often being restricted to small areas.

2.2 Geology

Although the focus for this investigation was the geophysical expression of the palaeovalley sediments associated with the Lindsay East Palaeovalley system, it is relevant to consider the broader geological framework for the study.

There is limited outcrop in the vicinity of the study area, and an interpretation of the basement geology is reliant upon limited drilling and the interpretation of regional airborne geophysical data sets (magnetics and more recently airborne electromagnetics). Similarly information about the nature and variability of the cover (regolith) has been limited to drilling, primarily for groundwater resources, but more recently the acquisition of regional airborne electromagnetic data has provided further insight into the spatial variability of that cover including the existence of a complex palaeodrainage with the presence of large palaeovalleys being defined (see Soerensen et al., 2018).



The Musgrave Province consists mainly of gneissic rocks of the Birksgate complex, deformed, metamorphosed and intruded by granitic plutons of the Pitjantjatjara Supersuite. This occurred during the Musgravian Orogeny (c. 1220–1120 Ma) (see, among others, Major and Conon (1993); Edgoose et al. (2004); Howard et al. (2011)). These rocks were intruded by mafic volcanics of the Giles Complex, during what is termed the Giles Event (c. 1085–1030 Ma) and include dykes of the Alcurra Dolerite (see, among others, Glikson et al. (1996); Woodhouse and Gum (2003); Edgoose et al. (2004); Howard et al. (2011); Quentin de Gromard et al. (2017)). Following the Giles Event, the Amata Dolerite (c. 825 Ma) intruded the rocks of the Musgrave Province (Werner et al., 2018). During the 580–520 Ma Petermann Orogeny, several of the prominent E–W-trending faults were reactivated leading to the development of widespread mylonitic shear zones and the exhumation of the Musgrave Province from beneath the Centralian Superbasin (Pawley et al., 2014). During the same period as the Petermann Orogeny, was the development of the Levinger and Moorliyanna grabens, which are interpreted as dextral pull-apart basins (Edgoose et al., 2004; Hand and Sandiford, 1999; Pawley et al., 2014). These were infilled with clastic sediments derived from the locally exposed Musgrave Province basement (Coats, 1962). The structural grain associated with the east–west trending shear zones, developed during the Musgravian Orogeny, and reactivated during the Petermann Orogeny (Woodhouse and Gum, 2003) is reflected in the airborne magnetics for the area around Kaltjiti/Fregon (Figure 2). They appear as low-intensity aeromagnetic lineaments across the study area, with many interpreted to have been reactivated during the c. 450–300 Ma Alice Springs Orogeny. The interpreted basement geology for the area is shown in Figure 3.

The Musgrave Province underwent at least one phase of intensive deep weathering and erosion prior to the deposition of clastic sediments of the Mesozoic Eromanga Basin in the east (Krapf et al., 2019). Through the Late Cretaceous and in the episodic weathering resulted in deep weathering profiles accompanied by duricrust development, and continuing erosion and sedimentation (Conon, 2004; Krapf et al., 2014). During the Late Paleogene and Early Neogene, the landscape was cut by numerous valleys (palaeovalleys) with drainages that had their headwaters in the Musgrave and Mann Ranges. Preferential incision into the weathered landscape and basement was along some of the east-west and associated cross-cutting structures (see Figure 5). Drainage was southwards towards the Officer Basin. In the Mid to Late Neogene the valleys filled with a mix of clastic sediments including alluvial, fluvial, and lacustrine sediments composed of clay, sandy clay, mixed sand-clay deposits, and lenses of coarse sand and gravel (Rogers, 1995). The onset of aridity in Quaternary, resulted in the development of alluvial fans against the ranges, alluvial outwash plains, and sandplains. Dune fields also developed (Krapf et al., 2018). The surface regolith of the study area is shown in Figure 5.

2.3 Hydrogeology

The hydrogeology of the Musgrave Province is complex both in terms of the hydrostratigraphy, but also in regards the character of the groundwater present (Watt and Berens, 2011). Limited available data has, to-date, meant that conceptualisation of hydrogeological processes is relatively general and assumptive (Costar et al., 2019), although more recent investigations (see, for example, Leaney et al. (2013), Kretschmer and Wohling (2014), Costar et al. (2019) and Krapf et al. (2019)) are beginning to address that.

Surface water features in the area are typically ephemeral and only flow after significant episodic rainfall events. Surface water from the Musgrave Ranges flows to the Ernabella Creek system and similar tributaries, some of which subsequently discharge to the Officer Creek which transects in a southerly direction just to the east of Kaltjiti (Figure 1). Drilling for town water supply and other infrastructure projects has identified groundwater resources of varying quantity and quality, and it has long been known that the region is characterised by a well-developed, and complex palaeovalley system that has significant potential for additional resource (see, for example, Tewkesbury and Dodds (1997); Watt and Berens, (2011)). The recently acquired AEM data across the Musgrave Province (Soerensen et al., 2018) has shed further light on that system, and recent drilling (see Keppel et al. (2019), and Costar et al. (2019)) as part of Goyder Institute's G-Flows Stage-3 Project has provided further insight into the nature of the aquifers present within these palaeovalley systems.

Easting (m)

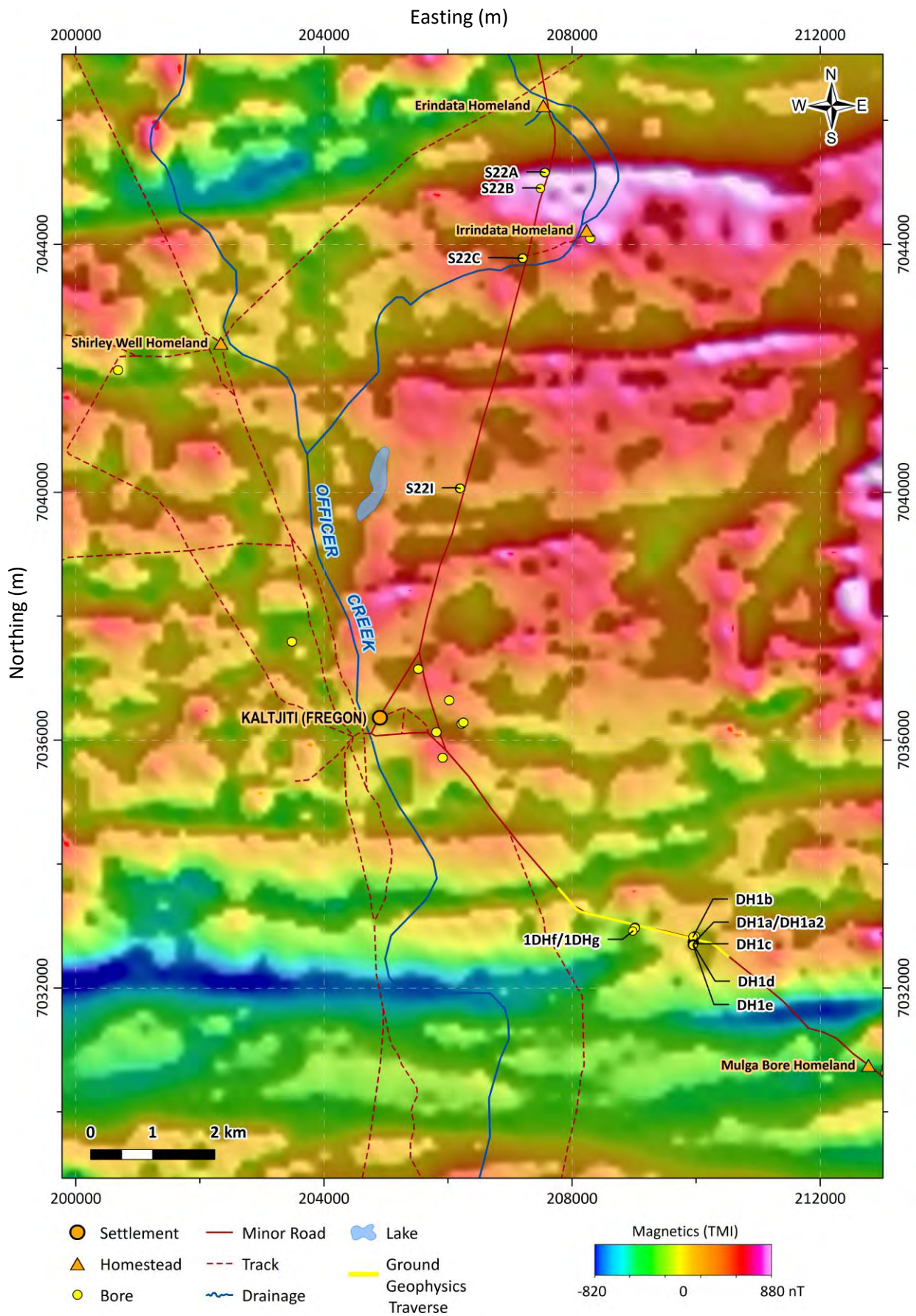


Figure 2. Pseudocoloured airborne magnetics total magnetic Intensity (TMI) image modulated by intensity variations from the 1st vertical derivative of the magnetics data for the study area.

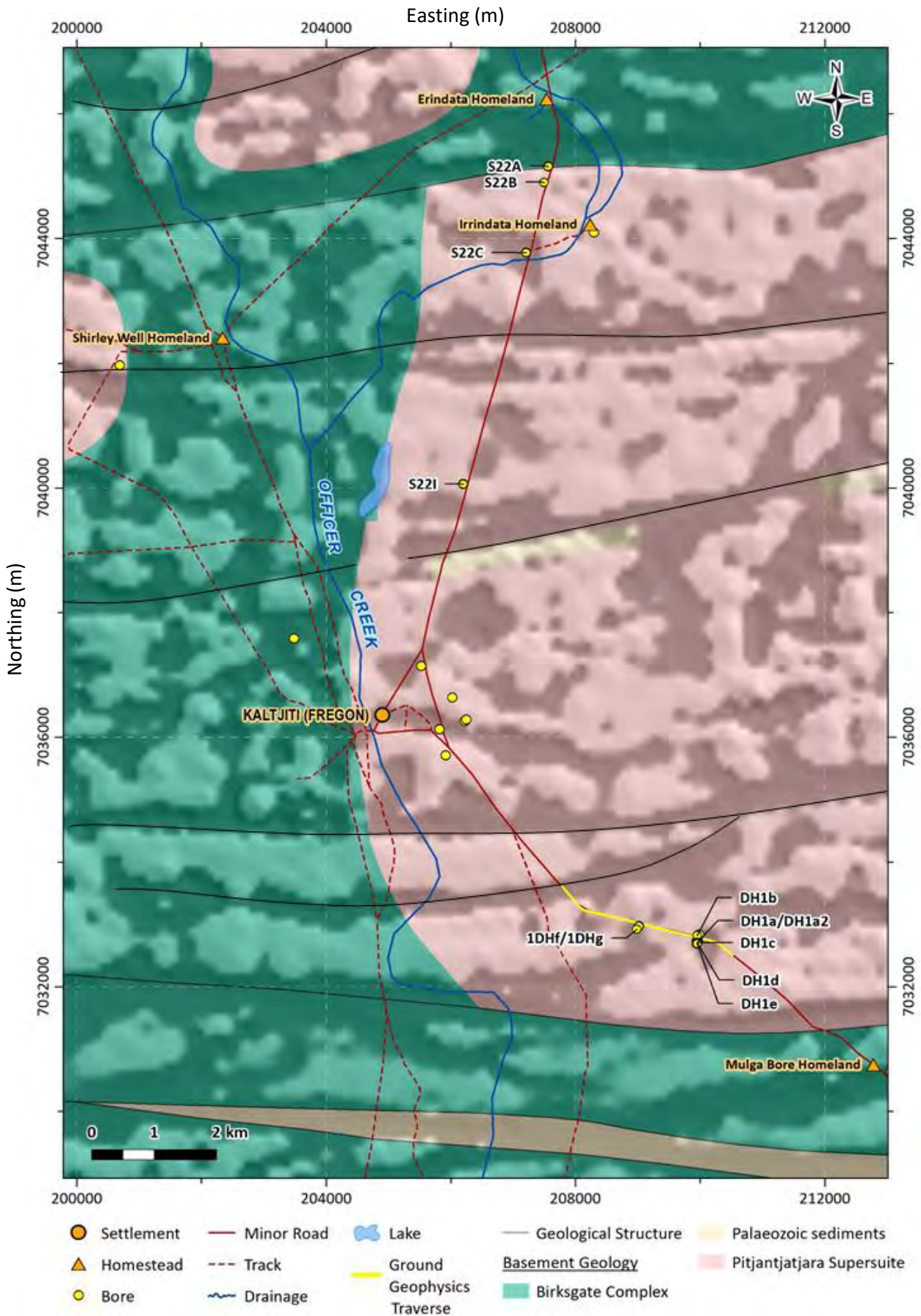


Figure 3. Interpreted basement geology in study area overlain on image of 1st vertical derivative magnetics.

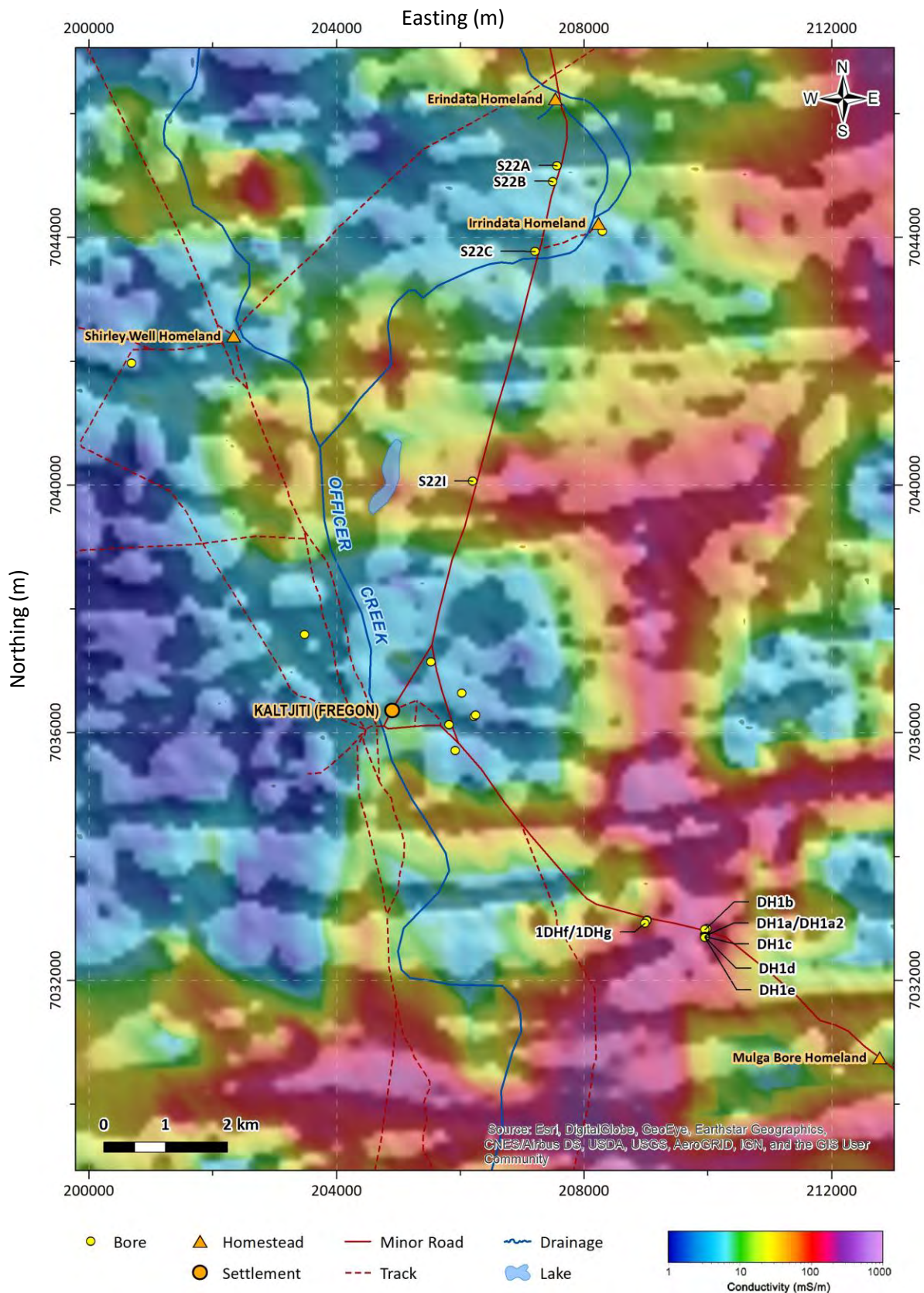


Figure 4. Pseudocoloured airborne electromagnetic (AEM) conductivity-depth interval (50-60 m) modulated in intensity by the 1st vertical derivative of the airborne magnetics. The main linear conductive feature runs north to south and comprises conductive valley fill within the Lindsay East Palaeovalley (see also Figure 1). The correspondence between the orientation of the palaeovalley fill and structure (de-magnetised zones represented as dark areas in the image) is apparent.

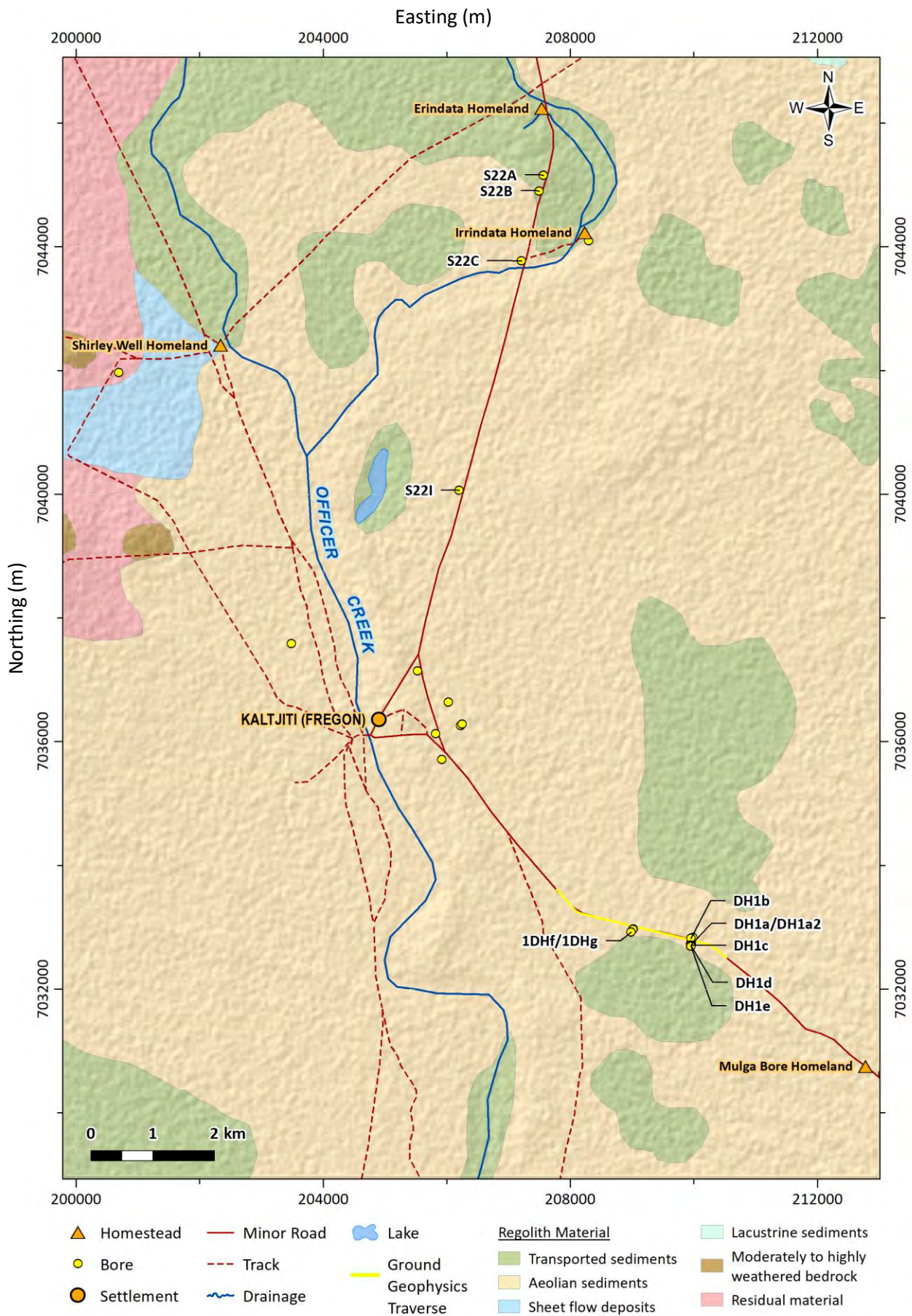


Figure 5. Interpreted surface regolith geology in the study area. Source: Krapf .et al. (2012).

3 Ground-based hydrogeophysical methods

Whilst a variety of ground-based geophysical approaches exist for near surface characterisation, our effort is concentrating on those that can be employed to characterise the subsurface down to 100 m and more. The initial studies also concentrated on those techniques that might help elucidate hydrostratigraphy, hydraulic properties and groundwater quality.

The initial focus of the work in the area involved an assessment of the following methods:

1. Surface time domain electromagnetics (TDEM)
2. Active seismic (refraction and reflection)
3. Borehole nuclear magnetic resonance (BNMR), and
4. Borehole inductive conductivity (BIC)

In the first phase of this research, findings from the application of four methods, namely surface-based active seismic, BNMR and inductive conductivity, and ground TDEM are considered. In a separate study undertaken by the South Australian Government's Department for Environment and Water (see Keppel et al., 2019), the geophysical logging of boreholes drilled as part of the G-Flows Stage-3 study was also undertaken.

Further work is planned for the study site involving a range of additional techniques. This will be undertaken by CSIRO's Deep Earth Imaging Future Science Platform. Future data acquisition and analysis will consider data from the following methods:

1. Ground gravity
2. Surface nuclear magnetic resonance (sNMR)
3. Passive (ambient noise) seismic
4. Additional surface TDEM

The extended study will also involve additional and longer-term pump testing to provide calibration data for the NMR methods.

4 Active seismic method

Seismic reflection and refraction surveys were undertaken in the APY Lands of South Australia in August 2018. A primary goal of the survey was to provide a detailed image of the main stem of a palaeovalley system that has been identified by airborne electromagnetic (AEM) surveys (the DH1 site on the Lindsay East Palaeovalley, on the road ~5 km east of the community of Kaltjiti/Fregon: see Figure 1). Over the course of five days the four-person team was able to collect a 1974 m of profile running perpendicular to the main trunk of the palaeovalley. An objective of the study was to obtain another independent measurement of the location of bedrock to help validate the AEM interpretation and elucidate details about the fill within the palaeovalley. The seismic data set is supported by several boreholes that had been drilled along the seismic profile earlier in the month. The seismic refraction results show significant variation in the near surface (top 10 m) velocity structure and a deep (~100 m) refractor that is believed to be the top of unweathered bedrock. The seismic reflection results show significant variability, both lateral and vertical, in the top of bedrock reflector and reveal prominent and clear reflections down to depths greater than 400 m.

4.1 Methods

4.1.1 SEISMIC REFRACTION

The refraction seismic survey method is an active source geophysical method that quantifies seismic velocity. It involves the measurement of primary seismic waves (P-waves; compressional waves) that travel via direct and critically refracted ray-paths (Figure 6). The approach specifically measures the time taken (travel times) for the P-wave to travel from the source through a subsurface layer to a series of detectors (geophones). The detectors are at a known distance from the source which therefore allows for a P-wave velocity to be calculated for that subsurface layer.

Depending on the type of source and receiver, refraction can be used to estimate P-wave (energy propagating along the direction of travel) or s-wave (energy propagating perpendicular to the direction of travel) velocities. In our case, we had vertical geophones and an impulsive source, so we are quantifying P-wave seismic velocity. To collect seismic refraction data multiple geophones are laid out in a profile along the surface. Then, a seismic source produces elastic energy that travels from the source to each geophone. The location where the seismic source was fired is referred to as a shot or shot point. The elastic displacements are recorded and the time it takes for the elastic energy to travel from the source to each geophone is identified on traces that are not noisy; this process is done manually. Multiple shots along the profile are taken to construct thousands of source to receiver travel-times, which are referred to as travel-time curves. The shapes of these curves are controlled by the P-wave velocity structure below the profile. P-wave velocity is controlled by the elastic properties of the material, porosity, and saturation. In cases where the lithology is known to be consistent, that is the elastic properties are not expected to change over the length of the line, changes in P-wave velocity likely be dominated by porosity. If this pore space is filled with a fluid, in our case water, then the P-wave velocity will increase. The rate of increase depends on the rock physics model used which depends on the geometry of the pore space.

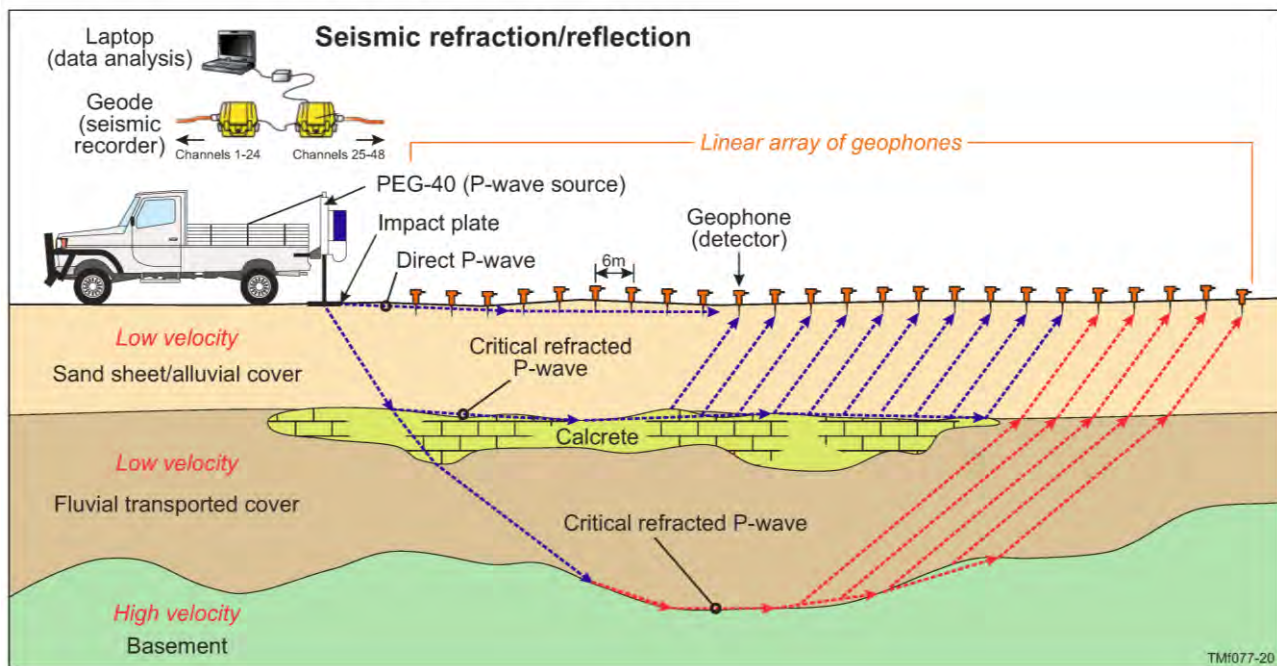


Figure 6. The layout of equipment employed in a refraction seismic survey, illustrating ray paths of direct and critically refracted P-waves through the subsurface. For this study the P-wave source energy was generated by a Propelled Energy Generator 40 kg (PEG-40) accelerated weight drop mounted on the rear end of a field 4WD. The seismic response was recorded by Geode seismic recorders (Figure adapted from Goodwin et al. (2017)).

For this study we used a 48-channel system with 14 Hz geophones and a 40 kg accelerated weight drop for a source (Figure 14b & c). The geophones were placed at 6 m spacing, producing lines that were 282 m long. To ensure high quality data, we stacked 10 shots at each location. We manually picked 19,495 first arrival times for this data set. An example of picking first arrivals is shown in Figure 7. These travel times are inverted (no amplitude information is used) using an open source travel-time tomography code in the Python Geophysical Inversion and Modeling Library (PyGIMLi) (Rücker et al., 2017). The inversion traces rays using a shortest path algorithm (Dijkstra, 1959; Moser, 1991; Moser et al., 1992) through a non-structured triangular mesh extending from the surface to a depth of 150 m.

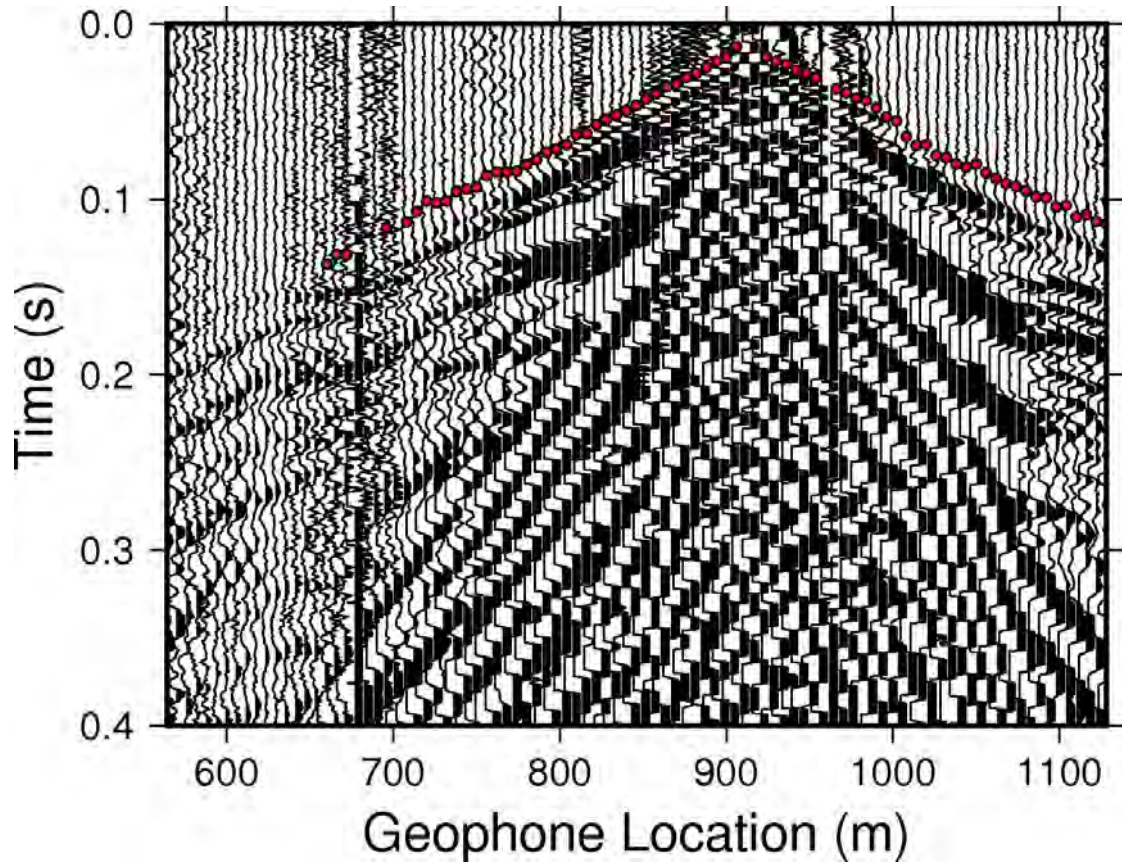


Figure 7. A shot from 912 m along the main profile showing the first arrival picks. These picks are done manually for each shot in the survey. If the trace is too noisy a pick is not made.

PyGIMLi utilises a deterministic Gauss-Newton inversion scheme and incorporates a data weight matrix (Rücker et al., 2017). We populated the data weight matrix using reciprocal travel-times. To quantify uncertainty, we incorporated a bootstrapping algorithm on the travel-time picks. The model fits are determined by a χ^2 misfit, which incorporates our picking errors and a root mean square (RMS) error.

We use the reciprocal values to drive the error weight matrix in the PyGIMLi inversion (Rücker et al., 2017). Thus, an error be assigned to every pick. In most cases we used the reciprocal error plus 1.2 ms. In locations where we did not have a reciprocal travel-time we applied a linear function as a function of offset (distance from source). In this case error (in seconds) was defined by Eq. 1.

$$error = \frac{0.004}{235} offset + 0.0012 \quad (\text{Eq. 1})$$

where offset is simply the distance from the source to the receiver, and the spread length was 235 m. We use Eq. 1 and the calculated reciprocal values to ensure that each pick has an assigned error (Figure 7). It also provides a way to determine if the data are over fit or under fit. These errors are read into the inversion and used to weight the travel-times during the inversion as well as calculate the χ^2 fit:

$$\chi^2 = \frac{1}{N} \sum_i \frac{(t_{obs} - t_{model})^2}{\sigma_i^2} \quad (\text{Eq. 2})$$

where t_{obs} is the observed travel time, t_{model} is the modeled travel time, σ is the picking error, and N is the total number of picks.

With the travel-time picks and associated errors collected we can invert the model. The mesh was selected so that there were at least three nodes between each geophone and the maximum triangle size was no more than 50 m. Thus, we used a gradient starting model with 300 m/s at the surface and 4000 m/s at 150 m depth. The depth of the model was selected to not limit the ray paths. This took some experimentation, but the final mesh extends a few meters below the lowest ray path. Smoothing parameters were manually selected through trial and error to achieve a feasible geologic model and still achieve a good model fit. Specific settings in the PyGIMLi refraction inversion were set as follows: Lambda equal to 400 and the z-weight to 0.1 and the maximum iterations to 10.

Although it is difficult to say exactly how accurate these velocities are, we did attempt to quantify velocity uncertainty. To quantify uncertainty, we took the 19,495 travel time picks and randomly removed 40% (7798 data points). We used this decimated data set to run an inversion. We then removed another random 40% of the original data set and inverted again. This process was repeated 20 times. Each velocity model was saved, and at the end all 10 models were averaged together. The average model was run through the forward model to get the travel-times and the error fits. This means that at each model parameter we have a standard deviation, indicating how much it changed as the result of randomly removing data. The high standard deviations highlight areas of the highest uncertainty.

4.1.2 SEISMIC REFLECTION

Seismic reflection exploits changes in seismic impedance, which is a function of velocity and rock density at different boundaries in the subsurface. By recording the ground motion response from many shots and many receivers a high-resolution image can be created from these boundaries. Seismic reflection data must be collected with a dense array of shots and receivers to maximise the common midpoint (CMP) fold. Once the data are collected the basic flow to seismic reflection is as follows: 1) quality control (i.e. remove noisy traces), 2) sort the shot gathers into CMP gathers, 3) apply filters to remove surface waves (i.e. mutes, f-k filters, or band-pass filters), 4) apply gains to visually inspect reflections, 5) conduct a normal move out (NMO) velocity analysis on CMP gathers, 6) apply normal move out to flatten reflections, and 7) stack the flattened CMP gathers. From this stage the derived velocity model can be used to apply migration and go from a time image into depth image.

In the field, the data are collected in shot gathers (Figure 8a). This is because it is difficult to pick up and move the receivers compared with moving the source along the profile. The first step in reflection processing is to generate common midpoint (CMP) gathers. A CMP gather is the theoretical construction that sorts through the data and selects source and receiver pairs that share a midpoint. The assumption is that in a flat-layered system these source and receiver pairs are receiving energy reflected off the same point of a subsurface boundary (Figure 8a). In reflection, the data will be re-arranged into CMP gathers. The total number of traces in these CMP gathers is referred to as the fold. The fold comes out in stacking charts (Figure 8b). By plotting the location of each shot and receiver a CMP lies on the diagonal (Figure 8b). The fold of the data can be adjusted by either increasing the total number of receivers, which was limited to 48 in our case, or by increasing the total number of shots. The higher the fold, the better the signal-to-noise. To cover just under 2 km in a week with a four-person crew, the data were set up to have a maximum of 48-fold at the centre of each roll graduating out to 24-fold on each line. Due to time constraints and field conditions the data fold varies spatially (Figure 9). Although the fold remains above 30 channels for the entire profile the fold does drop as a result of missed shots (Figure 9).

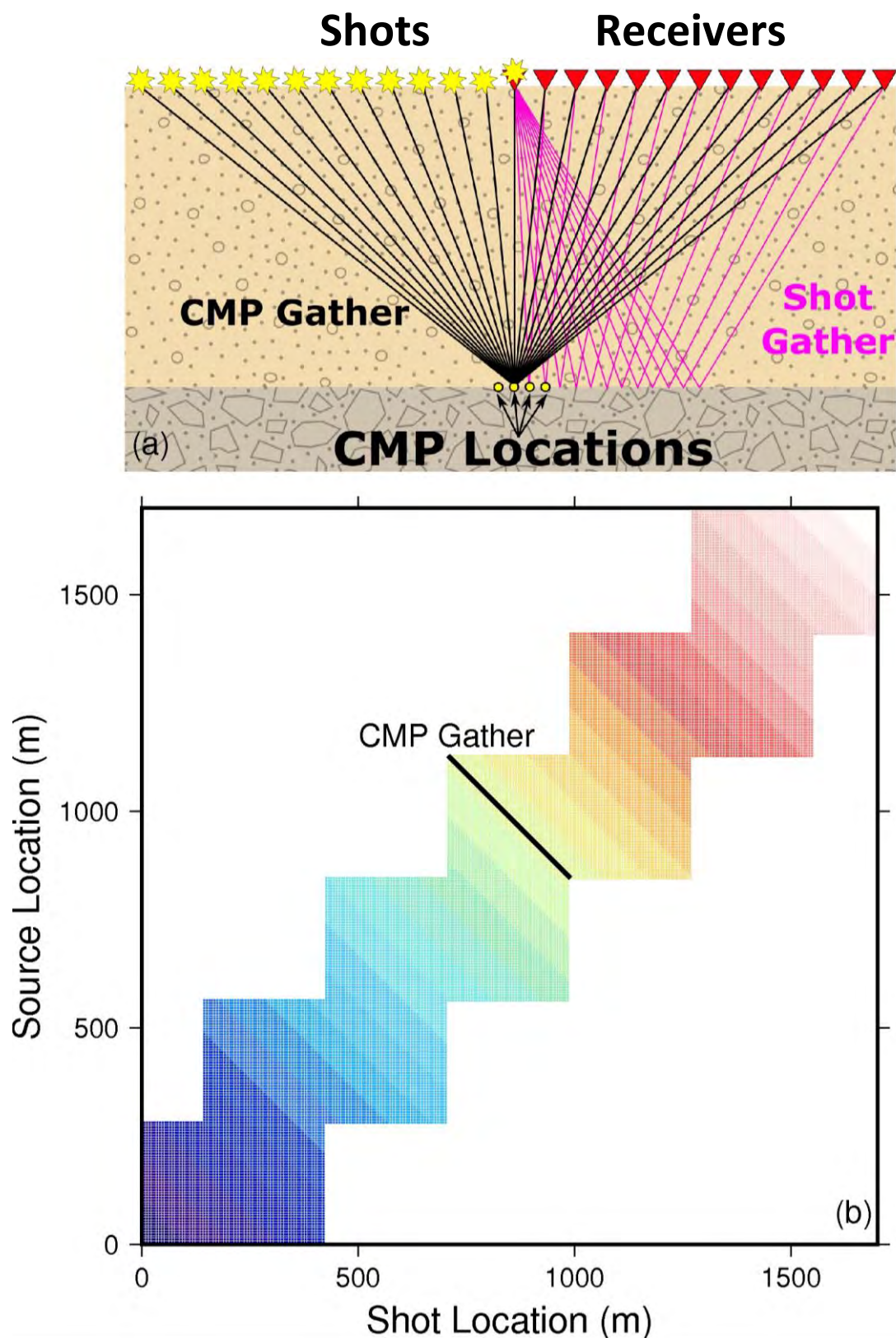


Figure 8. (a) Theoretical drawing demonstrating a common midpoint (CMP) gather. A single shot gather is shown in magenta, where energy is reflected of a boundary between the source and all the receivers. With many shots it is possible to collect all source and receiver pairs that share a common midpoint. A supergather can be created by combining any number of adjacent CMP locations. (b) The stacking chart used to design the survey geometry for these data. The CMP fold of the data set is presented in the diagonal space. Colors represent increasing CMP locations.

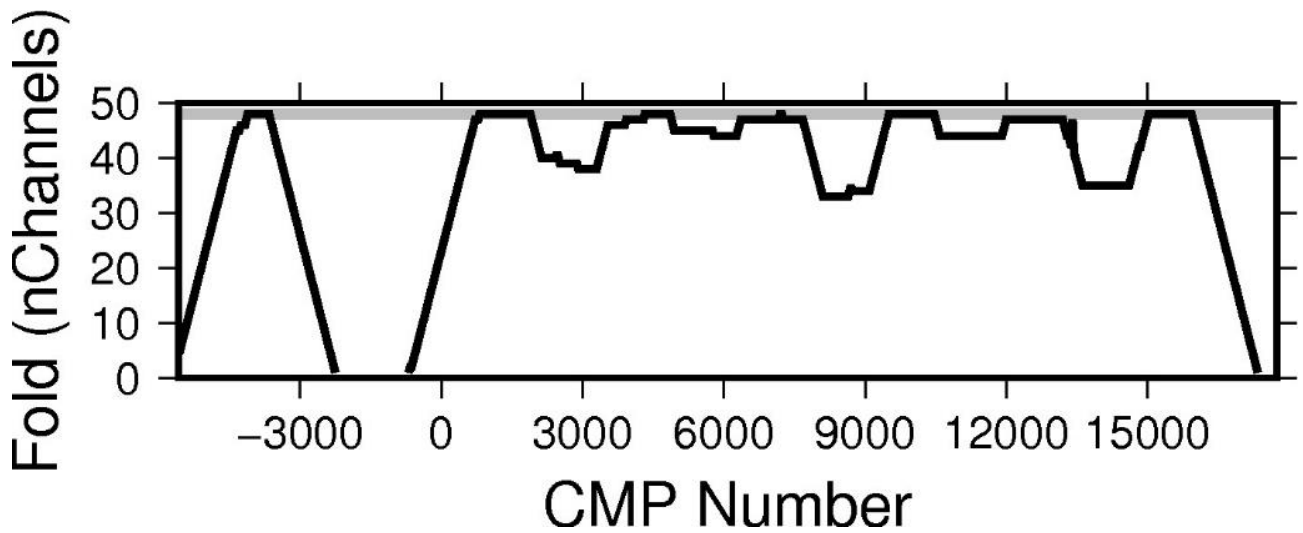


Figure 9. Common midpoint (CMP) fold of the data. The maximum fold possible is 58. The higher the fold the higher the signal-to-noise.

A useful technique to increase the signal-to-noise is to generate a supergather. Here, we combine three CMP gathers: the one at the point of interest and the two adjacent ones. This choice greatly improves around ability to see and pick NMO velocities on reflections (Figure 10). The increased signal enhancement comes at the cost of a loss in horizontal resolution. Because information from adjacent CMPs are now incorporated into a single CDP there is data redundancy which causes reflections to smear horizontally. This choice means that our maximum fold went from 48 channels to 144-channels.

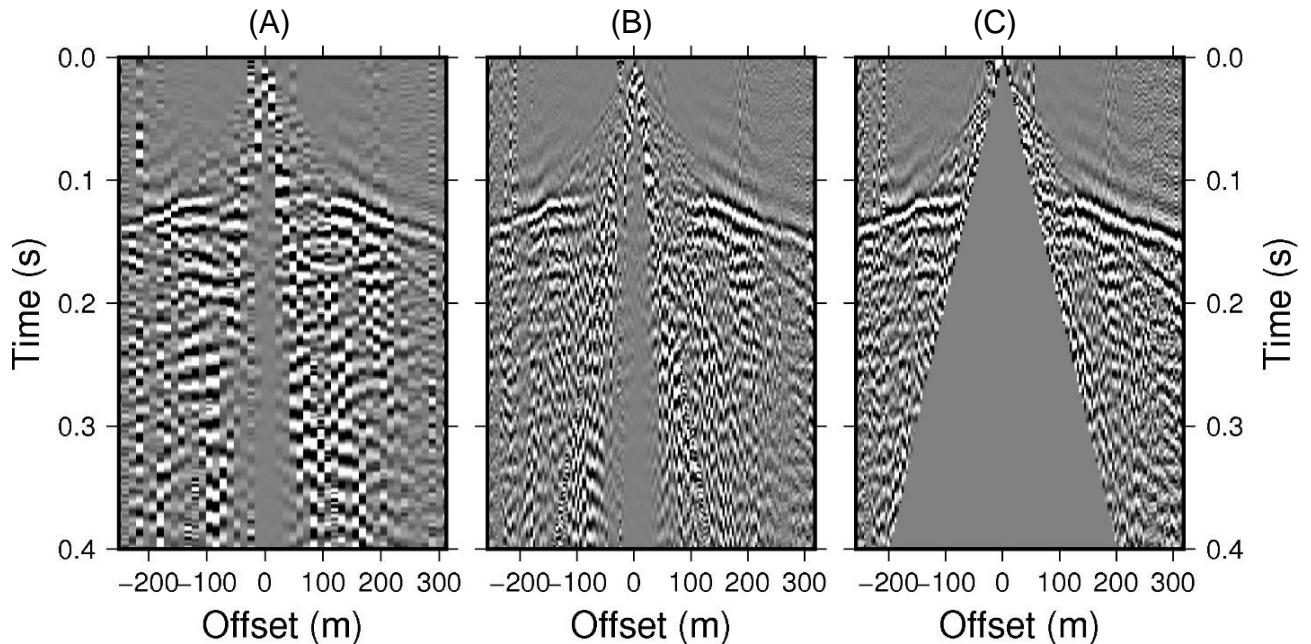


Figure 10. This figure shows the impact of using supergathers. (A) common depth point (CDP) from 1254 m; (B) Supergather from the same location (including two adjacent CMPs); (C) Supergather from (B) which has been filtered to remove surface wave noise.

In reflection processing on land, the largest source of noise is surface waves. The surface waves are the high-amplitude and low-frequency energy that propagates linearly from the shot location. In seismic reflection this energy masks the reflection energy which is higher frequency and has a much smaller amplitude. In CMP gathers, the surface waves are large amplitude linear features that propagate from zero offset. Given that we collected our data at 6-m interval spacing, our data is spatially aliased and all attempts at removing the surface wave energy via an F-K filter failed. To minimise the effect of surface waves on this data set, we applied a band pass filter between 50 and 200 Hz and applied a triangular mute to all supergathers (Figure 10c). The mute was applied in the CMP space and was chosen to kill all energy below a line with a slope of 0.0002 starting at zero offset. This mute means that a lot of the shallow reflections (those above about 0.05 s) will be unreliable because there is a lack of data to stack. This method was conservative to ensure the effect of surface waves did not show up in the final stacked image.

Gains are critical to visualise the data and conduct an NMO analysis. The first is a trace normalisation, where each trace is normalised to the highest amplitude in the trace. This gain tends to amplify noise if the entire trace is noise. The second is automated gain control (agc). This gain allows the user to specify a time window and then normalises the traces within based on the values within the window. This type of gain de-amplifies large scale amplitudes and amplifies low-amplitude noise. It is good at making the small reflection signals visible. Neither of these gains can be undone after the stack, so attribute analysis (i.e. the information contained in the amplitudes of the signals) is lost. This is a critical assumption for this methodology. Prior to stacking and NMO we applied trace normalised gains. The thought here is that we are unable to flatten and stack what we are unable to see. As a result, the amplitudes of the final reflections are not accurate. The stronger reflections represent the continuity of the reflection boundary not the change in impedance contrast.

After gaining the data we apply a normal moveout correction to the CMP gathers. Normal moveout assumes flat and continuous layers. Under this assumption the time it takes for energy to travel from the source down to a reflector and back up to a receiver on the surface can be calculated analytically (Eq. 3):

$$t^2 = t_0^2 + \frac{x^2}{V^2} \quad (\text{Eq. 3})$$

where t is time in seconds, x is distance from the source and V is the root mean squared (RMS) velocity. The RMS velocity is an average of all the layers above the layer that is the source of the reflection. In the CMP domain reflections show up as hyperbolas. Using Eq. 3 we calculated semblance curves, that is the energy along a set of curves to aid in the picking of the RMS velocities. This means that small changes in the RMS velocity can imply large velocity changes in the layers above. Using an interactive plot and semblance we picked the time to the top of the reflection and the velocity that best fits it (Figure 11). After picking time and velocity for 612 CMPs we show that the picked velocities and time have significant variation but are continuous from CMP to CMP (Figure 12). During the picking of the RMS velocities we tried to pick the same strong reflector that usually showed up between 0.09-0.13 s (Figure 11). To keep the processing simple and to prevent complexities in the time-to-depth conversion, only one RMS velocity for each CMP was picked. The data set might be improved on by picking multiple reflections and generated a more complex RMS velocity function.

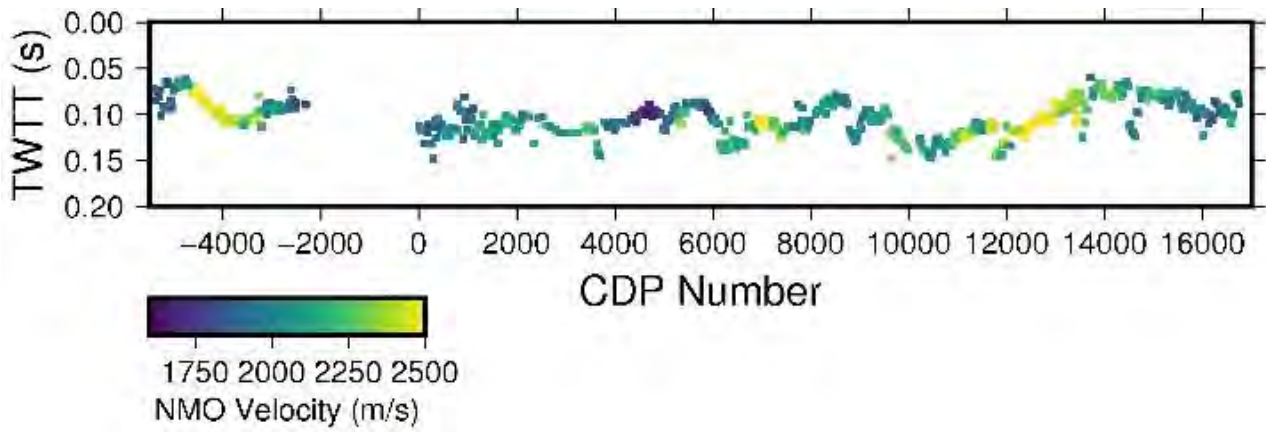


Figure 11. Two-way travel time of the picked reflection (with aid of semblance plot) coloured by the moveout velocity. Note the continuity between gathers.

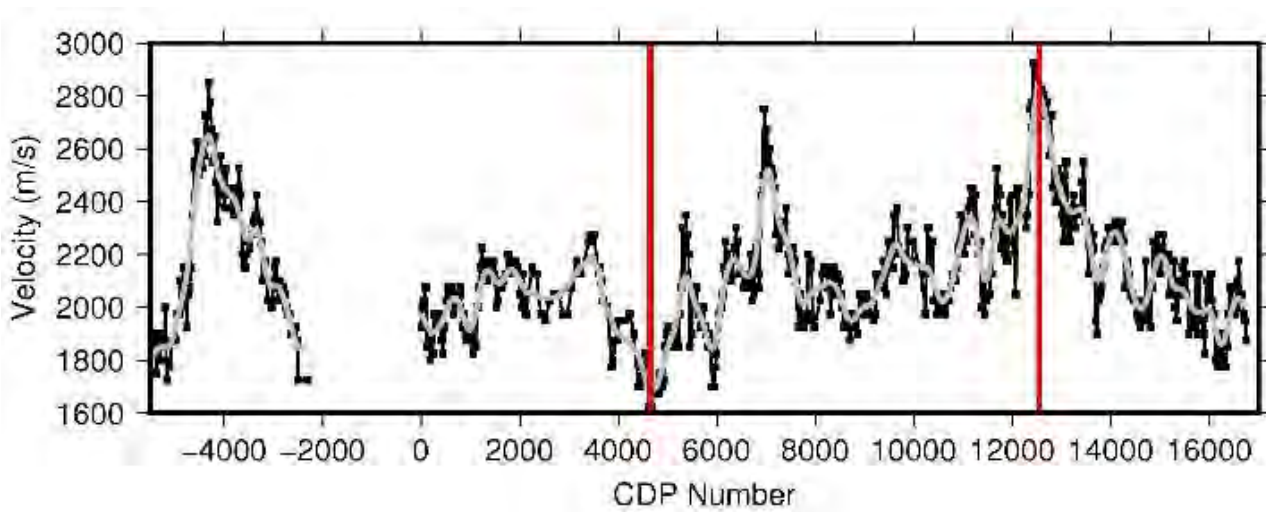


Figure 12. The normal move out (NMO) velocity plotted for each common depth point (CDP) number. The black dots are the raw moveout velocity and the grey line is a smoothed out version that was used for the moveout and stacking. Red vertical lines indicate the supergathers shown in Figure 13.

Using the RMS velocity function (Figure 11), we smoothed all abrupt changes in velocity by applying a low-pass filter (Figure 12). This choice provides smoother velocity transitions from CMPT to CM. Using these smoothed out velocities we applied normal moveout correction. NMO correction essentially subtracts the time it would take for energy to travel to and from a reflector at depth (Eq. 3) and flattens out reflections with that given velocity (Figure 13). These flattened reflections can then be stacked laterally to form a single trace at a CMP location. In theory other waveforms, such as surface waves and refractors, get stacked out because they are not coherent in this space, whilst the reflections lie horizontal and stack to gather (Figure 13). The resulting stacked trace represents the layer interfaces directly below the CMP. Stacking together the CMP produces the stacked section, which shows the reflectors as a function of time. The RMS velocity function can be used to go from time-to-depth (Figure 13). Finally, the velocity model derived from the NMO velocities is used to convert from time-to-depth. There is some uncertainty associated with this. In our case, the simple assumption of a single NMO velocity helps keep this uncertainty minimised by choosing not to propagate additional uncertainty associated with the velocity model into the depth calculation.

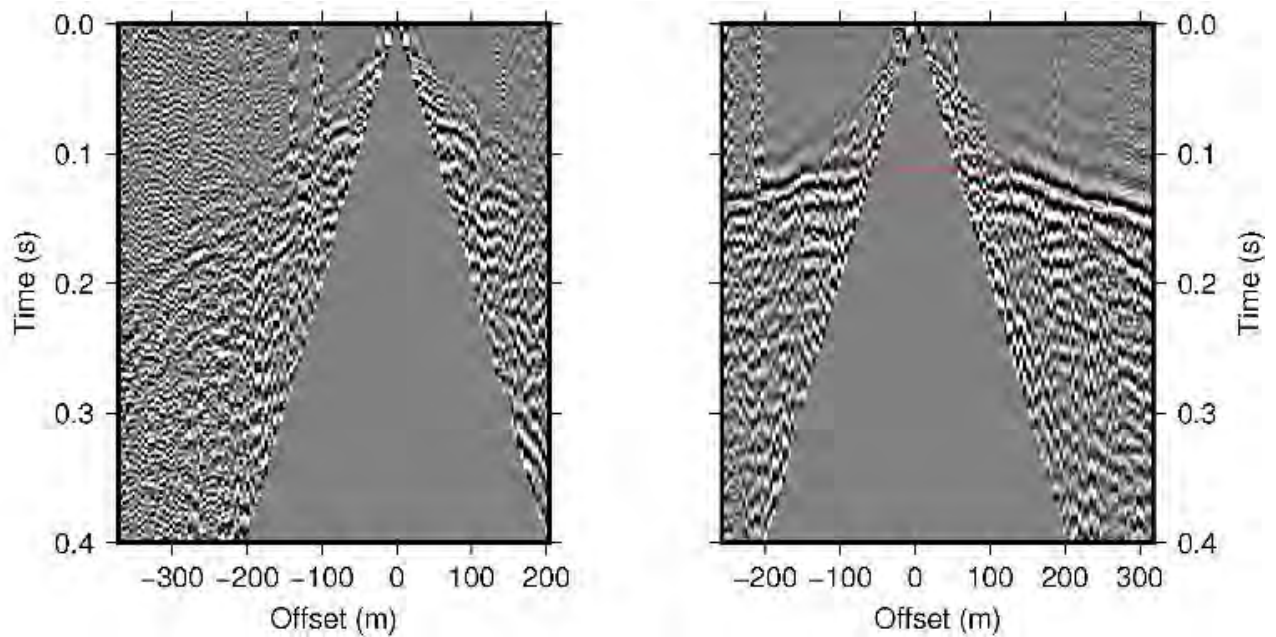


Figure 13. Supergathers from common depth point (CDP) number 4650 (left), and CDP 12540 (right). The red dashed line shows the moveout curve from the velocity profile shown in Figure 12.

4.2 Field data acquisition

From August 18th to 23rd 2018 a four-person team was present in the APY lands collecting seismic reflection and refraction data. Due to cultural constraints, the team was limited to working along the roadside. The target was the main trunk of a palaeovalley system that is easily identifiable in a 60–70 m depth section from the regions airborne electromagnetic survey (Figure 14a). Work was conducted along the main road used to travel from Mimili to Kaltjiti/Fregon (Figure 14a).

All seismic data were recorded with two Geometrics Geodes, which supported a maximum of 48 channels using 14 Hz vertical geophones (<https://www.geometrics.com/product/geode-exploration-seismograph/>). To cover a significant amount of ground in the allotted 5-day time slot we used a geophone spacing of 6 m. It should be noted, that with this current set up this is the largest offset achievable. Over the course of 5 days the team collected a total of seven individual 282 m long profiles (Figure 14a).

The quality of the reflection survey depends on the common midpoint point (CMP) fold. The CMP is defined as the point off a reflector at depth that is halfway between the source and receiver that is shared by many different source receiver pairs. The CMP fold is defined by the total number of these shared source and receiver pairs and is a function of the total number of channels and the shot spacing. To maximise the CDP fold we collected shots every 6 m along the profile and additional off-end shots. To have maximum fold at the first geophone the shots would have to start one whole line length before the first geophone. To save time we elected to begin-and-end shooting with points that were half of the line length from the first and last geophones. This results in a CMP fold of ~ 24 at the first geophone with maximum fold occurring by $\frac{1}{4}$ of the line length. We used the propelled energy generator (PEG) as a seismic source (Figure 14c). The PEG is a 40 kg accelerated weight drop that was mounted to the back of the vehicle (Figure 14c). The PEG is battery operated and has a quick cycle time (~ 10 s per shot), making it possible to cover significant ground with dense shot spacing. The weight from the PEG struck a 2 cm thick, 20 x 20 cm steel plate. To increase the signal to noise ratio, we collected and stacked eight shots at each shot location. The entire data set consists of 391 unique shot locations (this number does not include repeat shot locations when the receivers were moved for a roll along).

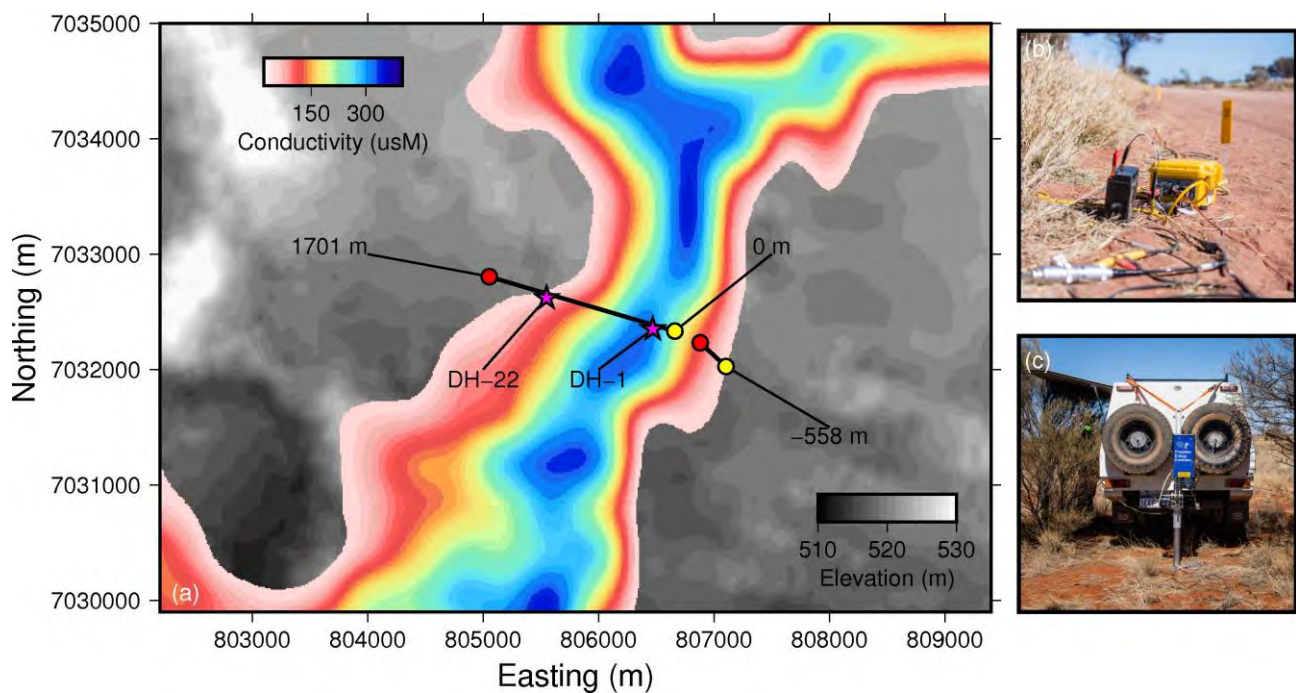


Figure 14. Location of the seismic surveys. (a) Underlying 10 m elevation data from Shuttle Rader Topographic Mission (SRTM). Overlaid on top of the elevation map is a conductivity depth section from 60-70 m below the surface. Electrical conductivity values greater than $55 \mu\text{S/m}$ are marked out to highlight the palaeovalley location. The airborne data were inverted using 400×400 m pixels, but a minimum curvature interpolation was applied for visualisation. The seismic profile running perpendicular to the channel was collected from southeast to northwest because we were required to shoot along the road. The yellow circles represent starts of profiles where the reference locations is near the centre of the palaeovalley and is marked accordingly. (b) Image of a geomatics Geode and cable along the side of the road. The image is taken looking toward the northwest. (c) Image of the PEG and steel plate used as the source. Here it is shown mounted onto the CSIRO vehicle and the 40 kg weight drop is fully extended.

4.3 Results

4.3.1 SEISMIC REFRACTION

First-arrival picks for the entire dataset are shown in Figure 15a. Overall data quality was very high. The only notable exception is the first roll (0–282 m) where generators present at the drilling site polluted the signal, resulting in multiple shots being skipped due to drilling equipment on the edge of the road. Here data quality was assessed by the picks' reciprocal travel time (Figure 15b). The reciprocal travel-time should be equal as it represents the travel time from the source to receiver as single receivers and then when the source is swapped with the same receiver. The long section was generated by inverting a total of 19,495 travel-time picks. The smaller section is based on 2561 travel-time picks. All the picks were picked manually, and both inversions showed excellent data quality and excellent model fits, thus most of the structures are considered to be present.

Typically, the higher P-wave velocity is associated with more solid and lower porosity materials. Solid granite at the surface has a velocity of roughly 4000 m/s and saprolite near the surface has a velocity between 1100-1200 m/s. In this context we define saprolite by its elastic properties, which is a material that would probably ring to hammer but that you could peel apart with your fingers. Water has a velocity of 1500 m/s. It is worth noting that saturation dramatically increases the P-wave velocity. So material below the water table should have velocities greater than 1500 m/s. The two sections were inverted separately. The same meshing and inversion were used for consistency. The long section was generated by inverting a total of 19,495 travel-time picks. The smaller section is based on 2561 travel-time picks.

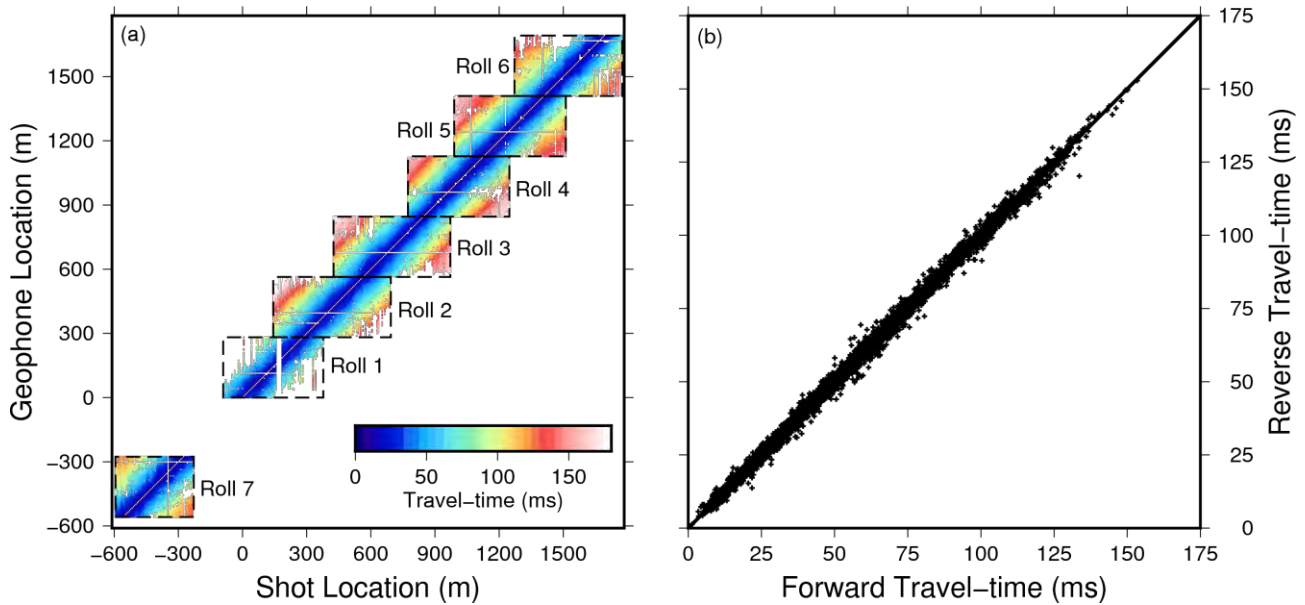


Figure 15. (a) First-arrival picks for the entire data set. Each roll is highlighted by a rectangular box. In an ideal and noise-free environment the entire rectangle would be filled. This highlights the generator noise on Roll -1. The cooler colours represent shorter travel times and the warmer colours are longer travel-times. (b). Plot of the reciprocal travel-times. This is calculated by comparing the travel time at a geophone where the shot and receiver are reversed. In an ideal and noise-free environment all the picks should lie on a 1:1 line. This plot shows that overall the data quality is very good.

The first observation is related to the depth to bedrock. Anything with velocity greater than 4000 m/s is assumed to be bedrock (bright yellows in Figure 16). Therefore, it can be seen that between 500 and 1750 m the refraction data set appears to define bedrock (Figure 16a). The bedrock comes closer to the surface between 1250 and 1550 m (Figure 16a). Note that from a geophysics standpoint, the region between 1250 and 1550 m is a result of a very strong seismic signal in the travel-time data, which supports the assertion that we are imaging bedrock. However, there is also a lack of fast velocities between 0 and 500 m. This means that from these data alone it is not possible to define bedrock across the entire 1700 m transect. The lack of bedrock (via high velocities) at the beginning of the profile is caused by one of two things. Firstly, it could be because the far offset data (the data that define the bedrock) could not be picked because the drillers were running a generator on site, which caused minute seismic signals interfering with our measurements. This made the small signals at the far offsets difficult to pick. Secondly, it could be that the bedrock continued to dive deeper here and that even with over 300 m of offset we did not receive signal from the bedrock.

The second key observation to highlight is the high velocity features near the surface. To make these more obvious, the scale has been changed (Figure 17). These features are difficult to see in the full profile (Figure 17a). But in the 600 m sections of the profile (Figure 17c-e) they become more obvious. These features occur between 5–10 m below the surface and have velocities between 2500–3500 m/s (bright yellows in Figure 17). These features are laterally heterogeneous and occur everywhere on the line. From a geophysical standpoint, they produce clear signatures in the raw data, and therefore are believed to represent real structures. At this point, these high velocity features are interpreted as calcrete lenses. The data suggest that the calcrete is not one continuous layer but is broken up along the profile.

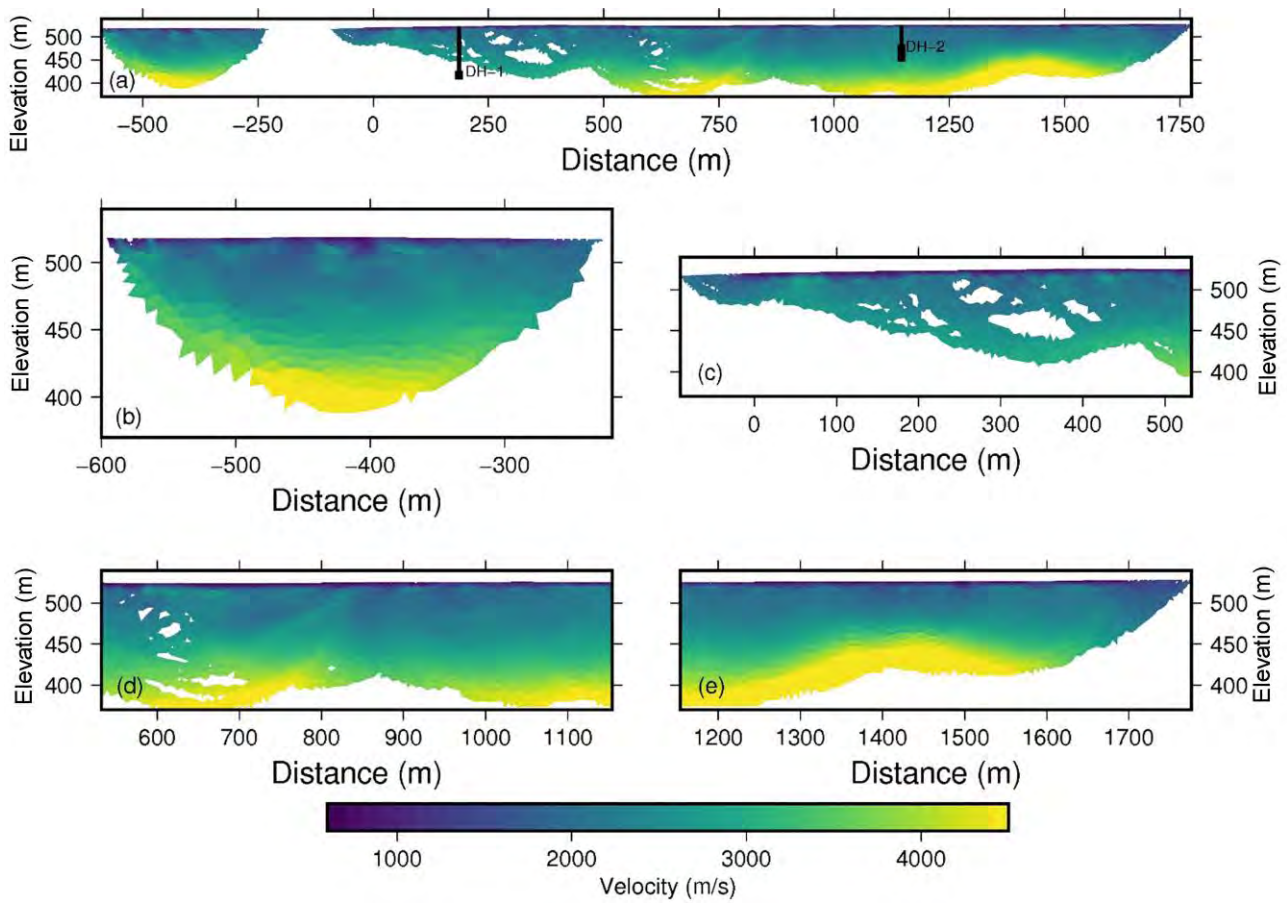


Figure 16. P-wave velocity. (a) Results for the entire seismic refraction profile shown with no vertical exaggeration. The gap in the line was due to a corner that we were uncomfortable operating on because of road traffic the location of the drill holes has been plotted for reference. The thick part at the bottom of DH-1 and DH-2 is where the log marked, “Weathered granitic rock, possibly gneissic. Coarse to very coarse-grained quartz sand sized fragments and kaolinitic clay”. Panels b-e are shown so that more details can be observed. Y-axis scale for all panels is in metres (i.e. all of these panels are shown with no vertical exaggeration); (b) The first short profile; (c) -90–532 m; (d) 532–1154 m; (e) 1154–1776 m.

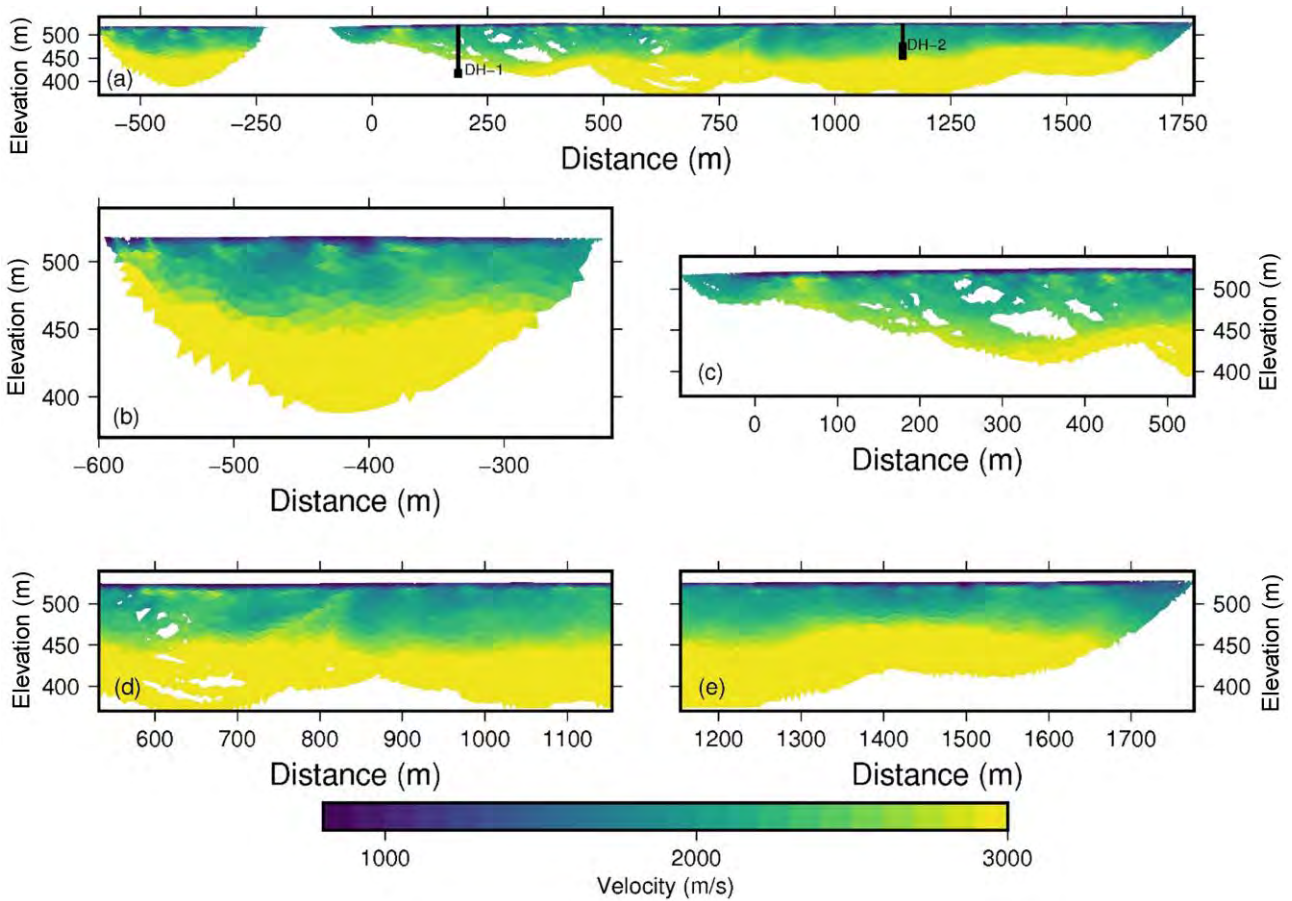


Figure 17. P-wave velocity, re-scaled to emphasise the shallow high velocity structures. (a) Results for the entire seismic refraction profile are shown with no vertical exaggeration (Y-axis units are in metres). The gap in the line was due to a corner that we were uncomfortable operating on because of road traffic the location of the drill holes are plotted for reference. The thick part at the bottom of DH-1 and DH-2 is where the drill-log marked “Weathered granitic rock, possibly gneissic. Coarse to very coarse-grained quartz sand sized fragments and kaolinitic clay”. Panels b–e show sub-survey details; (b) The short profile; (c) -90–532 m; (d) 532–1154 m; (e) 1154–1776 m.

4.3.2 SEISMIC REFLECTION

The seismic reflection results show significant structure and lateral heterogeneity across the 1.7 km of profile (Figure 18). The reflection data set provides significantly more detail than the refraction data set. The way that the data are processed means that the amplitudes observed in the section are caused by continuity (more lateral continuous over 10s of meters) opposed to how strong the velocity contrast is. The key observation are large amplitude and continuous reflectors that begin around 100 m depth (~ 400 m elevation). It is surprising to see how steep the edges of the palaeovalley are. The slope of the major reflector is ~ 1 m/m on the eastern end of the line (Figure 18b). The slope of the valley bottom is less steep on the Kaltjiti/Fregon end with a slope of approximately 0.25 m/m (Figure 18e). The other observation is that there are multiple reflectors that make up the transition to bedrock. In this case the bedrock is probably fractured. These images will be difficult to confirm because boreholes in the area tend to stop before reaching the interesting structure observed in the reflection data. This means that it is unclear exactly which reflector corresponds to the top of bedrock, but it a reasonable interpretation to follow the start of the strong reflections and call that bedrock. This reflector is well defined over the entire line.

The geometry used in this survey was unable to resolve the stratigraphy within the palaeovalley. This was because we sacrificed the top 40 m to cover significant ground in the five days we had in the field. It was originally thought that we would be able to pull some structure from the files but the surface wave energy is too strong and the geophones are too far apart to apply filtering. There are two other reasons why we

might not see reflections but they need to be investigated further. The first stems from the observation of lateral velocity changes in the refraction data set (Figure 16 and Figure 17). This might suggest, although unlikely, that the material in the palaeovalley is not laterally continuous. The more likely reason for a lack of reflections is that all of the material in the channel is derived from the Musgrave Ranges (colluvium or alluvium that have been calcreted) making the elastic contrast between layers too weak to generate a reflection.

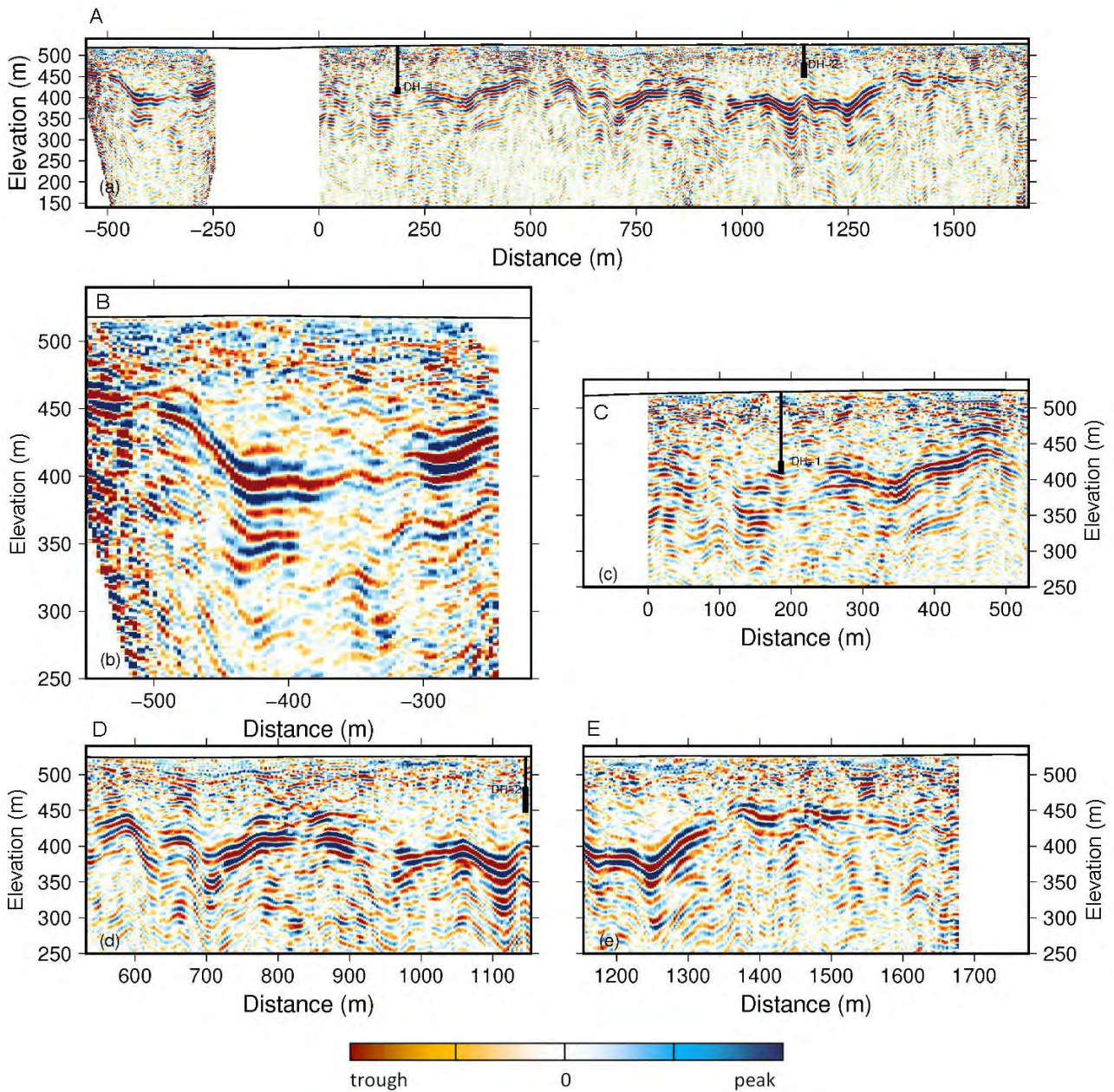


Figure 18. a) Seismic reflection results for the entire profile shown with no vertical exaggeration. Note that these are depth converted sections using a picked velocity model and uncertainty is probably +/- 5–7 m in the vertical direction. Panels (b) to (e) are zoom images so that some detail can be observed. All these sections are shown at zero vertical exaggeration: (b) The short profile. (c) 90–532 m; (d) 532–1154 m; (e) 1154–1776 m.

4.4 Data synthesis

4.4.1 FIRST ORDER BEDROCK INTERPRETATION

In this section we show the overlap between the refraction velocities and the reflectors. We then look at how the airborne interpretation matches up. In general, the high velocities (> 4000 m/s) occur below the strong reflectors (Figure 19). That is, given these two independent data sets, the bedrock boundary would have been selected in roughly the same location. The material at the bottom of the core (DH-1) still appears to be saprolite, so it remains unclear whether the reflections are caused from fractures in the underlying unweathered bedrock, or whether there is 150+ m of saprolite/saprock. Deeper drilling would be required in order to resolve which it is.

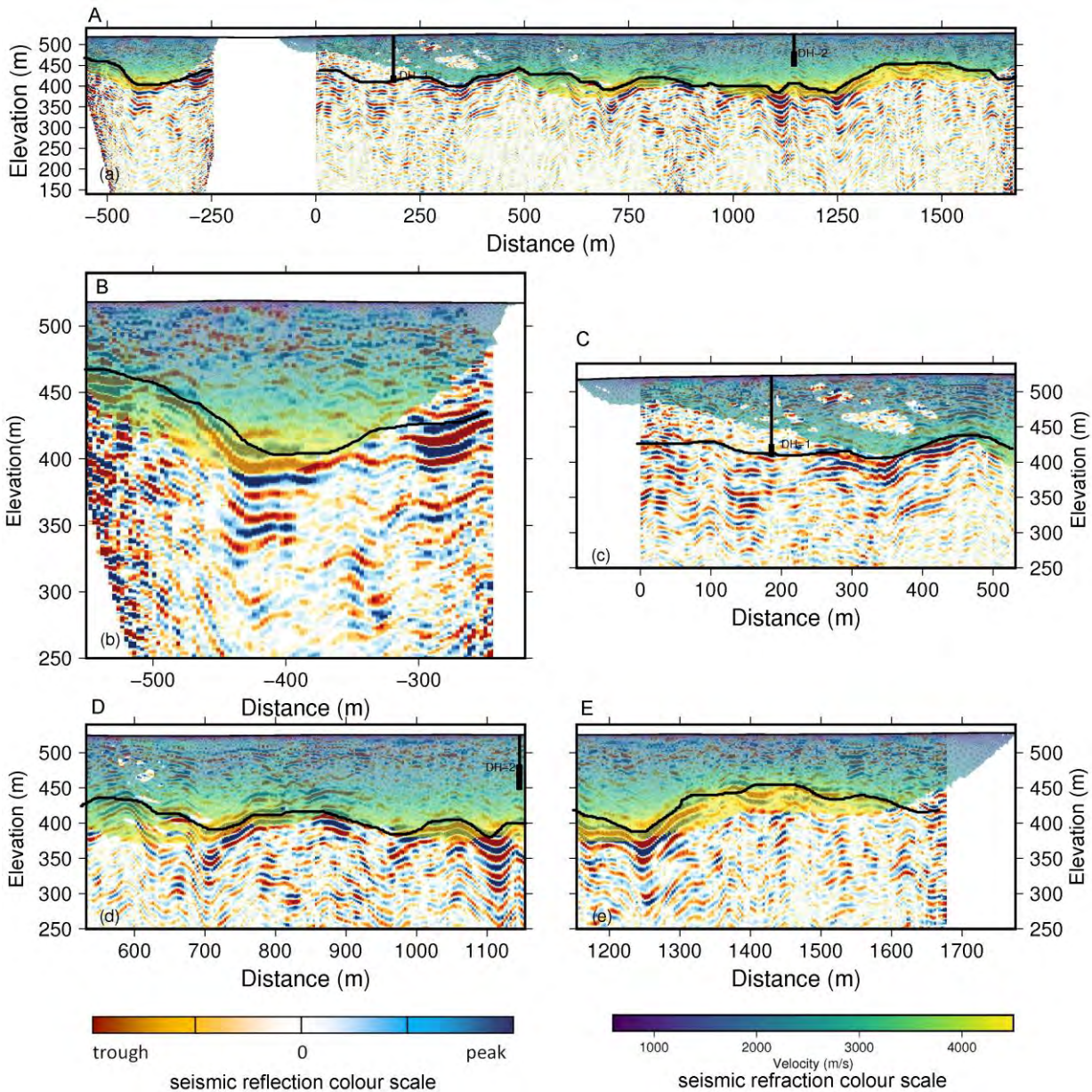


Figure 19. (a) Overlay plot showing the seismic refraction (same colour scale as Figure 16) on top of the Seismic reflection results (from Figure 18). All profiles are shown with no vertical exaggeration. A depth to bedrock prediction has been added manually (black solid line) to illustrate the match between the two methodologies; (b) to (e) are zoom images so that more detail can be observed. All these sections are shown at zero vertical exaggeration: (b) the short profile; (c) -90–532 m; (d) 532–1154 m; (e) 1154–1776 m. seismic reflection colour scale.

4.4.2 COMPARISON WITH THE AIRBORNE ELECTROMAGNETIC DATA

An electrical conductivity value has been selected where the largest change occurred (at $45 \mu\text{S}/\text{m}$). This would be considered the bottom of the palaeovalley using the airborne electromagnetic (AEM) data (Figure 20). The individual AEM lines running N–S at 250 m spacing have been interpolated to create a surface that represents the palaeo-topography (Figure 20b). In this view the palaeovalley system is evident. Furthermore, the seismic line is centred mostly over the palaeovalley, and at its deepest point the depth to bedrock, as predicted by AEM should be around 100 m depth (Figure 20c).

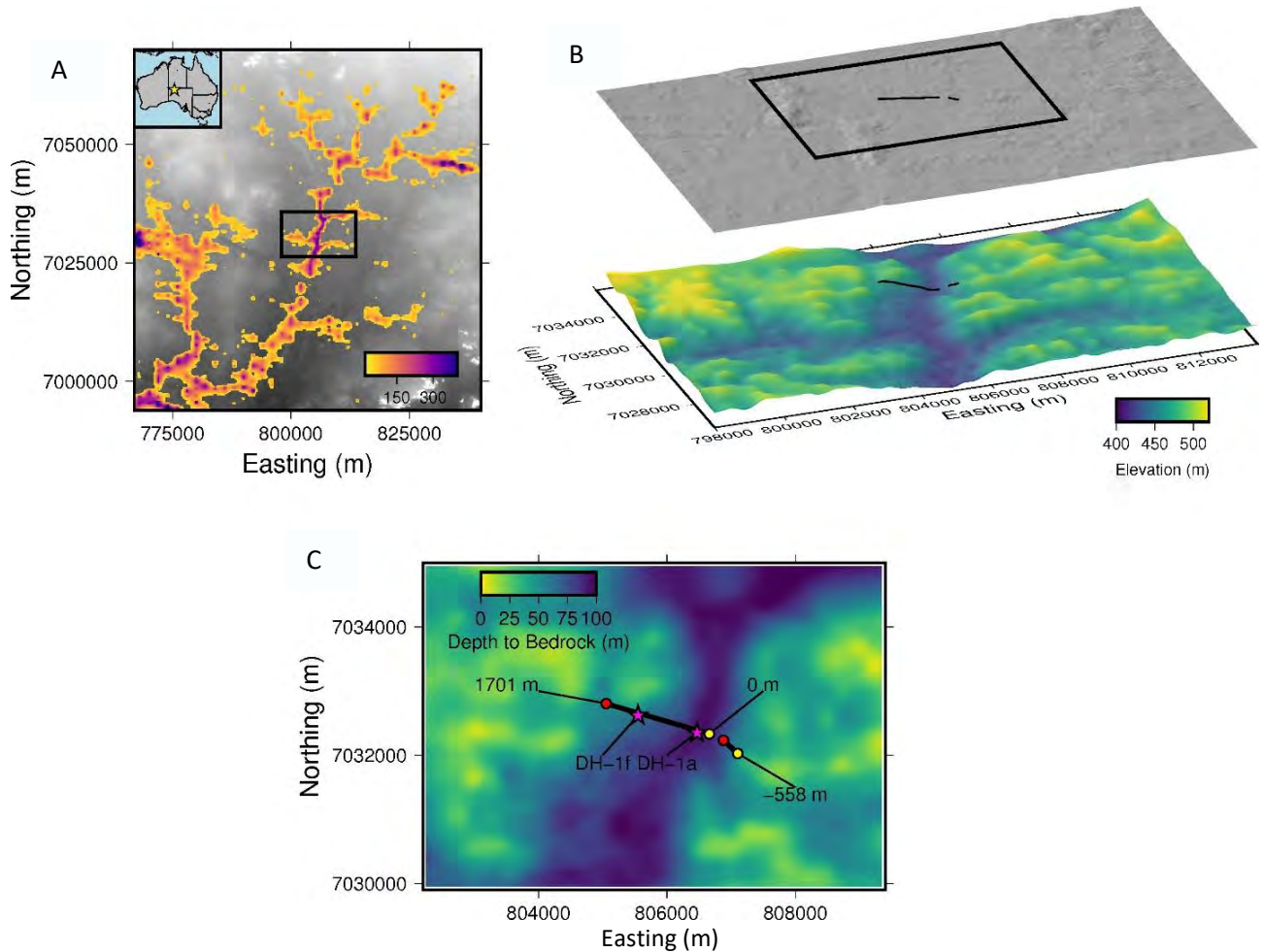


Figure 20. (a) Regional map showing 60–70 m depth section with conductivity greater than $45 \mu\text{S}/\text{m}$ masked out; (b) Perspective view of the palaeo-topography with line location shown at 10x vertical exaggeration. The surface topography has been shifted up for visualisation; (c) Final inset showing the location of seismic line and the two boreholes. Start of the lines are from 0–1701 m and from 0–558 m. This is overlaid on a depth to bedrock map (instead of elevation of ground surface) from the airborne electromagnetics.

Using the depth to the palaeovalley bottom from the airborne AEM interpretation, we can compare it to the seismic reflection (Figure 21) and seismic refraction (Figure 22) results. There are some notable differences. The airborne EM defined valley has been defined from a widely spaced survey (250m line spacing) which indicates the valley to be both broad and rolling. The base of the conductive response in the AEM matches the transition from transported sediments to saprolite as defined by drilling (Figure 21). There are a few locations, particularly in the centre of the valley where the seismic defined boundary and the airborne boundary match quite well (Figure 21). In contrast near the valley's edges, on both sides of the reflection survey, the match between the airborne and seismic deviates. This vertical deviation can be over 70 m in places. This difference appears real and is attributed to a change in the physical properties of the materials present, not a result of ambiguities associated with the airborne inversion. It is unlikely that airborne data could be matched with an alternative boundary location that is 70 m below the current predicted locations of the base of the palaeovalley system.

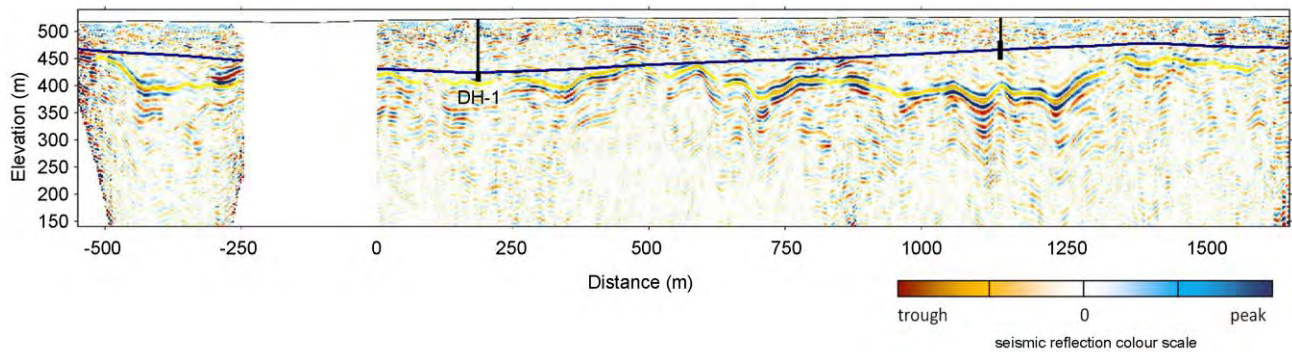


Figure 21. Results from the seismic reflection survey. Data were processed following a basic flow: 1) band-pass filtered, 2) trace normalised, 3) CMP sorted, 4) muted surface waves, 5) NMO moveout applied (one velocity per gather), 6) stacked, and 7) a time to depth conversion was applied using a single velocity. The main reflector (clearly visible in the raw CMP gathers) is highlighted in yellow. The boreholes are shown as black vertical lines. Where the black line gets thicker is where drillers intersected saprolite (*in situ* rock). The blue line is the extracted depth to bedrock value (from airborne electromagnetics) —note the large difference between 1000 and 1250 and -500 and -250 m along the profile.

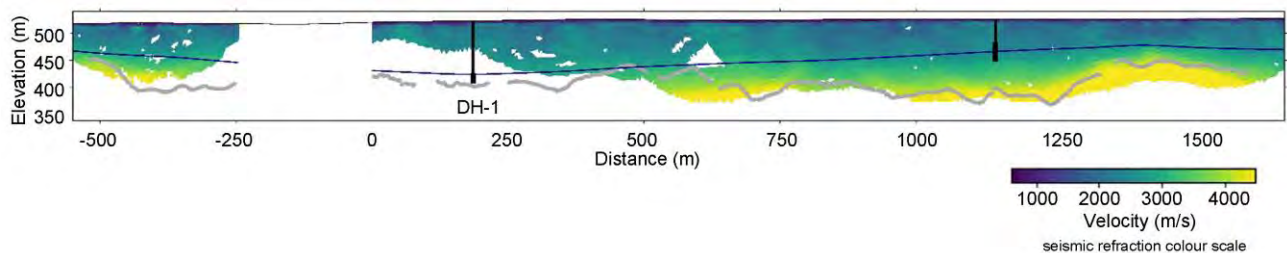


Figure 22. Results for the seismic refraction survey. The velocity model was inverted using travel-time tomography and is comprised of ~20,000 picks. Regions that are white have no ray paths passing through them. The main reflection from (Figure 21) is plotted on the image as a grey line, the blue line is from the AEM data, and the boreholes are shown as in panel a. The match between the strong reflector and strong velocity change means that the depth conversion is done well.

This discrepancy has led to a new conceptual model. Using the two data sets, the bottom of transported sediment fill appears well defined using the AEM data. The zones that lie between the airborne boundary and seismic reflection boundary have then been defined here as saprolite. This is where this new conceptualisation changes from previous work. In previous work the saprolite is always drawn as a relatively uniform layer. Here it appears that the saprolite is thickest near the valley edges and thinnest in the centre of the valley. Lastly, the cause of all of the reflections remains unclear. Thus, in the conceptual model this is marked as saprock/fractured bedrock. There are also notable regions where there are no reflections (between 250-750 m in Figure 21). These regions have been interpreted as solid and unweathered bedrock (Figure 23).

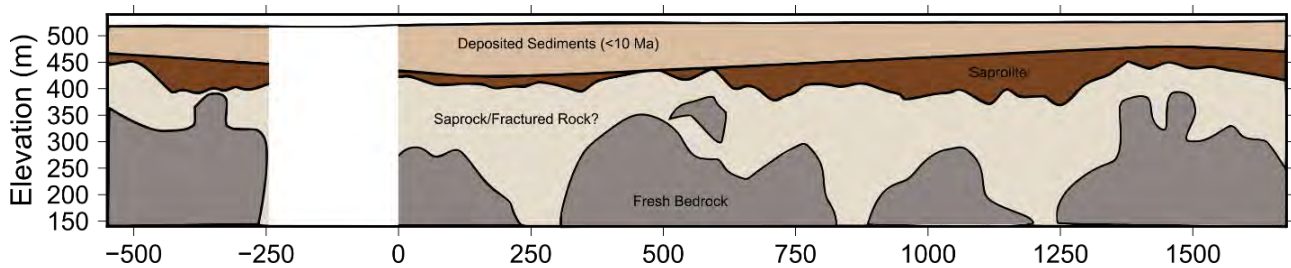


Figure 23. Preliminary conceptualisation based on the combination of airborne electromagnetics (AEM) and seismic reflection data. The base of the deposited sediments are defined by the AEM data. The saprolite is defined as the region between the reflection boundary and AEM boundary. The saprock/fractured rock is the region that has a lot of reflections. Fresh bedrock was defined by a notable lack of reflections. The biggest difference to the conceptualisation is that the saprolite thickness is not uniform (it is thickest at the edges of the valley and thinnest in the centre).

In summary, it appears from the stratigraphic borehole data that the AEM data does an excellent job at defining the bottom of transported regolith and the seismic data will define the top of unweathered bedrock (Figure 23). From a hydrologic standpoint, most of the water is in the transported cover so the AEM is an excellent tool to site new water wells. Most of the water found at DH-1 came from just above the large conductor that was identified as a clay layer in the AEM. On the other hand, if the aim is to precisely locate the top of bedrock itself (not saprolite), then the seismic refraction method is likely to be better.

Future work would benefit from integration with additional data from future surveys. Just recently borehole NMR data were collected. This shows that the porosity in the saprolite and overlying mobile regolith is similar yet the T_2 distributions change significantly. Since porosity will dominate the elastic response this explains why a clear reflection boundary is not detected here despite the pore structure changes, which could significantly impact the electrical properties.

5 Borehole nuclear magnetic resonance (BNMR)

5.1 Borehole nuclear magnetic resonance technology

Borehole nuclear magnetic resonance (NMR) methods have seen extensive use in the oil and gas industry with the first NMR logging tools developed for oil exploration in the 1960s (Brown and Gamson, 1960). The technology has improved significantly in the last few decades with the advent of new pulsed NMR tools (Coates et al., 1991; Kleinberg, 2001). The relatively recent development of small-diameter, and highly portable NMR tools (see, Walsh et al., 2013; and Trofimczyk et al., 2018) now permits the non-invasive use of this technology within existing PVC/fibreglass-cased bores or open holes that commonly support hydrogeological investigations. Concurrent with these technology developments there have been numerous theoretical, empirical, and field studies that demonstrated robust transforms between the measured NMR response and key hydraulic parameters including fluid-filled porosity (Timur, 1969), pore-size distribution (Gallegos and Smith, 1988), and permeability (Seevers, 1966; Kenyon et al., 1988). In the oil sector, borehole NMR is now widely regarded as a mature technology, supporting improved reservoir characterisation and oil production. It is now developing wider application in the mineral (mining) (see, for example, Trofimczyk et al. (2018) and Krejci et al. (2018)) and groundwater resource sectors (see, for example, Walsh et al. (2013); Dlubac et al. (2013); Kirkland and Codd (2018) and Parsekian et al. (2015)).

As borehole nuclear magnetic resonance logging offers a method to directly measure water content (free and bound), porosity, pore-size distribution, and estimates of hydraulic conductivity (see, for example, Coates et al. (1999); Dunn et al. (2002), Stapf and Han (2006); Walsh et al. (2013)) it is regarded as having significant potential in hydrogeological investigations.

The nuclear magnetic resonance effect in borehole NMR logging relies on a pulsed magnetic field that operates at right angles to the polarising static magnetic field. Whereas in surface NMR the static magnetic field is the magnetic field of the earth, in borehole NMR, the static magnetic field is produced from powerful magnets that are mounted in the sonde and lowered down the borehole. The powerful magnets create a cylindrical shell of uniform field strength that targets the rock outside the invasion or disturbed zone caused by the drilling technique (Figure 24).

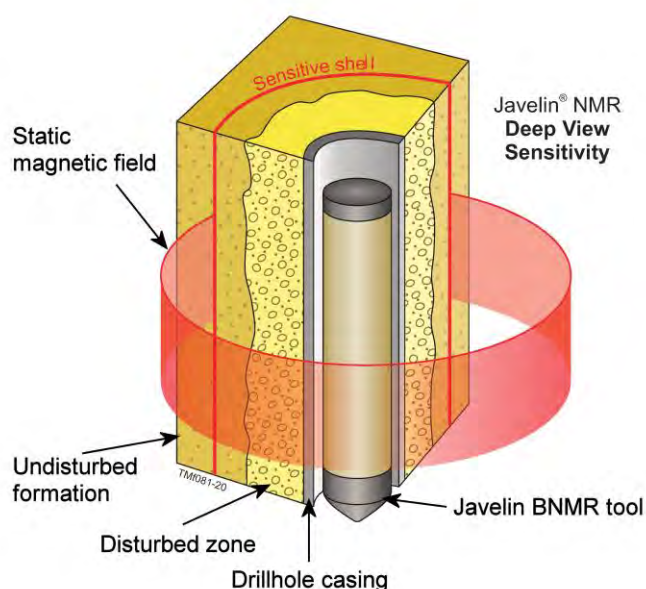


Figure 24. Cylindrical shell of uniform magnetic field strength that targets the formations outside the disturbed zone to water content and pore size/porosity (adapted from Vista Clara Inc. 2017).

The resonant magnetic field in borehole NMR is caused by an oscillating electromagnetic field at right angles to the primary static field. Since the magnetic field strength of the static field is very many times more powerful than the magnetic field of the earth, the resonant Larmor frequency in borehole NMR applications is typically on the order of hundreds of kiloHertz (as opposed to 1500–3000 Hz in surface NMR applications).

At a given depth, a borehole NMR measurement is made by observing the relaxation of the NMR response. This is achieved by using a pulse sequence called the CPMG, named after its inventors Carr, Purcell, Meiboom and Gill (Cowan, 1997), which produces what is known as a spin-echo train. The spin echo train is used to mitigate the effects of de-phasing in the spin resonance state due to inhomogeneity in the static magnetic field. A series of short magnetic pulses are generated by the radio-frequency (RF) coil in the sonde which stimulate the hydrogen protons into resonance. Between each pulse, a re-phasing of the nuclear magnetic spins creates a small secondary magnetic peak that is recorded by a pick-up coil. The re-phased peak is called a "spin-echo", since it occurs out of phase of the stimulating peak, and the magnetic field so created is formed from the magnetic dipole moment of the protons as a result of their spin. The series of spin-echo peaks is called an "echo train", and it is this which is analysed for the sounding. A diagram of a spin-echo train from a GPMG pulse sequence is shown in Figure 25.

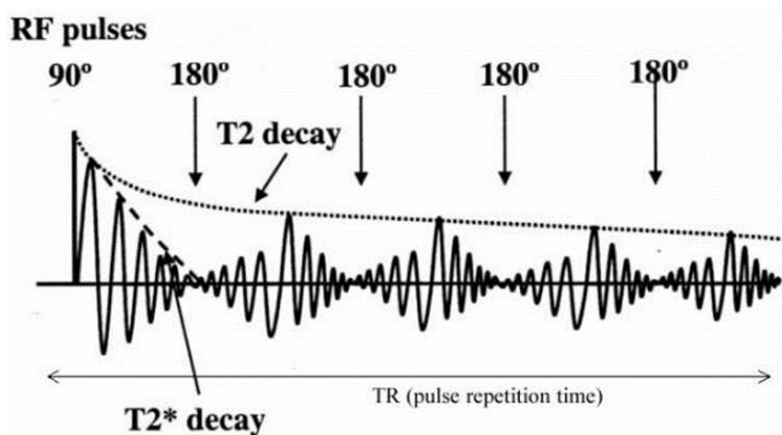


Figure 25. Diagram of the spin echo train from a CPMG pulse sequence for nuclear magnetic resonance (NMR) measurement. The time decay measured by the borehole NMR tool is the T₂ decay, which is estimated from the peak amplitude of every echo in the spin echo train. Image from: <http://www.iomonitoring.pro/mrphysics.htm> .

In order to reduce the effects of noise and to increase the signal to noise ratio, the CPMG sequence is repeated many times during a typical sounding. The number of times that the spin-echo response needs to be done depends upon the diameter of the borehole tool being used and the strength of the static magnetic field used to polarise the spins. Noise processing, filtering and fitting of the spin echo trains is completed using proprietary software. Each train is filtered and fitted in order to estimate the peak amplitude of each spin echo response in the train. The resulting decay curve represents the T₂ response of the hydrogen atoms in the subsurface surrounding the static magnets and influenced by the resonant magnetic field. The initial amplitude of the T₂ response (extracted back to time t = 0) is a direct indicator of the total water content in the volume that is being measured by the borehole NMR tool, while the rate of decay of the T₂ curve indicates pore volume (in the saturated zone, since we assume that the total pore volume has been filled with water).

The T_2 decay is modelled by a superposition of exponential decays that are weighted to fit the decay curve. Selection of the individual components of T_2 (the basis set) that can contribute to the decay curve is made by the interpreter and the interpretation software fits the best contribution of exponential decays to the T_2 in order to estimate pore-size distribution (Coates et al., 1999). An example of a T_2 decay curve, its best fit, and the basis function used to create the best fit are shown in Figure 26 and Figure 27. We see in these figures that extrapolation of the linear best fit model to time $t = 0$ s shows that the total water content for this sounding is 30%. Figure 27 gives us an indication of how much of the water present is contained in small pore spaces (low values of T_2 in the basis set), and how much of the water is mobile (or contained in larger pore spaces, i.e. high values of T_2 in the basis set). The bimodal distribution of T_2 in the basis set in Figure 27 indicates that there is both free and bound water present at this depth, but that there is slightly more free water present than bound water.

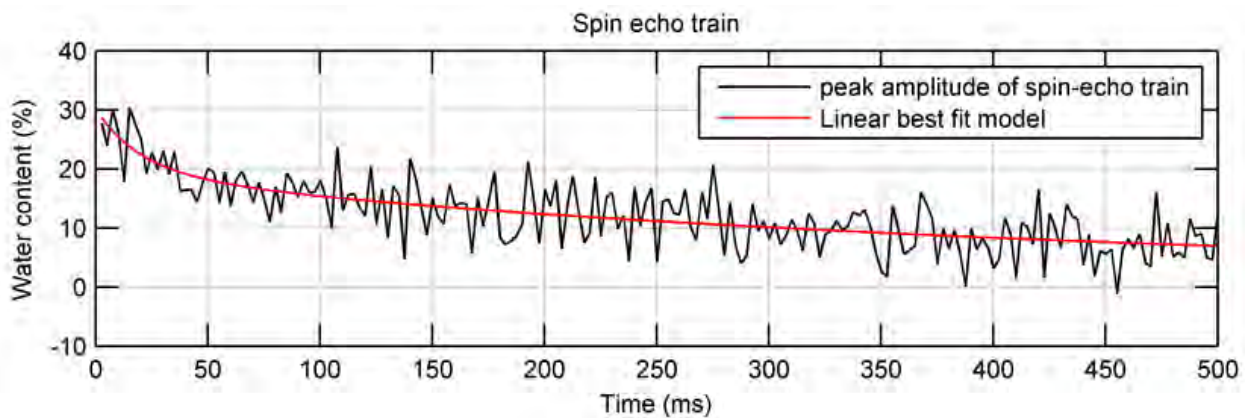


Figure 26. Measured, stacked, and filtered T_2 decay curve for a borehole nuclear magnetic resonance (NMR) measurement in (black line) and the linear best fit model that is used to fit the decay data (red line).

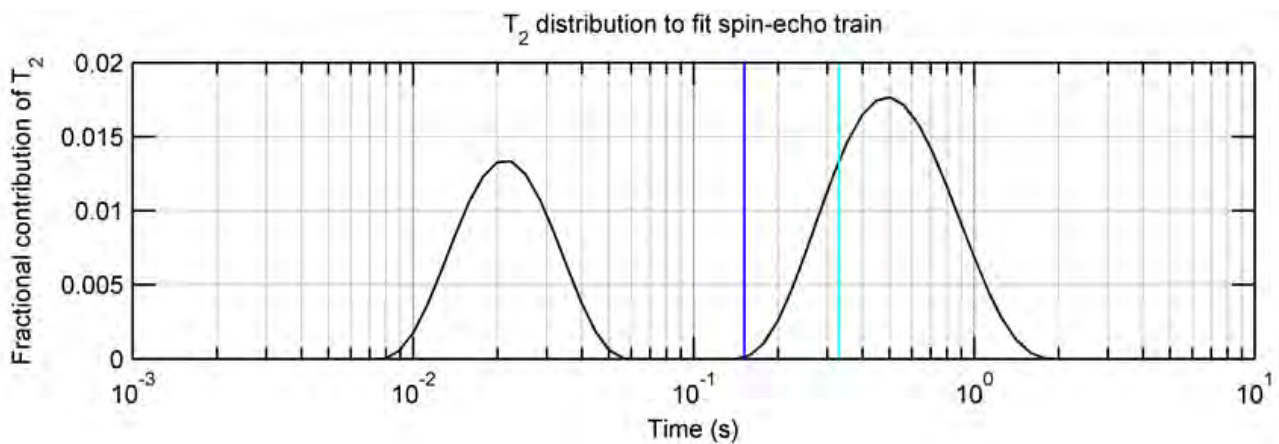


Figure 27. Basis function of the exponential decays used in creating the red curve in Figure 26. Note there are two distributions of T_2 in the basis set, indicating both bound (left) and mobile (right) water.

5.2 Borehole nuclear magnetic resonance inversion

As explained in the previous section, the averaged and filtered spin echo train at each depth is fitted with an exponential decay curve that is formed from a porosity- T_2 distribution (Figure 27). The T_2 decay curve is also converted from measured amplitude versus time curve to total water content versus time curve (a result of the tool calibration in both air and in a wholly saturated solution). We thus have measurements of water content, fractional porosity and T_2 distribution for each depth. These results can be used to estimate free and bound water content in the subsurface through selection of a cut-off T_2 , below which we say that the water present is bound, or contained in pore spaces too small for water to be freely productive. Water content above $T_{2cut-off}$ is considered to be mobile, which is that water will flow as a result of pumping. In consolidated sandstones typical of the Gulf of Mexico, the cut-off time separating bound and mobile water is $T_{2cut-off} = 33$ ms, while for carbonates, $T_{2cut-off}$ is often taken as 92 ms (Coates et al., 1999). These values are arbitrary, but compare well to laboratory test data of several sandstone and limestone. In this survey, we use the cut-off values of 33 ms (blue vertical line in Figure 27), since little is known about sandstone and limestone $T_{2cut-off}$ values in unconsolidated sandstones and carbonates for near-surface applications.

Hydraulic permeability

The hydraulic permeability of a material is the ability of the material to transport water as a result of some production method (for example, a pump test on a borehole through its screened section). Among the properties borehole NMR offers is an estimate of permeability k or hydraulic conductivity K (Walsh et al., 2013; Behroozmand et al., 2015). Three different methods can be used to estimate hydraulic permeability from the water content and T_2 distributions. These are: 1) k_{SDR} : Schlumberger-Doll Research (SDR) equation (Dunn et al., 2002); Equation 4; 2) k_{TC} : Timur-Coates (TC) estimate (Stapf and Han, 2006) and 3) k_{SOE} : Sum of Echoes (SOE) estimate (Dunn et al., 2002) (Equation 5). Each method is known to provide better estimates in some aquifers over others, however, each method needs to have reliable pump-test or aquifer test data to fully calibrate for an area of interest. In each case, the estimates of hydraulic permeability can be taken as *relative* hydraulic permeability values (Walsh et al. 2013, Behroozmand et al. 2015). We employed two of the more commonly applied estimation methods (SDR and SOE) in this study, with the equations and parameters given below:

$$k_{SDR} = C_{SDR} \Phi^4 T_{2ML}^2 \quad (\text{Eq. 4})$$

$$k_{SOE} = C_{SOE} \left| \sum_{n=1}^N E_n \right|^2 \quad (\text{Eq. 5})$$

In Equation 4, k_{SDR} is the Schlumberger-Doll Research equation conductivity estimate, C_{SDR} is a lithology-specific coefficient, Φ is the porosity of the material at a given depth, and T_{2ML} is the weighted logarithmic average of the T_2 distribution (blue line in Figure 27). In Equation 5, k_{SOE} is the sum-of-echoes conductivity estimate; and C_{SOE} is a coefficient. The value for k_{SOE} is estimated by squaring the sum of all echoes E_n in the sounding stack, and multiplying the sum by the coefficient specific to a given soil-type. In each case, the multiplier coefficients must be chosen based on the material that is being studied. In this study, we have used the coefficients for Gulf sandstone as an estimate of relative hydraulic conductivities in sediments of the Lindsay East palaeovalley in the APY Lands. Arguably this is a reasonable starting point as some of the sediments encountered in the drilling were cemented sandstones (see Keppel et al. (2019), and Krapf et al. (2019)). This approach can be used to estimate permeability as a linear function of the squared echo decay curve which is measured by the borehole NMR tool (Walsh, 2008).

5.3 Field data acquisition

In the study at the G-Flows Stage-3 sites (Figure 1) we used the Vista-Clara Inc. Javelin JP350 borehole NMR tool (Walsh et al., 2010). The tool choice was determined by the nominal diameter of the PVC casing (between 155 and 177 mm) and the width of the drilling method employed (see Keppel et al., 2019). Bores logged and depth of logging are detailed in Table 1. Basic well construction details of the bores logged are given in Table 2.

Table 1: Bore name and depth of logging for borehole nuclear magnetic resonance logging.

BOREHOLE	DEPTH LOGGED (m)
DH1a2	82
DH1a	93
DH1b	55
DH1c	47
DH1d	51
DH1f	66
S22i	11.6

The Javelin JD350 is 89 mm in diameter and performs measurements at four simultaneous frequencies to obtain measurements for four discrete diameters of investigation (Figure 28). Measurements from each shell (see Figure 24) can be combined in post-processing to improve data quality or can be analysed individually to assess radial variation. Diameters of investigation for the JD350 are 27 cm, 30 cm, 34 cm and 38 cm. Available drilling logs (Keppel et al., 2019) suggested that only data from the lower frequencies would be from the undisturbed formation. This influenced the choice of shells used in the data analysis and interpretation.

Table 2: Well construction detail for bores logged with borehole nuclear magnetic resonance. Source: Keppel et al. (2019).

UNIT NO.	NAME	PERMIT NO.	CONSTRUCTION DATE	FINAL DEPTH (m)	ZONE	EASTING	NORTHING	STUDY SITE	SCREEN LENGTH (m)	AQUIFER MONITORED	WELL DESIGN
534400087	DH1a	294909	1-Sep-18	117	53	209961	7032742	DH1	No screen	NA	Deep Observation/ Production Well
534400078	DH1a2	330199	3-Sep-18	112.7	53	209953	7032689	DH1	3	Fractured Rock	DH1a2 Observation Well
534400089	DH1b	294912	28-Aug-18	59.9	53	209984	7032828	DH1	3	Palaeovalley	Deep Observation/ Production Well
534400080	DH1c	294911	13-Aug-18	57.5	53	209954	7032745	DH1	6	Palaeovalley	Deep Observation/ Production Well
534400082	DH1d	294910	28-Jul-18	61.4	53	209959	7032719	DH1	6	Palaeovalley	Deep Observation/ Production Well
534400085	DH1f	294913	11-Aug-18	77.35	53	209019	7032973	DH1	6	Fractured Rock	Shallow Observation Well
534400088	DHS22i	330198	25-Aug-18	51.8	53	206201	7040059	S22	3	Phreatic	Deep Observation/ Production Well

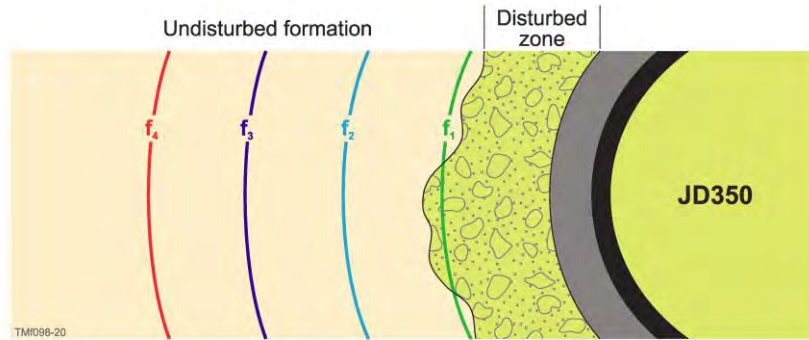


Figure 28. The JD350 borehole nuclear magnetic resonance tool acquires data for four frequencies to obtain measurements away from the disturbed zone. Data from each shell can be combined to improve data quality or they can be examined and interpreted separately. Adapted from Vista Clara Inc. (2017).

At each logging depth interval, two scans, Tr1 and Tr2, were performed with different values for the relaxation time between CPMG pulses (4 and 1.6 μ s), the length of each CPMG pulse (200 and 80 ms) and number of averages (4 and 24). The Larmor frequencies used for the JP350 were F1:437 kHz, F2:365 kHz, F3:301 kHz and F4:256 kHz, sampled at 80,000 Hz. At each site, a radio-frequency noise cancellation device was used to eliminate near-surface noise during the soundings. Logging time for each depth interval averaged 6 minutes, owing to the relatively slow measurement time of the NMR signal. Data processing, stacking and filtering was conducted using software developed by Vista-Clara Inc; the coefficients and cut-off times used for each hydraulic conductivity and porosity estimate are given in Table 3. The tool was deployed is shown in Figure 29, with operational control arranged from a field vehicle as shown in Figure 30.



Figure 29. Setting up of the Vista Clara Borehole nuclear magnetic resonance logging tool over DH1a.



Figure 30. Winch and Borehole nuclear magnetic resonance controller in field data acquisition configuration.

Table 3: Coefficients and cut-off times used in borehole NMR processing.

COEFFICIENT AND $T_{2CUT-OFF}$	VALUE
C_{SDR}	8900
C_{SOE}	4200

* average = one full CPMG sequence.

5.4 Borehole nuclear magnetic resonance interpretation

For each of the logged bores, we show the T_2 distribution, free, bound and total water content, and estimates of hydraulic conductivity (SDR and SOE) with depth. Where available, inductive conductivity logs are included in the depth profiles. Data was processed using the software provided by Vista-Clara Inc. (Walsh 2008) using the parameters given in Table 2.

An assessment of the lithology logs for all the bores in the immediate vicinity of DH1a indicated a significant heterogeneity in the makeup of the sediment package that characterised the Lindsay East Palaeovalley fill and overlying transported cover. The upper ~30m which is interpreted to comprise the fluvio-aeolian sandplain deposits, indurated in places, with pedogenic calcrete present in the near surface (Krapf et al., 2019). Underlying these materials younger fluvial deposits of the valley fill sediments are defined. In the deepest part of the palaeovalley (~65 m below ground surface at DH1a – see Figure 31), these sit over fluvial-lacustrine materials associated with brackish estuarine/marginal marine facies (Krapf et al., 2019). Induration is commonplace through the sedimentary sequence with the development of sandstones, calcretes, silcretes, claystones and mudstones (See Figure 31 to Figure 36). The lacustrine/marginal marine facies are underlain by fine to coarse-grained fluvial sands which, in turn overly clay-rich saprolite after granite (Krapf et al., 2019).

With groundwater levels at around 8 m below the land surface for all the bores around DH1a, most of the BNMR logs are in the saturated zone. Measured inductive conductivity is relatively low, generally less than 150 mS/m, except in the deepest part of the palaeovalley where it approaches 350 mS/m. Groundwater quality, sampled during drilling was variable, but ~1000–1500 mg/L in the upper part of the sedimentary package, increasing slightly with depth, but dropping to less than 1000 mg/L in certain parts of the sequence (see Keppel et al., 2019; and Costar et al., 2019).

All the bores logged in around DH1a (see See Figure 31 to Figure 35) indicated that estimated porosities from the BNMR to be highly variable, both vertically and laterally. Estimates of bound (capillary) and free or mobile water vary significantly, averaging from 15–20% in the upper ~40 m. Trends in the mobile and capillary water content also suggests fining or coarsening upward sequences which are not always reflected in the lithology logs. In part that may reflect limitations in the drilling procedure employed which involved air rotary and mud rotary methods with drill cuttings used to define the lithology. With both approaches, there is potential to misinterpret the relative abundance of finer-grained materials. The lithology log in Figure 37 (for DH1a) was determined from diamond drill core, and more accurately defines textural changes in the sedimentary package.

Measured variations in porosity and modelled hydraulic conductivity (K) from the BNMR are highly variable in the bores logged (Figure 31 to Figure 36). Keppel et al. (2019) noted that the variable development of induration through the upper 60 m of the palaeovalley sediment package would result in a grossly bimodal porosity, with small-scale primary porosity controlled by grain size and grain distribution, accompanying a larger scale secondary “mega”-porosity controlled by zones of induration. They also suggested that this could have an important influence on localised aquifer hydrodynamics. While the BNMR results support the assertion of a highly variable porosity vertically, the lateral heterogeneity in both modelled water content and K (that is the variability between closely drilled bores) also suggests that significant horizontal porosity variations are also present. Although induration may affect primary porosity, a secondary porosity controlled by solution cavity, micro-fracture and the influence of vegetation (root channels etc) is also likely. The variable hydrogeological properties of upper unit, and by extension, the capacity of the unit to be a productive aquifer may be highly variable and dependent on the heterogeneous distribution of secondary porosity development. Costar et al. (in press), remark that their aquifer testing was equivocal, and that their results were unclear as to whether the sequence from the water table to the main water bearing zone (~9–65 m below land surface) is one sequence and fully connected or separate systems (i.e. unconfined). They indicated that further testing was required to resolve this.

In the upper 40 m of the palaeovalley fill, mobile water content (water that would be more readily pumped), averages between 5 and 10%, but there are zones in some bores where the mobile water content is significantly higher. For example, in bore DH1c (Figure 33), between 40 and 50 m, mobile water exceeds 20% in places. In DH1d (Figure 34) a similar zone of high mobile water content (and suggested porosity) is noted between 17 and 22 m. This pattern is repeated in S22i, located on a tributary valley to the main Lindsay East Palaeovalley (Figure 1), where a zone of mobile water between 30 and 35 m coincides with the presence of a coarse-grained sandstone unit (Figure 36). Costar et al. (2019) and Keppel et al. (2019) identified a target water-bearing zone (55–65 m deep) referred to Unit 1b, where sampled groundwater salinities were lower (~870 mg/L), with yields of 10–18 L/s (in bores DH1b, DH1c, DH1d). Hydraulic conductivities for this zone were estimated at ~50 m/day (Costar et al., in press). Hydraulic parameters were estimated by conducting step drawdown tests and a constant rate discharge test (over a 12-hour continuous pumping period). Unfortunately, the BNMR could not log these intervals, but in bore DH1a2 and DH1a (Figure 31 and Figure 37) these zones were logged. In DH1a2 (Figure 31), a zone of higher porosity and mobile water content was noted for that depth interval, but similar and higher average porosities were also present higher in the profile.

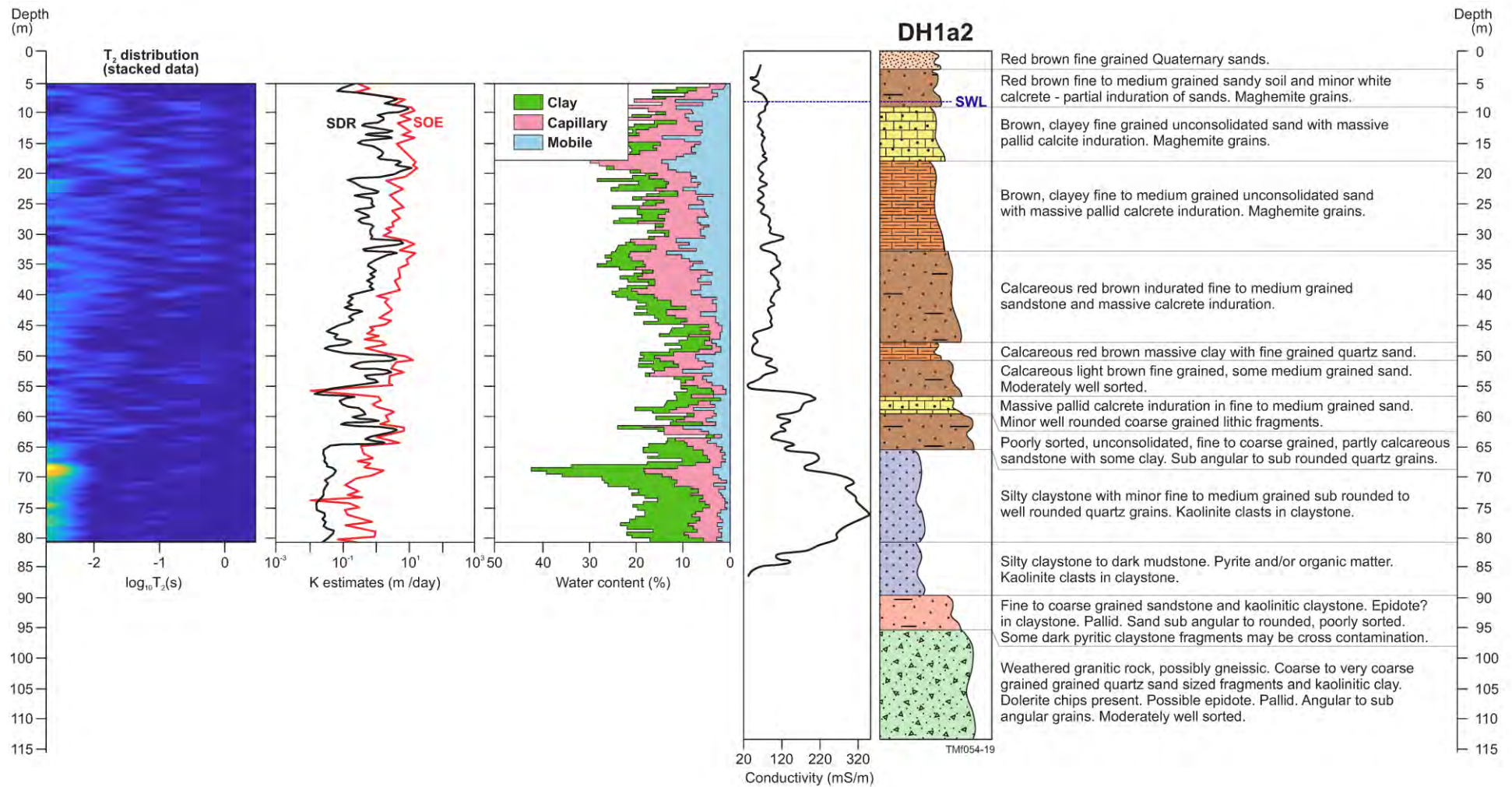


Figure 31. Borehole nuclear magnetic resonance logging for DH1a2, compared to drilling lithology and an inductive conductivity log. Location of borehole given in Figure 1. Lithology log is sourced from Keppel et al. (2019).

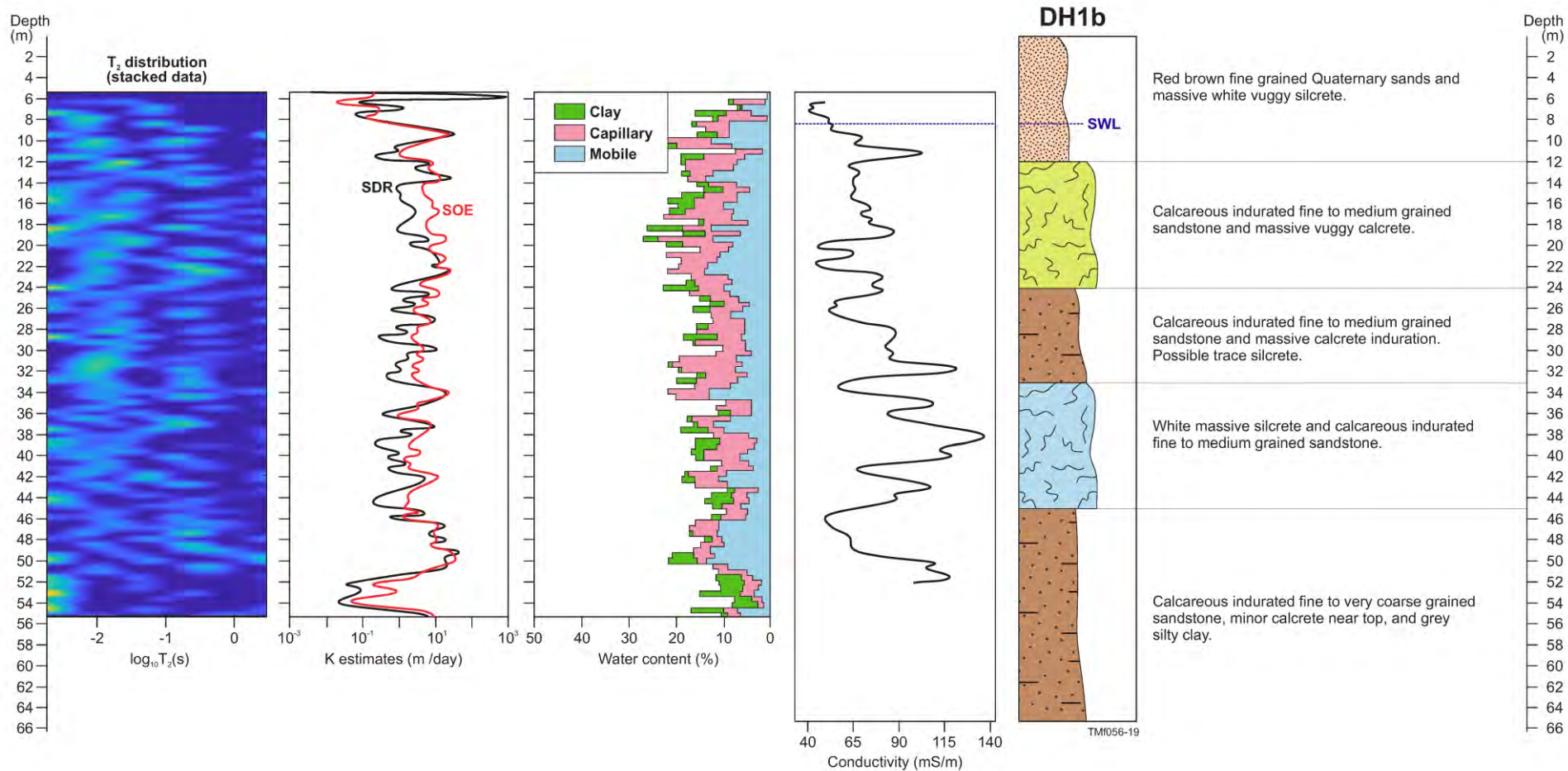


Figure 32. Borehole nuclear magnetic resonance logging for DH1b, compared to drilling lithology and an inductive conductivity log. Location of borehole given in Figure 1. Lithology log is sourced from Keppel et al. (2019).

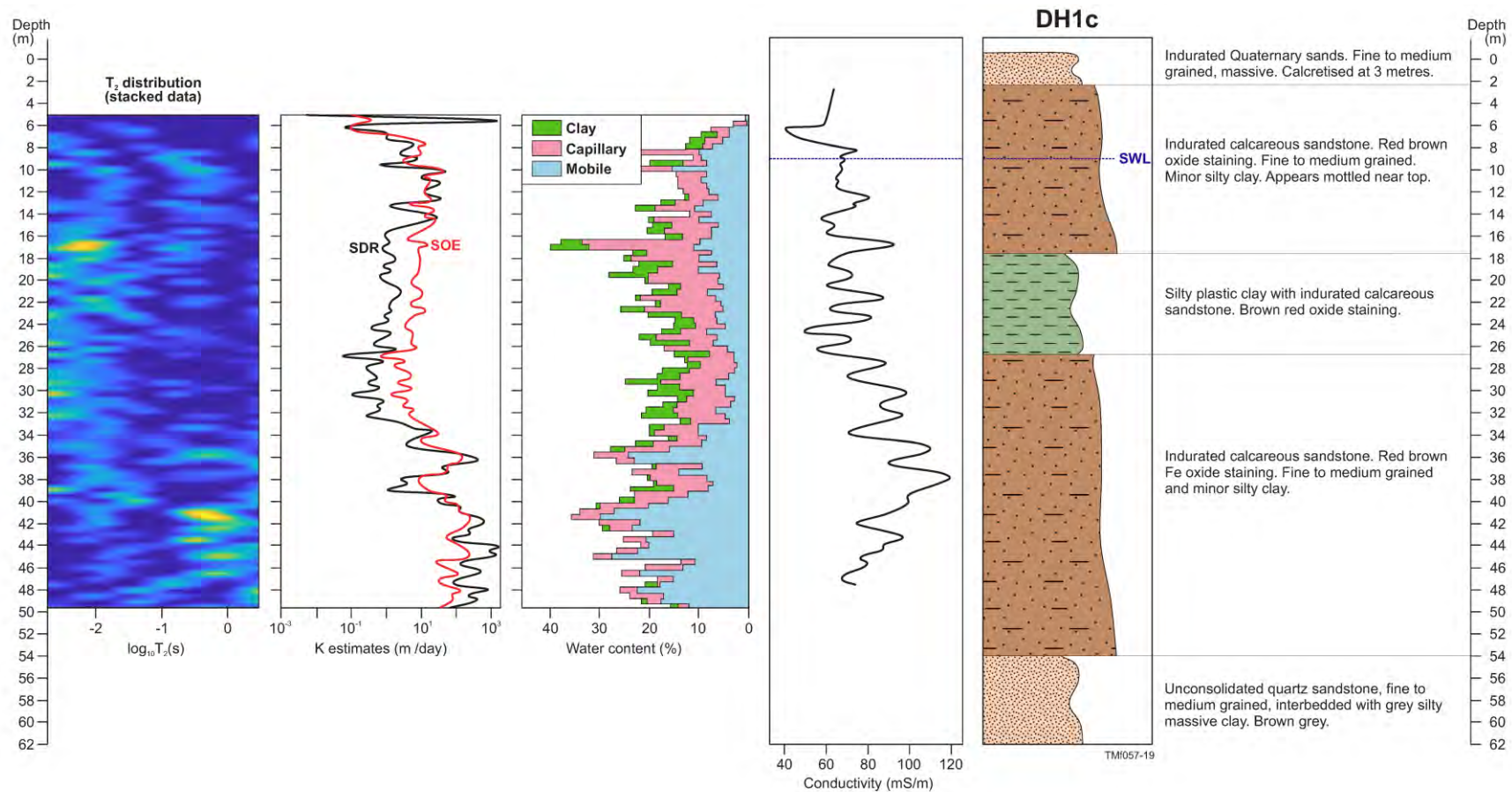


Figure 33. Borehole nuclear magnetic resonance logging for DH1c, compared to drilling lithology and an inductive conductivity log. Location of borehole given in Figure 1. Lithology log is sourced from Keppel et al. (2019).

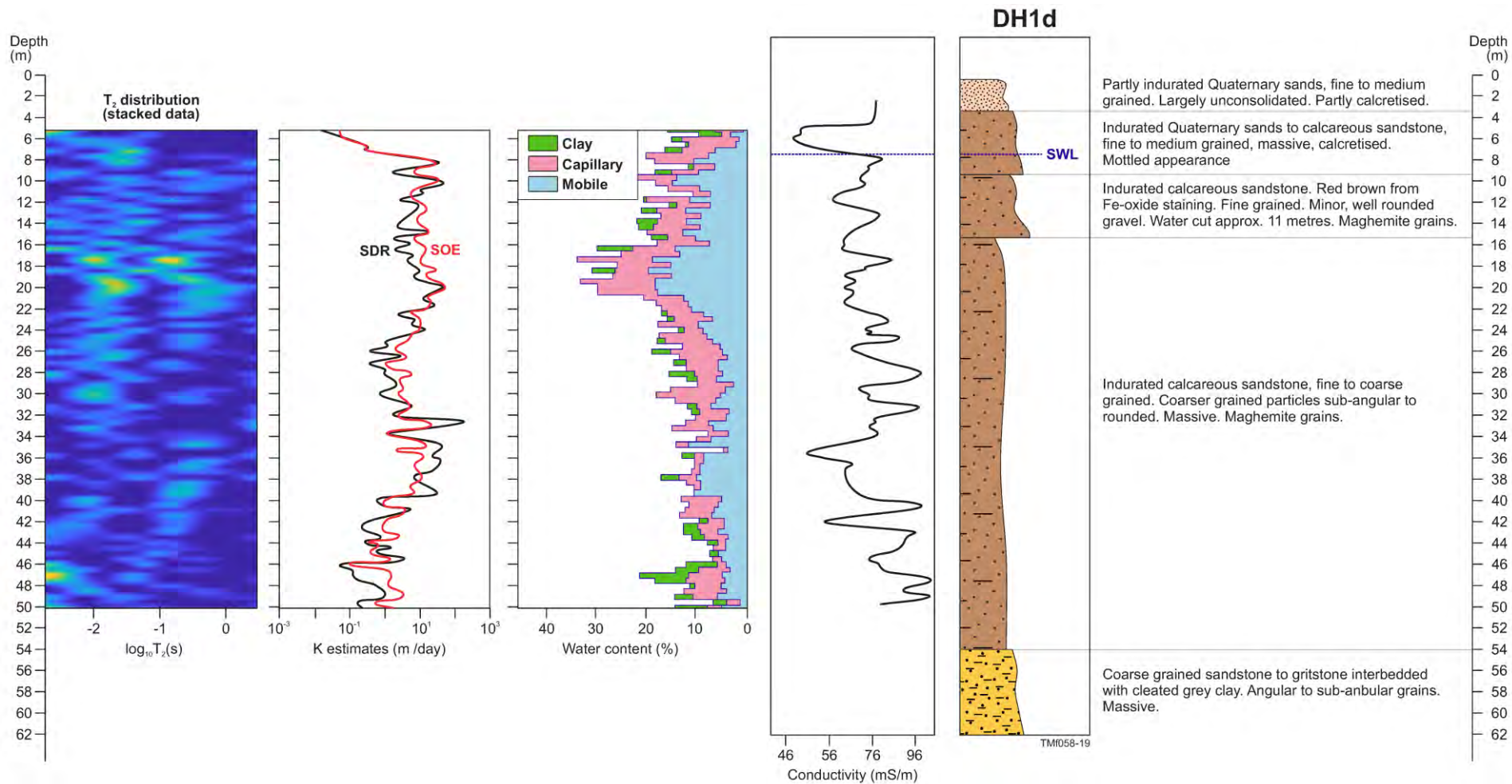


Figure 34. Borehole nuclear magnetic resonance logging for DH1d, compared to drilling lithology and an inductive conductivity log. Location of borehole given in Figure 1. Lithology log is sourced from Keppel et al. (2019).

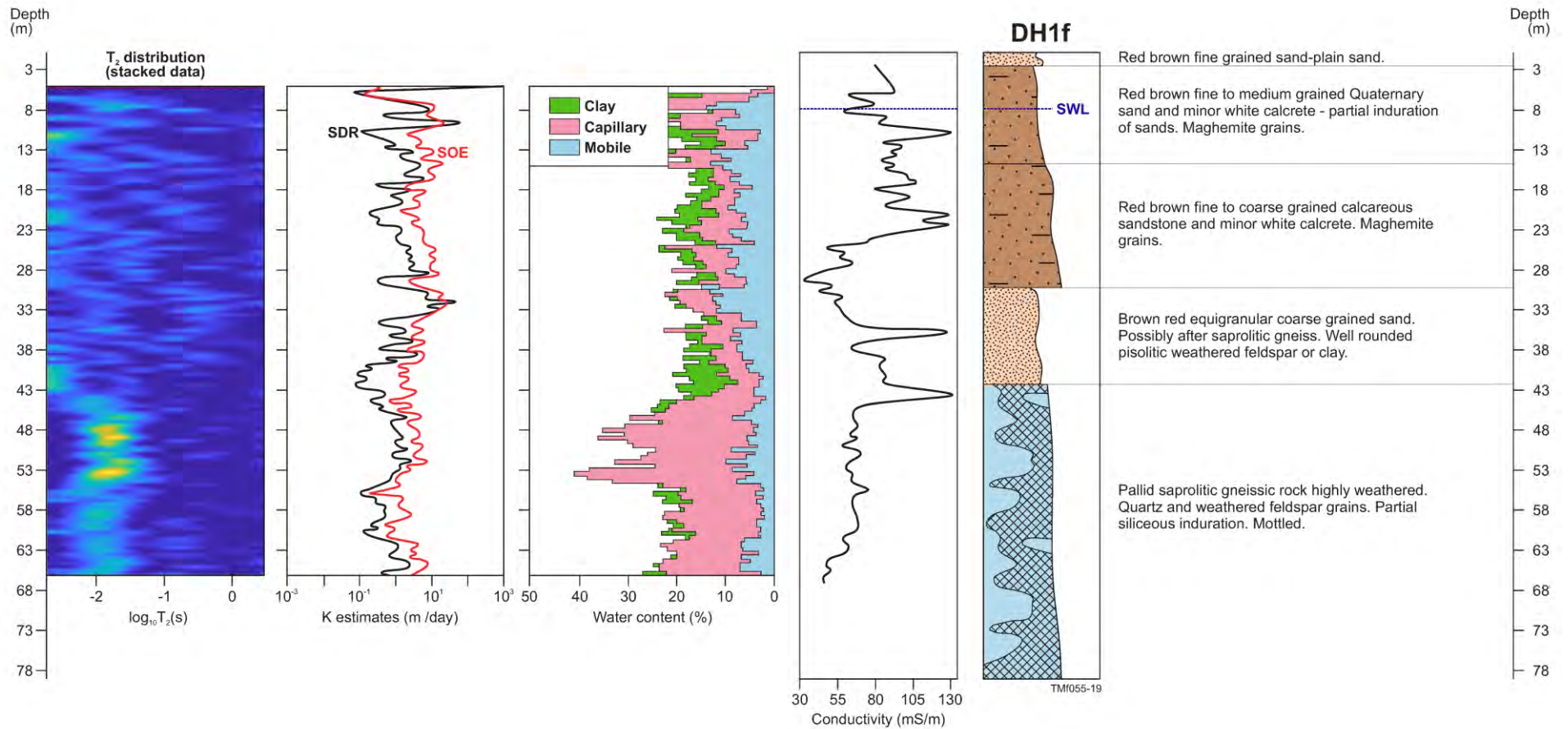


Figure 35. Borehole nuclear magnetic resonance logging for DH1f, compared to drilling lithology and an inductive conductivity log. Location of borehole given in Figure 1. Lithology log is sourced from Keppel et al. (2019).

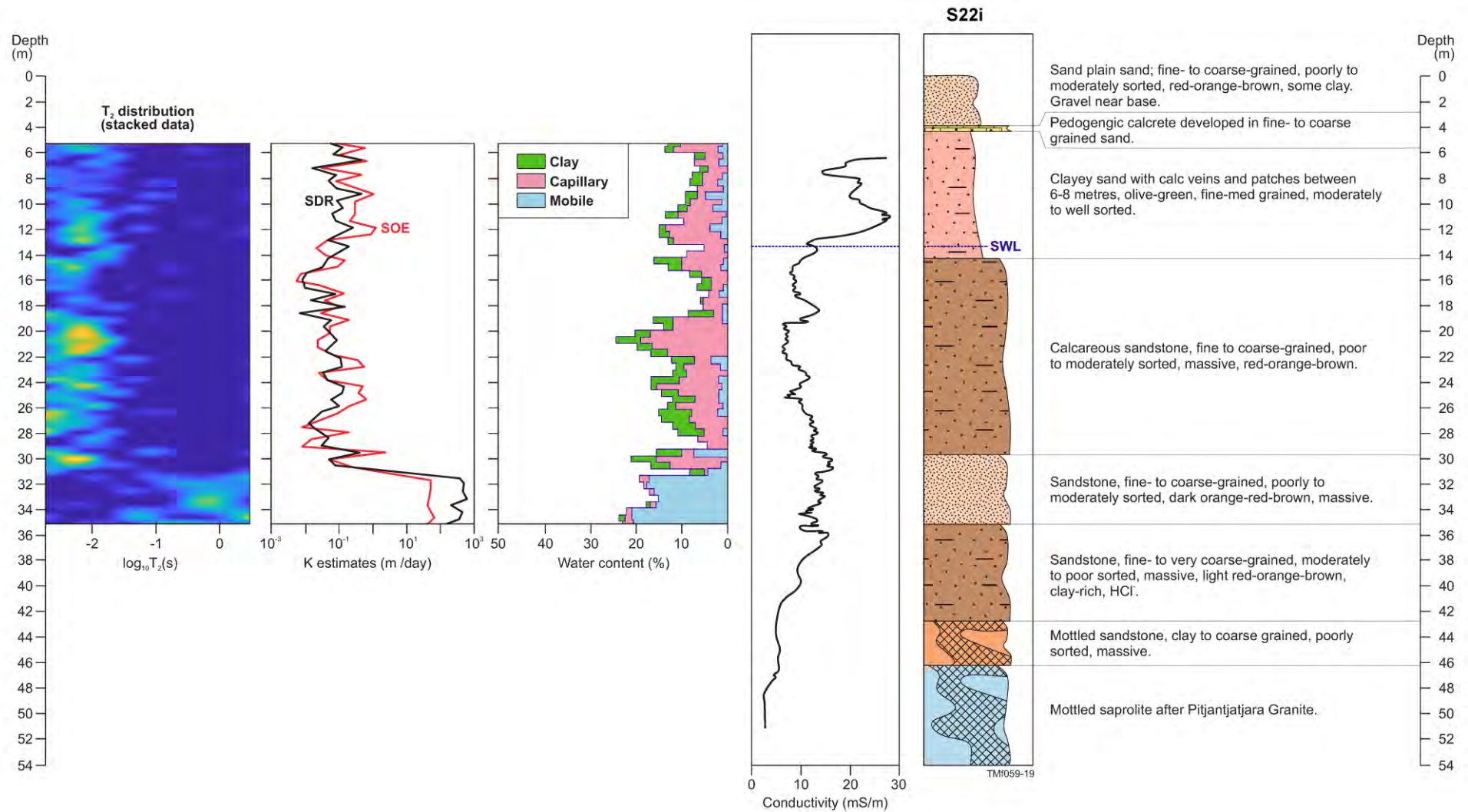


Figure 36. Borehole nuclear magnetic resonance logging for S22i, compared to drilling lithology and an inductive conductivity log. Location of borehole given in Figure 1. Lithology log is sourced from Keppel et al. (2019).

For bore DH1a (Figure 37) very high mobile water contents were noted in the base of the hole, coincident with the presence of older fluvial deposits that sit atop the saprolite. Low inductive conductivities (hence low groundwater salinity) were also noted with this unit. The modelled estimates of hydraulic conductivity exceed 50 m/day. This suggests that the lowest part of the palaeovalley sedimentary fill sequence, described as proximally transported fluvial sands and residual sand, may be high yielding but it remains untested. Spikes in mobile water content and hydraulic conductivity in the overlying fluvial-lacustrine – marginal marine sediments (Figure 37) are most likely to represent washout zones resulting from the drilling process.

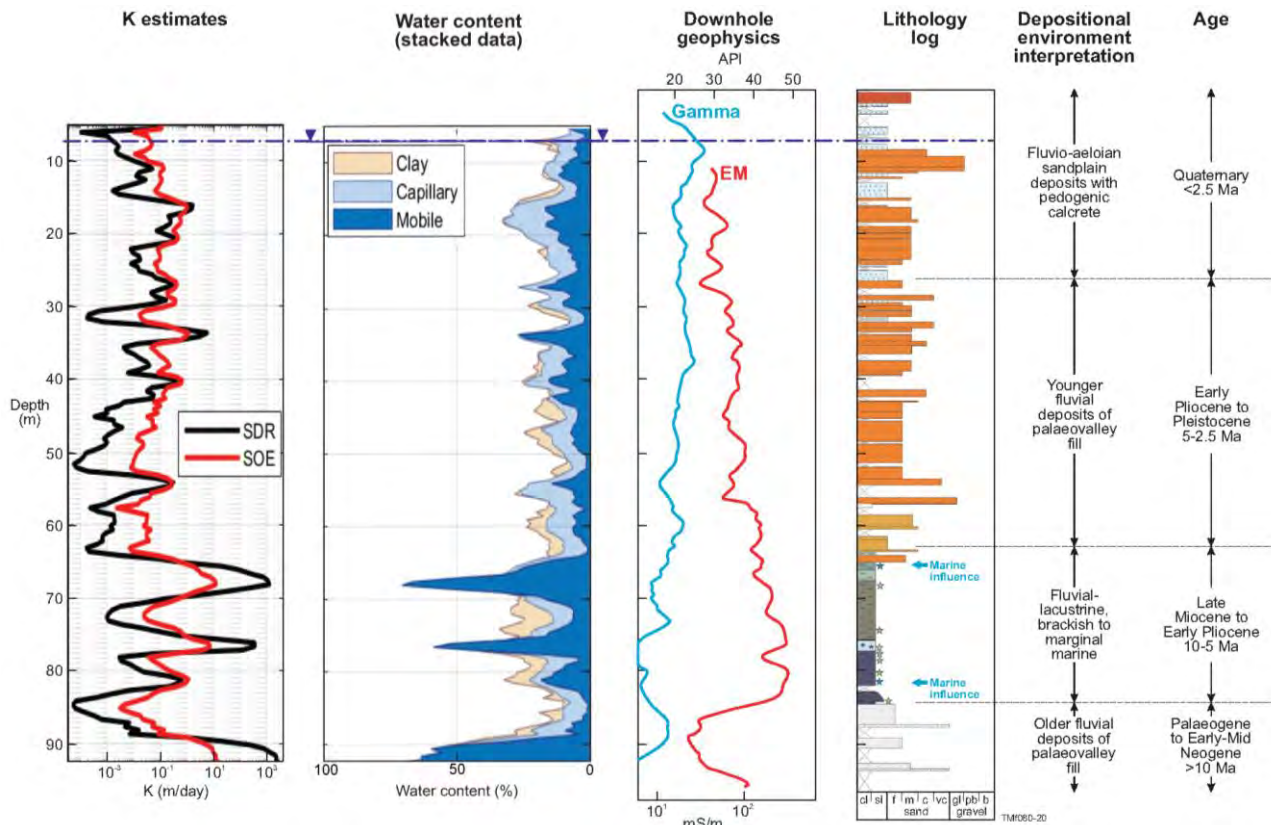


Figure 37. Lithology log of borehole DH1a with accompanying nuclear magnetic resonance, inductive conductivity and gamma logs. Lithology interpretation from Krapp et al. (2019).

The “target aquifer” layers, described by Keppel et al. (2019), were determined from mud rotary drilling and based on air development (which can be subjective), consist of a zone of interlayered calcareous sandstone and claystone between 60 and 65 m overlying a lacustrine claystone and mudstone. BNMR logs for DH1a and DH1a2 (Figure 37 and Figure 31 respectively), indicate that this zone has porosities of the order of 10-20%, with moderate mobile water contents (5-10%), the magnitude of these variations is similar to that encountered in higher parts of the sedimentary package. Whether that indicates that the productive aquifer layers are due to high yielding, but narrow units, remains uncertain and undefined. What is also unclear is whether some of the variations observed are a result of a variable mud invasion into the sidewall during drilling. A more accurate test of the method might be to employ sonic drilling approaches (Ruda and Farrar, 2006). This drilling method has been employed successfully in unconsolidated settings in Australia (see, for example, Lawrie et al. (2012)). The sonic drilling method applies high-frequency sound waves instead of a drill bit enabling penetration to depths of up to 250 m. The method yields high quality core samples in unconsolidated media.

One of the only holes that encountered saprolite, which was also logged with the BNMR was DH1f (Figure 35). The BNMR results show a marked transition between the overlying transported regolith and the *in situ*

saprolite. Overall porosity increases to be in excess of 20%, with much of that comprising capillary water. Free water contents remain low. This is in keeping with similar observations made by Emerson et al. (2000, and 2001). They noted that in petrophysical studies of regolith materials saprolites were characterised by very high porosities.

Results from bore S22i (Figure 36) contrasted with those drilled in the Lindsay East Palaeovalley. This bore, which targeted a tributary to the main palaeovalley (Figure 1) on a topographically elevated palaeo-interfluvial area overlies shallow basement. Free water contents in this bore are significantly lower than those observed for bores in the main palaeovalley although predicted porosities are of a similar order. The borehole inductive conductivity responses suggest a more resistive transported cover.

The borehole NMR tool provides a fine-scale indication of the vertical variations in the hydraulic characteristics of the aquifers logged. This is not unexpected in a sediment package comprising a mix of consolidated and unconsolidated materials. Calibration of the modelled hydraulic conductivity values would require detailed testing of the aquifer system with approaches such as multilevel slug tests (MLST) (see, for example, Butler (2005)), dipole-flow tests, and well bore flow (WBF) logging (see, for example, Dlubac et al. (2013); Parsekian et al. (2015); Knight et al. (2016); Maurer and Knight (2016); and more recently Kendrick et al. (2020). This was not possible as part of the G-Flows Stage-3 study.

Alternative approaches to testing finer scale variations in the hydraulic properties of the sediment types encountered in the Musgrave Province palaeovalleys might also include lab-based approaches. Dlubac et al. (2013), employed this through the lab-analysis of sidewall cores in the development of empirical constants that could be used to calibrate borehole NMR determined hydraulic conductivity models in near surface aquifer systems. However, that was not without challenges as the technique is both costly and requires specialised equipment. An interesting alternative, that warrants further investigation, is the use of fine scale studies involving the testing of drill core using transient-flow syringe air permeameters (see Brown and Smith 2013). Air permeameters have been used in a variety of laboratory and field applications where fine-scale measurements are needed to characterise the permeability heterogeneity of consolidated and unconsolidated materials (see, for example, Dreyer et al. (1990); Hartkamp et al. (1993); Tidwell & Wilson (1999); and Castle et al. (2004)).

In situ permeameters can reveal several orders of magnitude of permeability contrast missed by conventional core-plug measurements. Flinders University undertook some analysis of the DH1a Core using the TinyPerm (a device distributed by New England Research - <http://www.ner.com/site/systems/item/27-tinyperm.html>) and derived measurements of horizontal and vertical K in pieces of core sampled down the length of the bore. These results are plotted over the estimates of hydraulic conductivity from the BNMR in Figure 38. Estimates of horizontal K_h show a relatively good correlation with SOE estimates. Further work on the application of these analytical methods as a basis for calibrating BNMR measures is required.

Results from the BNMR were imaged against an AEM conductivity-depth section which traversed the Lindsay East Palaeovalley (Figure 39). The borehole lithology information (Keppel et al., 2019) provides spatial context for the hydraulic information to help support the AEM interpretation. The modelled water contents from the BNMR shown some correspondence with the conductivity structure in the AEM data. For example, the clayey fine to medium grained unconsolidated sand unit between 17 and 33 m (below the ground surface) identified in DH1a2 has a lower free water content (and lower porosity) than units above and below (Figure 31 and Figure 39). It coincides with a zone of elevated conductivity in the AEM data. Whether this relates to a slight increase in the solute content of the contained water is unknown but likely. At depth, the lacustrine-estuarine-marginal marine facies described by Krapf et al. (2019) have high porosities, less mobile water, but the BNMR data also indicate lower permeabilities (Figure 39). The AEM data show this zone to be relatively conductive.

Down-hole Nuclear Magnetic Resonance (NMR) has provided relative estimates of how available-water varies with depth as you get deeper in the palaeovalley (capillary and mobile), compared to clay water components in Figure 39. The shallower parts of the palaeovalley at DH1 appear to be more prospective for water, with lower groundwater salinity (see Figure 31 and Figure 35), and a static water level around 8 m below the land surface. Shallow wells (20-40 m) may provide an alternative target aquifer in this area, as opposed to targeting deeper parts if the aquifer system (55-65 m or 80-100 m). An option for pumping

smaller amounts from multiple shallow bores could be a strategy for consideration when using this resource. Bores of this depth are already employed for town water supply (see for example Dodds and Sampson 2000). Further investigations linked this option may be warranted.

The north – south orientated AEM conductivity-depth section that transects bore S22i, north of Kaltjiti (Figure 1), shows that the interpreted tributary to the Lindsay East Palaeovalley as a trough of relatively conductive material (Figure 36). The drill hole lithology log provides some insight into the relationship between the observed conductivity structure and stratigraphy. The BNRM logs indicate relative low amounts of free water in the saturated zone compared with the main palaeovalley sampled to the east. However, what could be interpreted as a relatively high-yielding sandy unit is identified in the BNMR logs, coincident with lower conductivity (from the inductive conductivity log) between 30 and 35 m (Figure 32). Modelled hydraulic conductivities from the BNMR are low compared to the sediments of the main palaeovalley system.

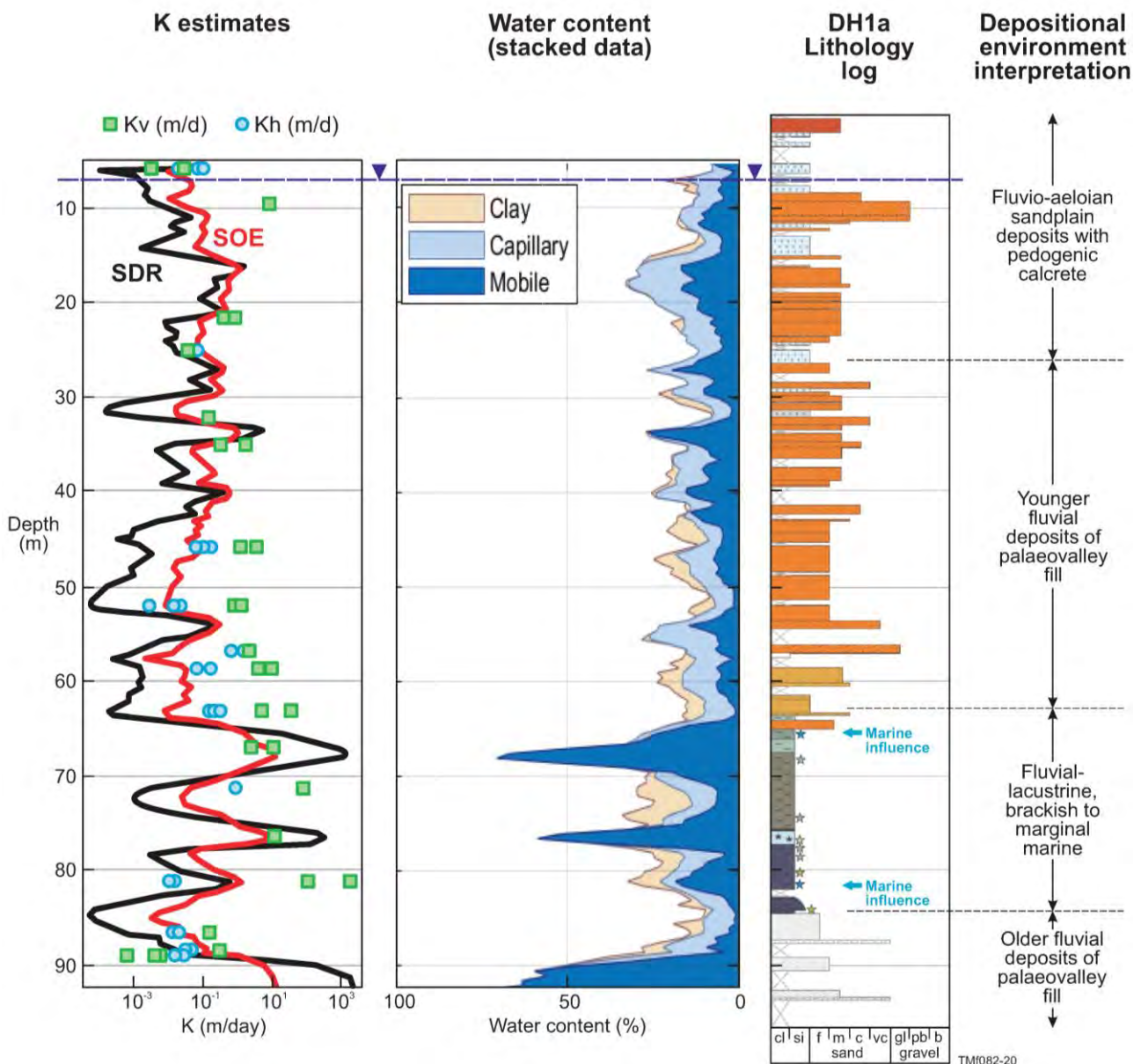


Figure 38. Comparison between fine scale TinyPerm derived measures of vertical and horizontal hydraulic conductivity (K_v and K_h) shown in the left-hand panel overlain on the borehole nuclear magnetic resonance modelled estimates of K using the Sum of Echoes (SOE) and Schlumberger-Doll Research (SDR) methods. TinyPerm results courtesy of Andy Love (Flinders University of South Australia).

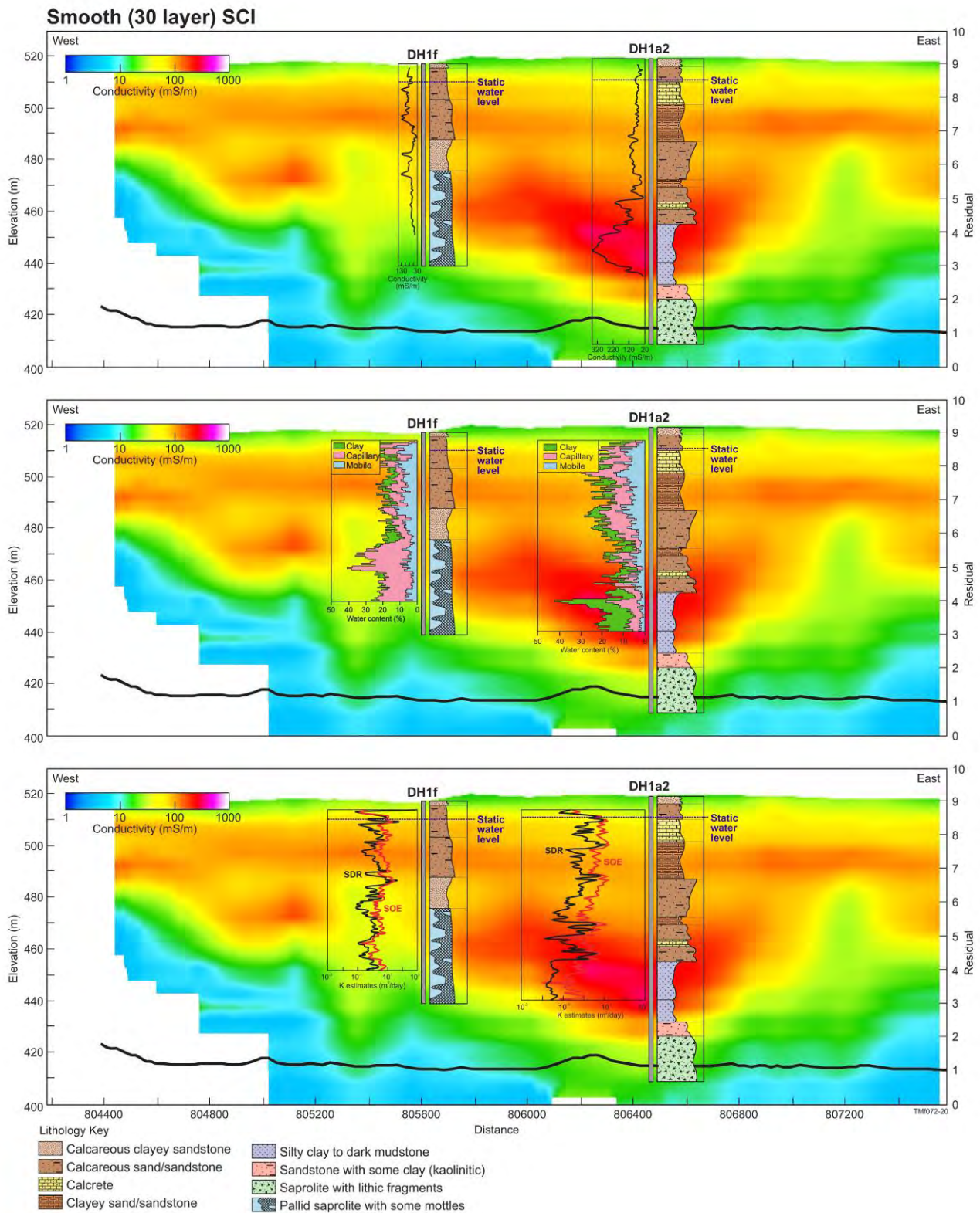


Figure 39. The Conductivity-depth sections for the Lindsay East Palaeovalley transect for a smooth 30-layer inversion. Drill hole lithology (adapted from Keppel et al. (2019)) and inductive conductivity logs are overlain on the AEM section in the top panel. Water contents from the borehole nuclear magnetic resonance are overlain on the section in the middle panel and modelled hydraulic conductivity estimates (Schlumberger Doll Research (SDR) and Sum of Echoes (SOE)) are overlain on the section in the lower panel. Adjustments to the predicted lithology textures (whether fining or coarsening upwards) have been made based on the borehole nuclear magnetic resonance logs.

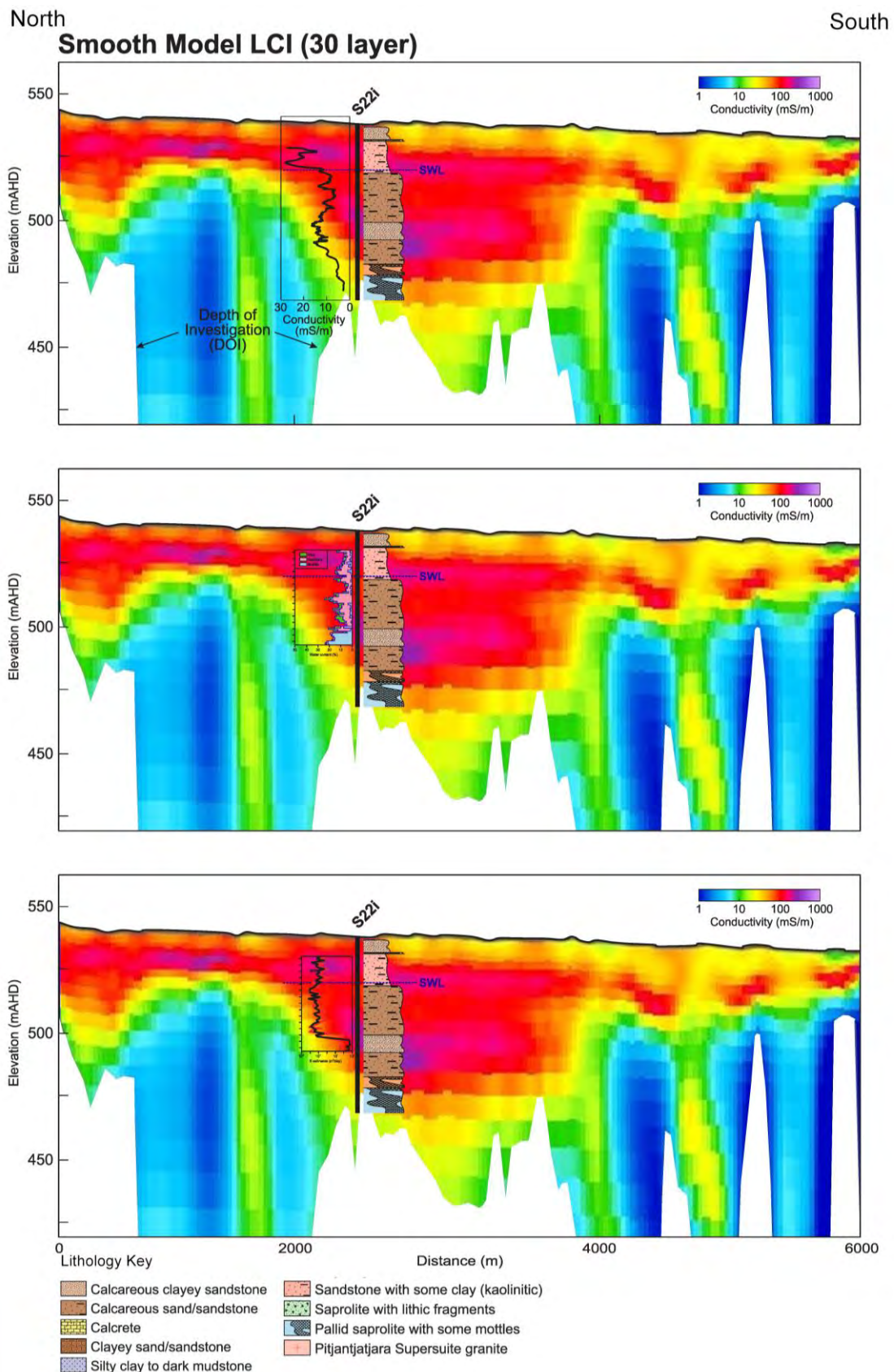


Figure 40. The Conductivity-depth section for airborne electromagnetic line adjacent to bore s22i. The airborne electromagnetic model is a smooth 30-layer inversion. Drill hole lithology (adapted from Keppel et al. (2019)) and inductive conductivity log is overlain on the airborne electromagnetic section in the top panel. Water contents from the borehole nuclear magnetic resonance are overlain on the section in the middle panel and modelled hydraulic conductivity estimates (Schlumberger Doll Research (SDR) and Sum of Echoes (SOE)) are overlain on the section in the lower panel.

6 Time domain electromagnetics (TDEM)

Ground time domain electromagnetics (TDEM) methods have a long-standing application in near surface geophysical investigations of groundwater resources.

6.1 The ground time domain electromagnetic (TDEM) method

The principle of the time domain electromagnetic approach is summarised in Figure 41. An ungrounded loop of electrical wire is placed on the ground and a time-varying current is transmitted through it using a specialised transmitter. A magnetic field is induced (referred to as the primary magnetic field) in the ground while current is being transmitted. When the current is turned off abruptly, the magnetic field is then left without its source and responds by inducing an image of the source loop in the subsurface. Initially this is equal to the primary magnetic field but is rapidly weakened by the electrical resistivity of the ground and it dissipates or decays. The induced current moves in circular horizontal paths and generates another magnetic field (the secondary field).

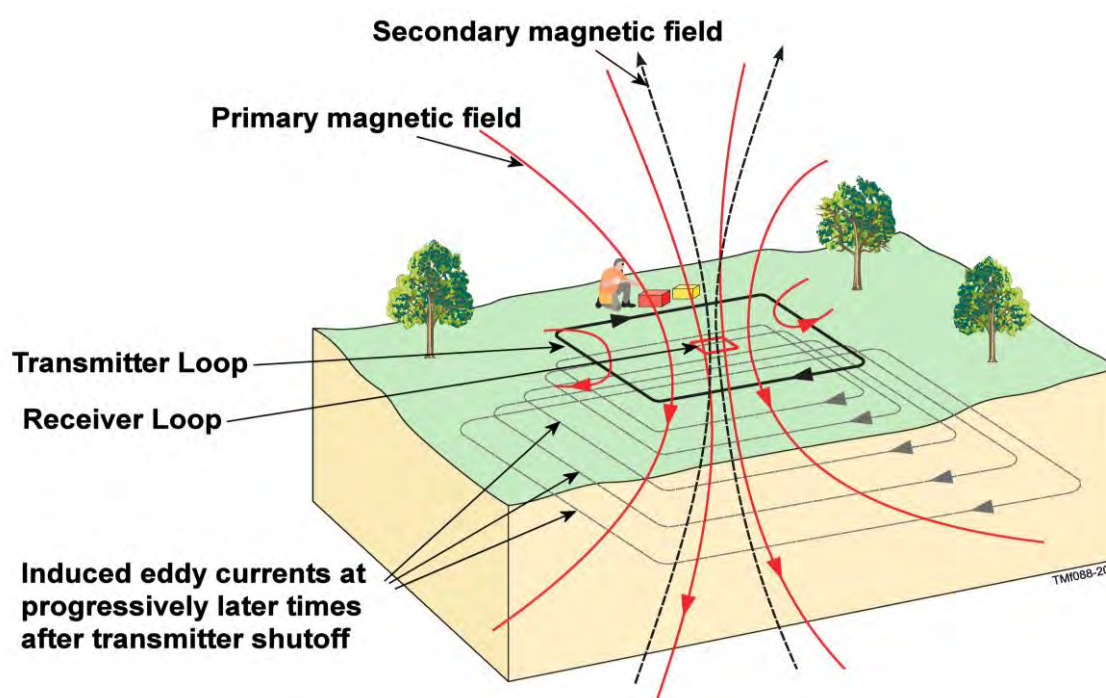


Figure 41. The principles of a time domain electromagnetic sounding.

The decaying secondary magnetic field is measured by the receiver coil (positioned in the centre of the transmitter loop, see Figure 41). Whilst dissipating, the current diffuses downwards and outwards, occupying an increasing volume of the subsurface (Figure 41). Shortly after turnoff, the current is concentrated in the near-surface and therefore the measured signal will reflect conductivities of near surface layers. With later times the current propagates deeper into the ground and the measured signal will contain information of the conductivity of these deeper layers.

The diffusion is initially quick, but it slows up with time. Diffusion is slower for conductive ground, and faster for resistive ground settings. Diffusion speed is proportional to $1/\sqrt{\sigma t}$, where t is the time after turnoff and σ is the ground conductivity. The recorded dataset (the decaying secondary magnetic field) is organised in time-windows, which are typically logarithmically increasing to improve the signal to noise ratio at later times, where the signal can be weak. The shape of the decaying signal recorded by the receiver coil provides information about the vertical conductivity structure of the subsurface.

6.2 Time domain electromagnetic (TDEM) workflow

The workflow employed in this pilot study is summarised in Figure 42 and involves the targeted acquisition, processing and inversion of ground-based time domain electromagnetic data, followed by their processing, inversion and subsequent interpretation against available hydrogeological information. In this study the interpretation also involved their forward modelling to provide some guidance as to how an airborne time domain EM system would perform in this environment.

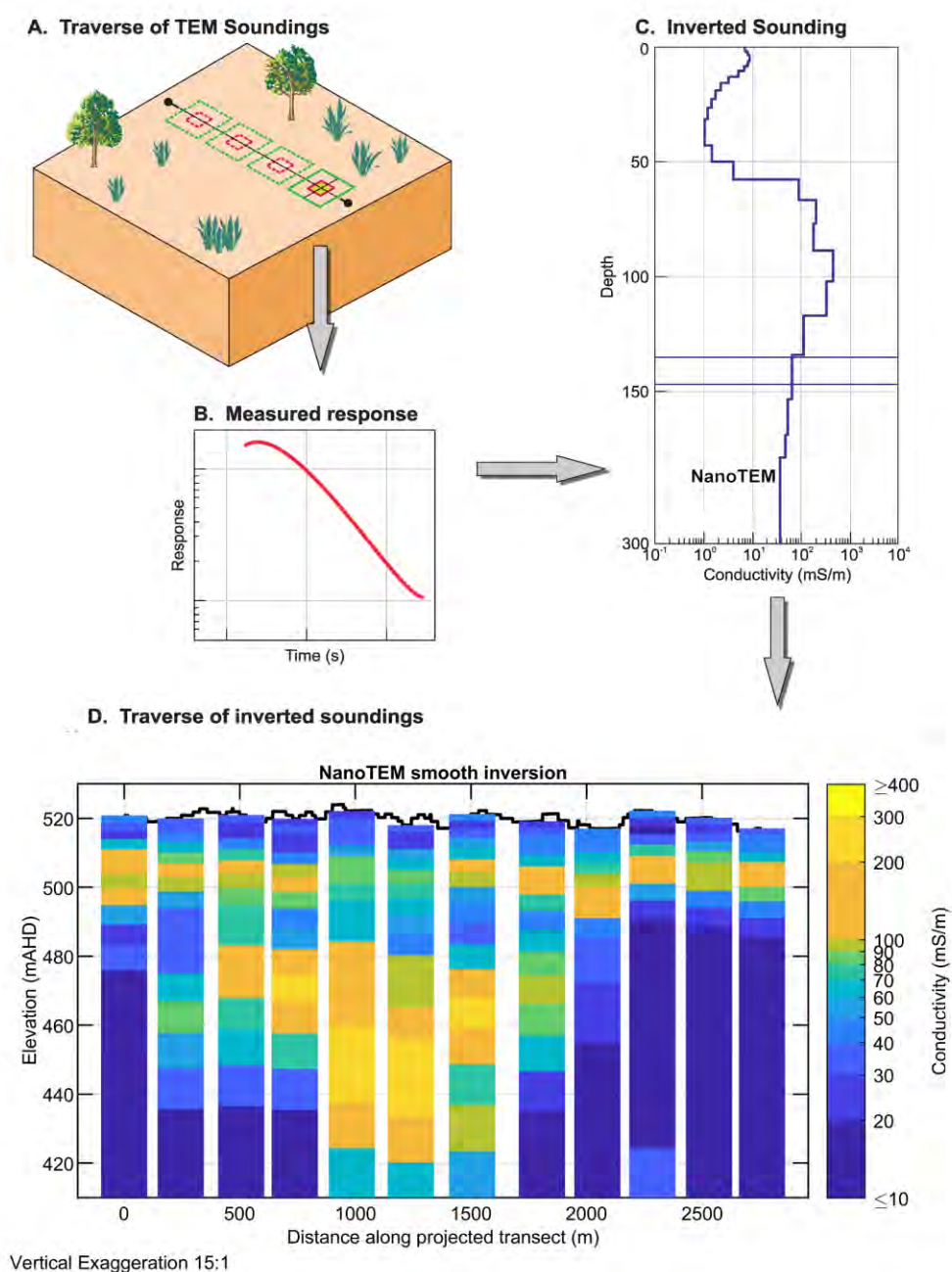


Figure 42. Schematic representation of the time domain electromagnetic (TDEM) acquisition (A), measurement (B), inversion (C) workflow, with section/traverse of pseudocoloured soundings to aid interpretation (D).

6.3 Field data acquisition

TDEM data were collected over the study area using a Zonge NanoTEM ground TDEM system (Zonge International, 2011a). The setup employed on this project consisted of a 40x40 m transmitter and standard centre-positioned receiver loop (Figure 43). Station soundings were completed with a spacing of approximately 250 m (Figure 43, Table 4).

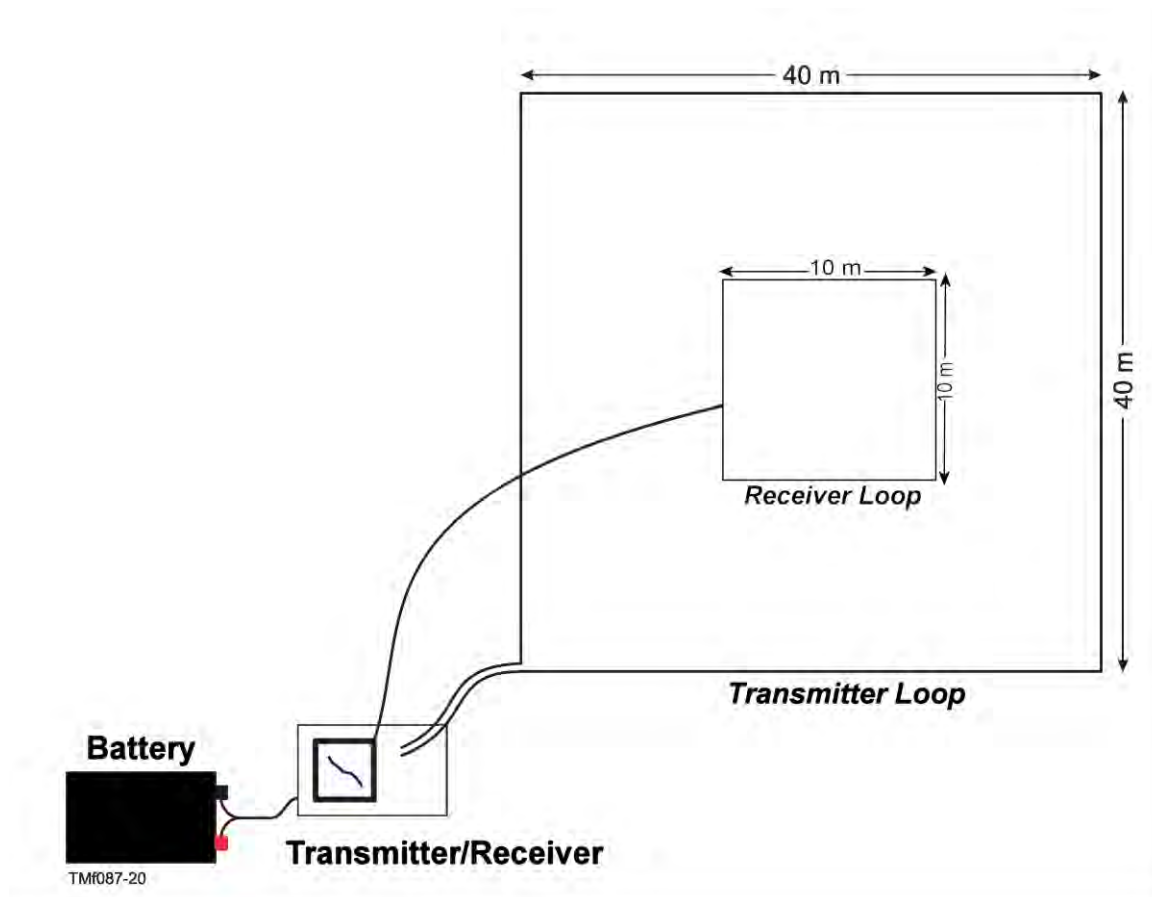


Figure 43. Layout of transmitter/receiver loops used in this study.

The NanoTEM operates with a NanoTEM card placed in the GDP-32II receiver. It transmits a 50% duty-cycle square wave 1 A pulse into a 40x40 m loop and receives in a 10x10 m concentric square receiver loop linked in opposite polarity to the transmit pulse. Earliest time windows for the NanoTEM system are about 3 μ s after transmitter shut-off, with data recording to ~800 ms for each cycle repetition. Data was recorded over about 27 windows, although this was changed during the processing stage to eliminate noisy windows from the data. Transmit frequency was set to 32 Hz, with 512 stacks per sounding, repeated five times per site. Details of the receiver sampling are shown in Table 5. The transmitter waveform is approximately trapezoidal with a peak current of 3 A, shown in Figure 44 (Zonge International, 2011b).

All data were inverted using smooth and blocky models. We also used both 13-layer unconstrained and 19-layer constrained models. Depth of inversion for the 19-layer models was limited to 100 m. Layer thicknesses and depth used in the TEM inversions are shown in Table 6. A total number of twelve soundings were acquired along the same transect as the seismic data acquisition program discussed in Section 4. This transect runs near-perpendicular to the orientation of the Lindsay East Palaeovalley along which the G-Flows Stage-3 drilling was undertaken (Figure 45). The location of the soundings relative to the drill holes in the Lindsay East Palaeovalley is shown in the inset box of Figure 45.

Table 4: Locations of ground-based NanoTEM time-domain electromagnetic soundings.

STATION	EASTING (m)	NORTHING (m)
0000	208806.80	7033117.14
0250	209044.43	7033058.29
0500	209297.00	7032990.25
0750	209522.73	7032937.89
1000	209762.36	7032878.74
1250	210011.34	7032823.36
1500	210268.49	7032759.17
1750	210514.55	7032583.83
2000	210694.33	7032425.37
2250	210883.25	7032280.65
2500	211073.09	7032125.75
2750	211243.77	7031973.18

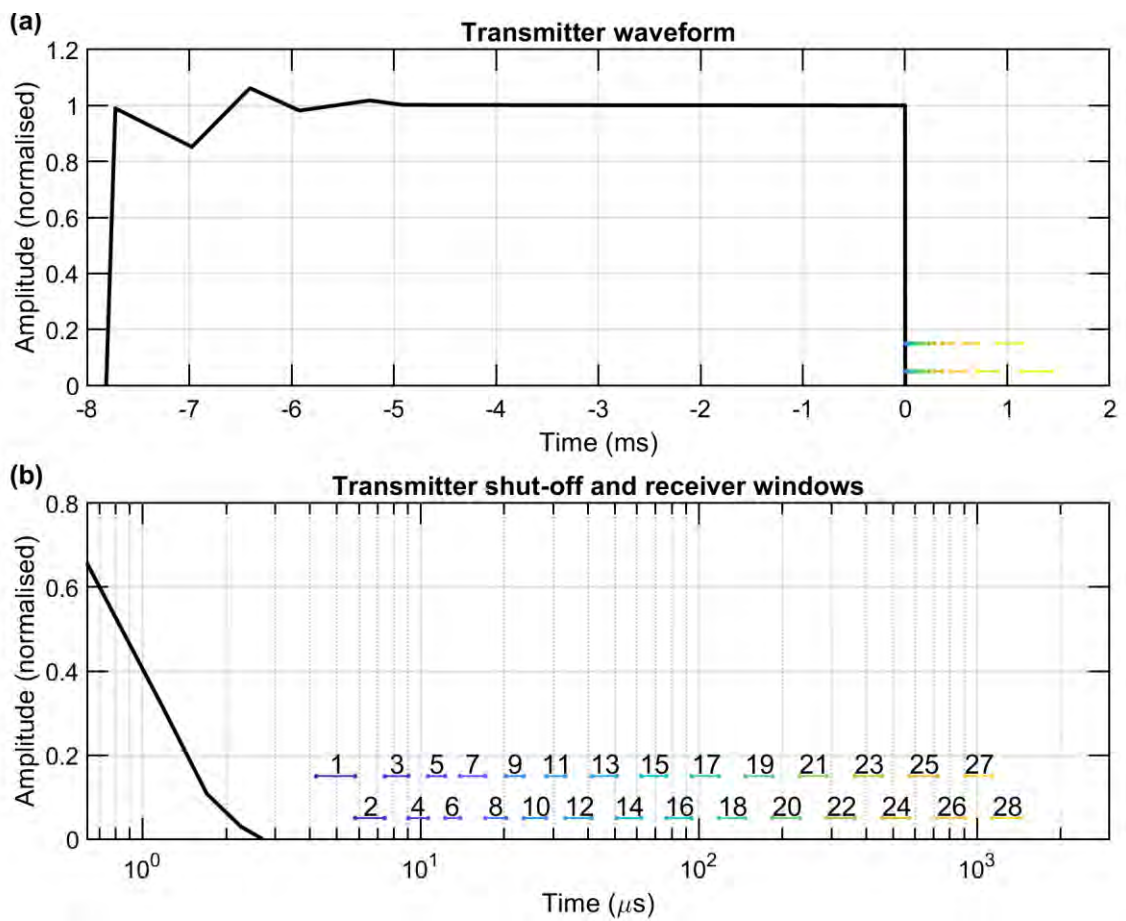


Figure 44. Transmitter current waveform (a) and receiver windows (b) of the NanoTEM electromagnetic system.

Table 5: Window start, end, and centre times for the NanoTEM time-domain electromagnetic system.

SAMPLE	RECEIVER START (s)	RECEIVER END (s)	RECEIVER CENTRE (s)
1	4.22E-06	5.82E-06	5.02E-06
2	5.82E-06	7.43E-06	6.63E-06
3	7.43E-06	9.03E-06	8.23E-06
4	9.03E-06	1.06E-05	9.84E-06
5	1.06E-05	1.22E-05	1.14E-05
6	1.22E-05	1.39E-05	1.31E-05
7	1.39E-05	1.71E-05	1.55E-05
8	1.71E-05	2.03E-05	1.87E-05
9	2.03E-05	2.35E-05	2.19E-05
10	2.35E-05	2.83E-05	2.59E-05
11	2.83E-05	3.31E-05	3.07E-05
12	3.31E-05	4.12E-05	3.71E-05
13	4.12E-05	5.08E-05	4.60E-05
14	5.08E-05	6.20E-05	5.64E-05
15	6.20E-05	7.65E-05	6.93E-05
16	7.65E-05	9.42E-05	8.53E-05
17	9.42E-05	0.000118	0.000106
18	0.000118	0.000147	0.000133
19	0.000147	0.000184	0.000166
20	0.000184	0.000231	0.000207
21	0.000231	0.000289	0.00026
22	0.000289	0.000364	0.000326
23	0.000364	0.000457	0.000411
24	0.000457	0.000573	0.000515
25	0.000573	0.000721	0.000647
26	0.000721	0.000907	0.000814
27	0.000907	0.00114	0.001023
28	0.00114	0.001435	0.001288

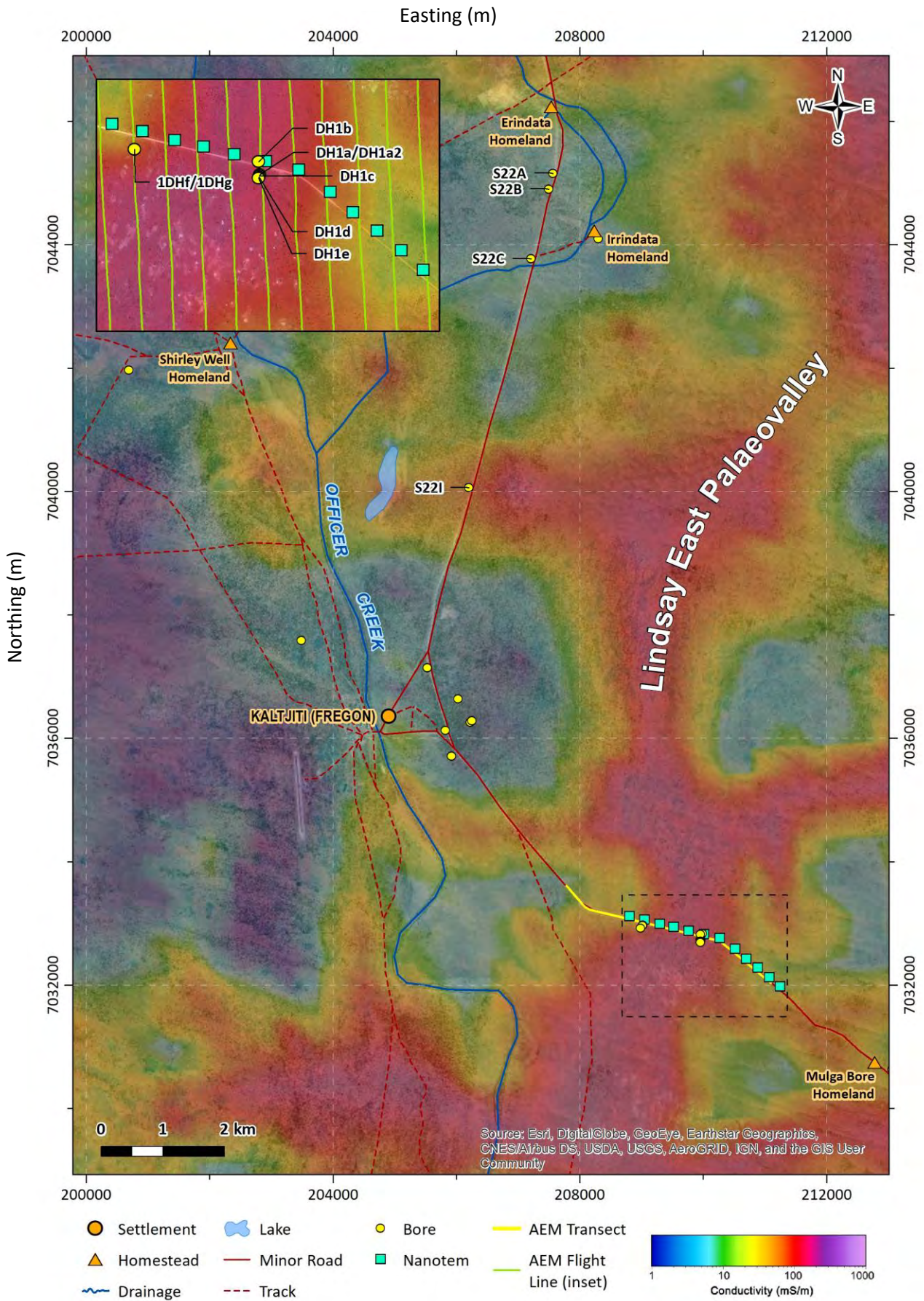


Figure 45. Location of NanoTEM survey soundings in the study area. Inset map shows their locations relative to the AEM flightlines.

6.4 Time domain electromagnetic inversion

Inversions for variation of conductivity with depth were conducted using a 1D layered-earth inversion (LEI) algorithm adopted from the AMIRA p223f suite on inversion programs (Raiche et al., 2007). Layer thickness was set prior to the inversion to best reflect the expected depth of investigation typically achieved with a NanoTEM system (~150 m in a resistive environment with a 40 m square loop and 3 A peak current). Conductivity values across each layer were constrained to vary by no more than 2x between layers (0.3 in logarithm base 10). Several inversion approaches were trialed including a blocky (few-layer) and smooth model. Results from the inversion of each sounding plotted along the transect shown in Figure 43 is shown in Figure 46 for the blocky LEI, and Figure 48 for the 19-layer smooth model LEI. Layer thicknesses for the smooth-model inversion are given in Table 6.

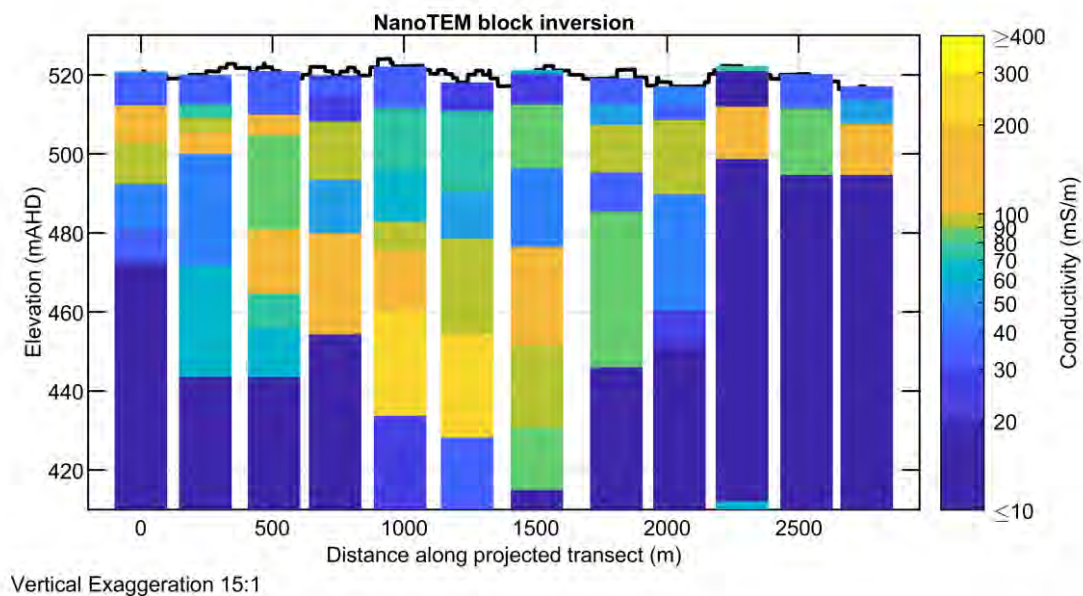


Figure 46. Conductivity-depth model for blocky layered inversion approach.

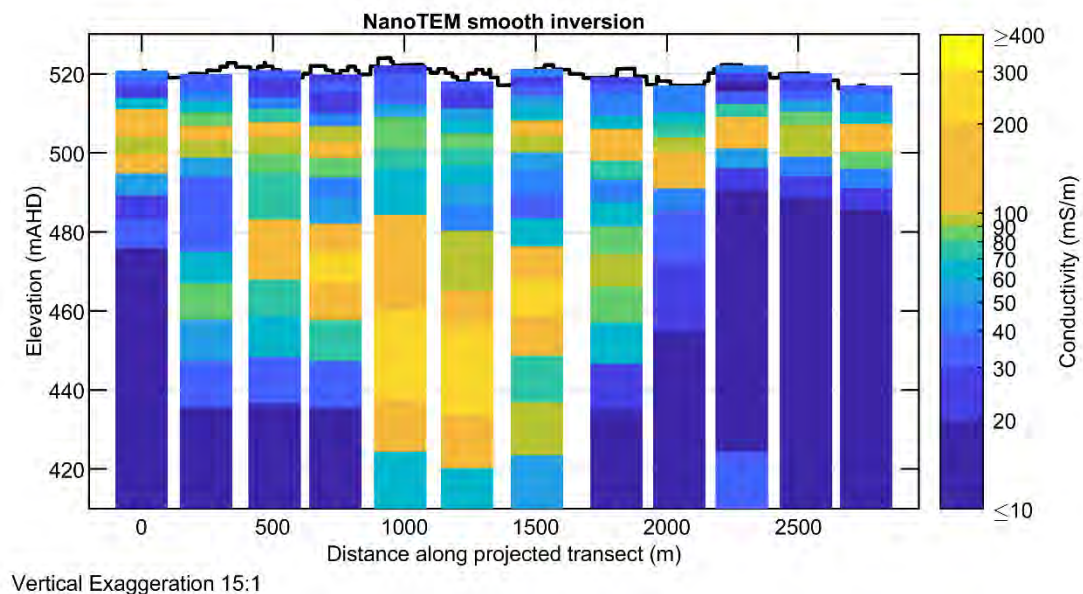


Figure 47. Conductivity-depth models resulting from smoothly constrained 19-layer 1D inversion.

Table 6: Layer thicknesses and depths used in 19-layer smooth-model inversions.

LAYER	DEPTH FROM (m)	DEPTH TO (m)	THICKNESS (m)
1	0	2	2.270635
2	4.270635	4.270635	2.577891
3	6.848526	6.848526	2.926724
4	9.77525	9.77525	3.322761
5	13.09801	13.09801	3.772388
6	16.8704	16.8704	4.282857
7	21.15326	21.15326	4.862402
8	26.01566	26.01566	5.52037
9	31.53603	31.53603	6.267371
10	37.8034	37.8034	7.115455
11	44.91885	44.91885	8.0783
12	52.99715	52.99715	9.171434
13	62.16859	62.16859	10.41249
14	72.58108	72.58108	11.82148
15	84.40255	84.40255	13.42113
16	97.82368	97.82368	15.23724
17	113.0609	113.0609	17.2991
18	130.36	130.36	19.63997
19	150	infinite	infinite

6.5 Time domain electromagnetic interpretation

Conductivity-depth models from the TDEM soundings are comparable with those generated from the AEM data, and an interpretation of the observed conductivity structure is similar to that obtained from the AEM data transect (Figure 48). The saturated zone appears to be coincident with a marked increase in ground conductivity which may relate to the concentration of salts through evapotranspiration at the interface between the saturated and vadose zones. A more resistive unit, possibly related to lower salinity groundwater, is encountered at about 30 m below the ground surface. The deeper parts of the palaeovalley are more conductive, and this is partially coincident with the presence of muds and clays associated with fluvial-lacustrine and marginal marine sediments as reported in Krapf et al. (2019).

Perhaps the biggest difference between the ground and airborne electromagnetic data sets is observed in the eastern part of the transect where the ground TDEM data suggests the presence of a more resistive unit (saprock/bedrock) nearer surface. This is reflected in the revised interpreted geological section (determined from a combination of drilling and the ground EM data) shown in Figure 48.

Further work on ground TDEM methods is planned, including the acquisition of data from different TDEM systems, and interpretation of the derived data using alternative inversion approaches.

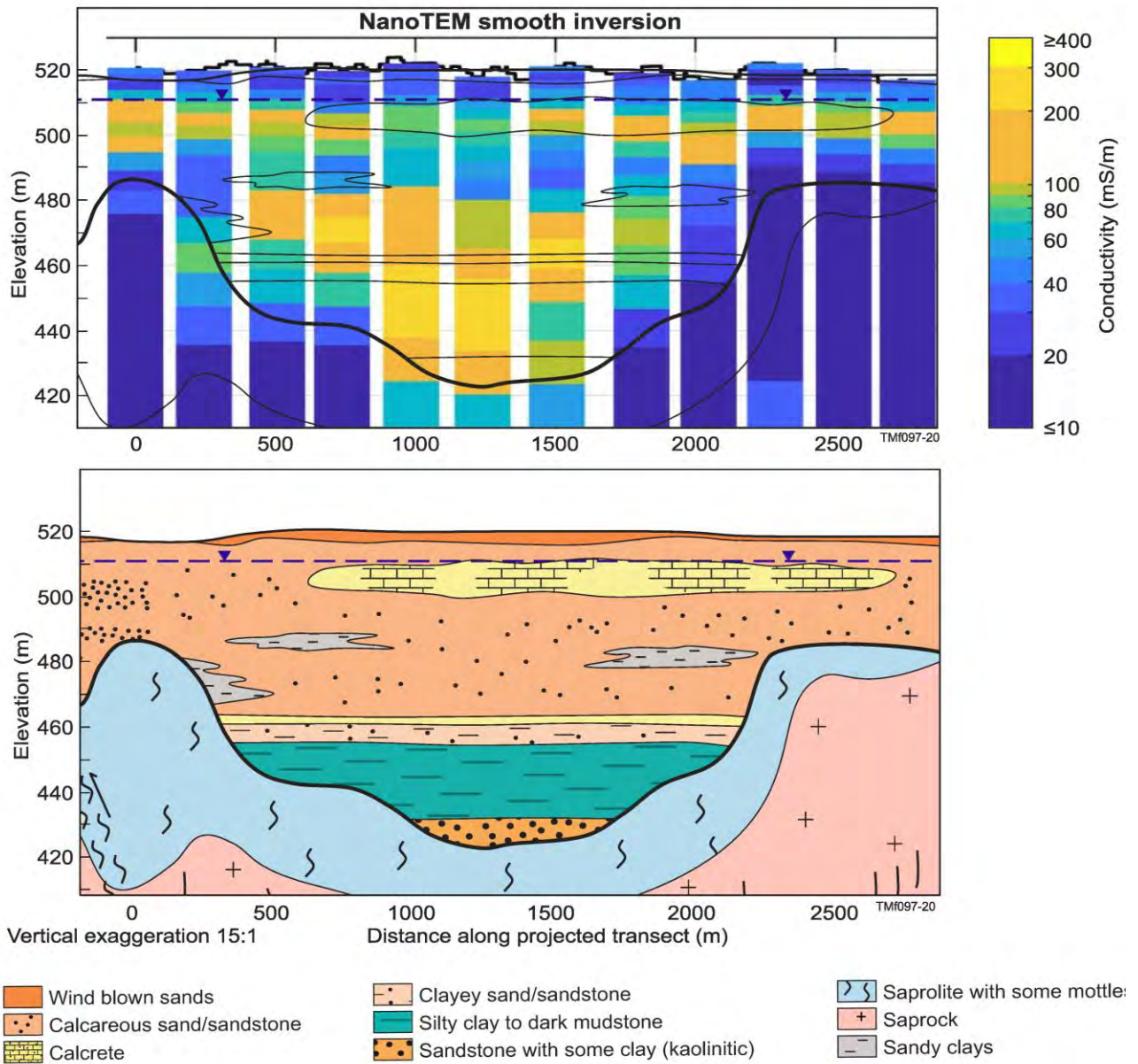


Figure 48. Smooth-model conductivity depth section from the inverted NanoTEM soundings (top panel) and the interpreted geology for the transect (lower panel). The geological section was determined from the combined interpretation of the drillhole and the conductivity section data. Geological linework is superimposed on the conductivity-depth soundings for added clarity.

7 Discussion and conclusions

This report summarises results from a selection of ground geophysical methods that can provide useful hydrogeological information in remote parts of South Australia. The work builds on previous studies undertaken in the region, principally with TDEM methods, but employs several relatively new technologies (e.g. the borehole NMR). With respect to the interpretation of TDEM data, newer, more robust and flexible inversion routines provide additional insight into the potential of that technology.

The advent of regional coverages of airborne geophysical data, particularly airborne electromagnetics, coupled with targeted drilling to investigate the sedimentary infilling of identified palaeovalley systems provides additional constraint to better understand the potential of hydrogeophysical approaches as a complementary technology to more conventional hydrogeological investigation methods.

The shallow seismic study, involving seismic reflection and refraction, was undertaken to obtain an independent measurement of the location of bedrock to help validate the airborne and ground TDEM data acquired in the study area. It was used to help elucidate details about the fill within the Lindsay East Palaeovalley. The seismic refraction results show significant variation in the near surface (top 10 m) velocity structure and a deep (~100 m) refractor that is believed to be the top of bedrock. The seismic reflection results show significant variability, both lateral and vertical, in the top of bedrock reflector and reveal prominent and clear reflections down to depths greater than 400 m. In contrast to the AEM data, the seismic data appear to define an interface between weathered and unweathered basement rocks at a depth significantly greater depth. The AEM data may not effectively resolve the boundary between the regolith and the basement in this situation, perhaps because we encounter a limit to its depth of investigation. Nonetheless the AEM data does appear to resolve the depth of the transported regolith, thereby defining the lower limits of the palaeovalley fill aquifer. The seismic data in contrast may define the boundary between the saprock and underlying bedrock. Given that the saprock, the overlying saprolite and the transported sediments above that represent the full aquifer (excluding the fractured rock component) this is also useful information to know.

While previous studies have demonstrated the potential for NMR logging data to provide reliable estimates of hydraulic conductivity (K) at high levels of vertical resolution, the opportunity remains to demonstrate this for the aquifer systems in the palaeovalleys of the APY Lands in the Musgrave Province. An added challenge is the definition of properties for both unconsolidated and consolidated materials found in the palaeovalley sedimentary sequences present. The BNMR results for the bores drilled into the Lindsay East main trunk valley indicate that the finer scale hydraulic properties of the palaeovalley sediments vary significantly vertically and laterally, reflecting the heterogeneity of the sediment package. Free water content in the upper part of the sedimentary sequence appears to be relatively consistent between bores but there is a suggestion that water contents may be slightly lower on the margins of the palaeovalley.

In the deeper part of the palaeovalley sequence, the presence of estuarine muds and clays have low K values, and this may act as a partially confining layer to the sandy unit aquifer below it, that sits above saprolite. The BNMR results don't necessarily support the observation that there is a higher yielding aquifer between 55-65 m in the centre of the palaeovalley, as has been suggested by Keppel et al. (2019) and Costar et al. (2019), but rather supports a model for higher yielding layer, which may be relatively thin (<5 m) within the overall sequence. Potentially there may be several such layers in that zone. Further work is required to test this. Modelled K values from the BNMR are consistent with those determined from aquifer testing, but more detailed testing employing multilevel slug tests (MLST), dipole-flow tests, and/or well bore flow (WBF) logging would be beneficial, and would provide a basis for deriving calibration values for the NMR data. This would then permit the spatial extension of BNMR logging to other parts of the region to derive more representative information on the hydraulic properties of the alluvial aquifer systems present. Other calibration approaches should also be examined including various lab-based methods employing the drill core collected. Further work is required to test this.

Results from the ground-based time domain electromagnetic (TDEM) methods show a similar conductivity structure for the transect across the Lindsay East Palaeovalley as was observed in the AEM data processed and inverted independently. Together they support the model for a deeper conductive zone within the

central part of the palaeovalley, including sediments comprising the confining mudstones and sandier units above that. The similar conductivity values of these different materials as observed in airborne, ground and borehole conductivity measurements indicate that groundwater salinity or quality is one of the key drivers of the observed conductivity structure.

The ground TDEM data suggest that a crude indication of the standing water level could be determined by mapping the depth to the top of the first conductive layer; interpreted as being related to a zone of higher salinity through evapotranspiration.

While this study has demonstrated the potential of different hydrogeophysical techniques to elucidate the hydrostratigraphy and nature of the groundwater present in the Lindsay East Palaeovalley system, the value of more systematic studies such as this will only be realised through further hydrological investigations of the aquifers, and through additional combined analysis of the geophysical data. For example, it is possible to constrain inversions of electromagnetic data with information provided by seismic data. Similarly, the joint inversion of borehole and surface EM data can also be undertaken. Potentially these approaches will yield more robust models for subsurface properties.

In summary, and as demonstrated in this initial phase of investigation, ground-based hydrogeophysical studies have the potential to provide an improved understanding of the palaeovalley systems in the Musgrave Province. If employed in conjunction with the analysis of the available airborne AEM data, and conventional hydrogeological investigations, they could assist in better defining drilling options across the region, detailing depth to basement, water quality, and information about the aquifers (sedimentary) themselves.

References

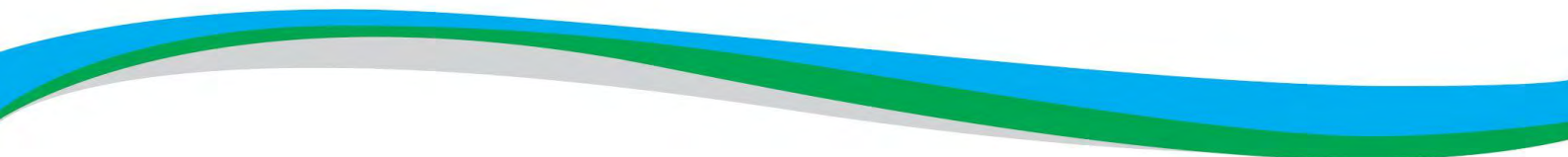
- Behroozmand AA, Keating K, and Auken E (2015). A review of the principles and applications of the NMR technique for near-surface characterization. *Surveys in Geophysics* 36(1): 27–85. <https://doi.org/10.1007/s10712-014-9304-0>
- Bureau of Meteorology (BOM) (2018). Climate statistics for Australian locations, Summary statistics ERNABELLA, Monthly mean maximum temperature. Bureau of Meteorology, viewed 5 June 2018, <http://www.bom.gov.au/climate/averages/tables/cw_016013.shtml>.
- Brown RJS and Gamson BW (1960). Nuclear magnetism logging. *Petroleum Trans., AIME* 219: 201–209.
- Brown S and Smith M (2013). A transient-flow syringe air permeameter. *Geophysics* 78(5): D307–D313
- Butler JJ Jr. (2005). Hydrogeological methods for estimation of hydraulic conductivity. In *Hydrogeophysics*, ed. Y. Rubin and S. Hubbard, 23–58. The Netherlands: Springer.
- Castle JW, Molz FJ, Lu S, and Dinwiddie CL (2004) Sedimentology and Fractal-Based Analysis of Permeability Data, John Henry Member, Straight Cliffs Formation (Upper Cretaceous), Utah, U.S.A.. *Journal of Sedimentary Research* 74 (2): 270–284.
- Clarke DK (2000). Indulkana town water supply drilling and discharge testing, 1998. South Australia, Department of Primary Industries and Resources, Report Book, RB 2000/06.
- Coates GR, Miller M, Gillen M, and Henderson C (1991). The MRIL In Conoco 33-1 An Investigation Of A New Magnetic Resonance Imaging Log. *Society of Petrophysicists and Well-Log Analysts (SPWLA) 32nd Annual Logging Symposium*, 16-19 June, Midland, Texas.
- Coates GR, Xiao L, and Prammer MG (1999). *NMR Logging Principles and Applications*. Halliburton Energy Services, Houston.
- Coats RP (1962). The geology of the Alberga 4-Mile Military Sheet, Report of Investigations 22. Geological Survey of South Australia, Adelaide.
- Conor CHH (2004). The geology of the Eateringinna 1:100 000 sheet area, eastern Musgrave Block, South Australia, Report Book 2003/00016. Primary Industry and Resources South Australia, Adelaide.
- Costar A, Howles S, and Love A (in press). G-FLOWS Stage 3, APY Lands Aquifer Testing, north-western South Australia, Technical Report Series. Goyder Institute for Water Research, Adelaide
- Costar A, Love A, Krapf C, Keppel M, Munday T, Inverarity K, Wallis I, and Soerensen C (2019). Hidden water in remote areas – using innovative exploration to uncover the past in the Anangu Pitjantjatjara Yankunytjatjara Lands. *MESA Journal* 90: 23–35.
- Cowan B (1997). *Nuclear Magnetic Resonance and Relaxation*. Cambridge University Press, UK.
- Dijkstra EW (1959). A Note on Two Problems in Connexion with Graphs. *Numerische Mathematik* 1: 269–271.
- Dlubac K, Knight R, Song YQ, Bachman N, Grau B, Cannia J, and Williams J. (2013). Use of NMR logging to obtain estimates of hydraulic conductivity in the High Plains aquifer, Nebraska, USA. *Water Resources Research*, 49(4), 1871–1886. <https://doi.org/10.1002/wrcr.20151>
- Dodds AR (1996). Report on a groundwater search program over various Pitjantjatjara Homelands in the Musgrave Ranges area, South Australia. South Australia, Department of Mines, Report Book RB 96/37.
- Dodds AR (1997). An assessment of the groundwater resources of the Lake Maurice area, northwest South Australia, for the Oak Valley community, Maralinga Tjarutja Aboriginal Lands. Mines and Energy Resources, South Australia Report 97/56.
- Dodds AR and Sampson L (2000). The sustainability of Water resources in the Anangu Pitjantjatjara Lands, South Australia PIRSA RB 2000/00027, 132

- Dreyer T, Scheie Å, and Walderhaug O (1990). Minipermeameter-Based Study of Permeability Trends in Channel Sand Bodies. *AAPG Bulletin* 74 (4): 359–374.
- Dunn K-J, Bergman DJ, and Latorraca GA (2002). Nuclear Magnetic Resonance Petrophysical and Logging Applications. Oxford, United Kingdom: Elsevier Science.
- Edgoose CJ, Scrimgeour IR and Close DF (2004). Geology of the Musgrave Block, Northern Territory, Report 15. Northern Territory Geological Survey, Darwin.
- Emerson D, Macnae J, and Sattel, D (2000). Physical properties of the regolith in the Lawlers area, Western Australia, *Exploration Geophysics*, 31:1-2, 229-235, DOI: 10.1071/EG00229
- Emerson D and Macnae J (2001). Further Physical Property Data from the Archaean Regolith, Western Australia. Preview Number 92, Preview, 2001:92, 33-41, DOI: 10.1071/PVv2001n92
- Gallardo LA and Meju MA (2003). Characterization of heterogeneous near-surface materials by joint 2D inversion of dc resistivity and seismic data. *Geophys. Res. Lett.* 30(13): 1658, doi:10.1029/2003GL017370
- Gallegos DP and Smith DM (1988). A NMR technique for the analysis of pore structure: Determination of continuous pore distributions. *Journal of Colloid and Interface Science* 122: 143–153.
- Glikson AY, Stewart AJ, Ballhaus CG, Clarke GL, Feeken EHJ, Leven JH, Sheraton JW, and Sun S-s (1996). Geology of the western Musgrave Block, Central Australia, with particular reference to the maficultramafic Giles Complex, Bulletin 239. Australian Geological Survey Organisation, Canberra.
- Goodwin JA, Jiang W, Meixner AJ, McAlpine SRB, Buckerfield S, Nicoll MG, and Crowe M (2017). Estimating cover thickness in the Southern Thomson Orogen: results from the pre-drilling application of refraction seismic, audio-magnetotelluric and targeted magnetic inversion modelling methods on proposed borehole sites. Record 2017/21. Geoscience Australia, Canberra. <http://dx.doi.org/10.11636/Record.2017.021>
- Hand M and Sandiford M (1999). Intraplate deformation in Central Australia, the link between subsidence and fault reactivation. *Tectonophysics* 305:121–140.
- Hartkamp CA, Arribas J, and Tortosa A (1993). Grain size, composition, porosity and permeability contrasts within cross-bedded sandstones in Tertiary fluvial deposits, central Spain. *Sedimentology* 40(4): 787–799.
- Howard HM, Smithies RH, Evins PM, Kirkland CL, Werner M, Wingate MTD, and Pirajno F (2011). Explanatory notes for the west Musgrave Province, Record 2011/4. Geological Survey of Western Australia, Perth.
- Kendrick AK, Knight R, Johnson CD, Liu G, Knobbe S, Hunt RJ, and Butler JJ Jr. (2020). Assessment of NMR logging for estimating hydraulic conductivity in glacial aquifers. *Groundwater*. Accepted Author Manuscript. doi:[10.1111/gwat.13014](https://doi.org/10.1111/gwat.13014)
- Kenyon WE, Day PI, Straley C, and Willemsen JF (1988). A three-part study of NMR longitudinal relaxation properties of water-saturated sandstones. *Society of Petroleum Engineers Formation Evaluation* 3: 622–636.
- Keppel M, Costar A, Love A, and Krapf C (2019). G-FLOWS Stage 3 APY Lands Drilling Program, north-western South Australia. Technical Report Series 19/39. Goyder Institute for Water Research, Adelaide.
- Kirkland CM and Codd SL. (2018). Low-field borehole NMR applications in the near-surface environment. *Vadose Zone Journal*, 17(1), 1–11. <https://doi.org/10.2136/vzj2017.01.0007>
- Kleinberg RL (2001). NMR well logging at Schlumberger. *Concepts in Magnetic Resonance* 13: 396–403.
- Knight R, Walsh DO, Butler JJ, Grunewald E, Liu G, Parsekian AD, Reboulet EC, Knobbe S, and Barrows M (2016). NMR Logging to Estimate Hydraulic Conductivity in Unconsolidated Aquifers. *Groundwater* 54(1): 104–14. doi:10.1111/gwat.12324

- Kowalsky MB, Chen J, and Hubbard, SS (2006). Joint inversion of geophysical and hydrological data for improved subsurface characterization. *The Leading Edge* 25(6): 730
<http://dx.doi.org/10.1190/1.2210057>
- Krapf CBE, Irvine JA, and Cowley WM (2012). Compilation of the 1:2 000 000 State Regolith Map of South Australia – a summary. Report Book 2012/00016. Department for Manufacturing, Innovation, Trade, Resources and Energy, South Australia, Adelaide.
- Krapf CBE, Werner M, Dutch R, and Pawley M (2014). A guide to bedrock weathering profiles in the eastern Musgrave area. Unlocking SA's Mineral Wealth [Conference], and [follow-on] Technical Forum: presentation and poster abstracts, Report Book 2014/00004. Department for Manufacturing, Innovation, Trade, Resources and Energy, Adelaide, pp.59, 85.
- Krapf CBE, Werner M, Questiaux D, Spooner N, Williams F, and Dutch R (2018). Optically stimulated luminescence dating revealing new insights into the age of major regolith units of the eastern Musgrave Province, South Australia, Report Book 2018/00004. Department for Energy and Mining, South Australia, Adelaide.
- Krapf C, Costar A, Stoian L, Keppel M, Gordon G, Inverarity K, Love A, and Munday T (2019). A sniff of the ocean in the Miocene at the foothills of the Musgrave Ranges – unravelling the evolution of the Lindsay East Palaeovalley. *MESA Journal* 90: 4–22.
- Krejci M, Lett M, Lloyd A, Hopper T, Neville T, and Birt B (2018). Groundwater Assessment in a Coal Measures Sequence Using Borehole Magnetic Resonance. ASEG Extended Abstracts 2018, 1-5.
https://doi.org/10.1071/ASEG2018abT7_3H
- Kretschmer P and Wohling D (2014). Groundwater recharge in the Anangu Pitjantjatjara Yankunytjatjara Lands, South Australia, DEWNR Technical Report 2014/06, Government of South Australia, through the Department of Environment, Water and Natural Resources, Adelaide.
- Lawrie KC, Brodie RS, Tan KP, Gibson D, Magee J, Clarke JDA, Halas L, Gow L, Somerville P, Apps HE, Christensen NB, Brodie RC, Abraham J, Smith M, Page D, Dillon P, Vanderzalm J, Miotlinski K, Hostetler S, Davis A, Ley-Cooper AY, Schoning G, Barry K, and Levett K (2012). Broken Hill Managed Aquifer Recharge (BHMAR) Project: Securing Broken Hill's Water Supply: Assessment of Conjunctive Water Supply Options Involving Managed Aquifer Recharge and/or Groundwater Extraction at Menindee Lakes: Data acquisition, processing, analysis and interpretation method. Record 2012/011. Geoscience Australia, Canberra. <http://pid.geoscience.gov.au/dataset/ga/73819>
- Leaney FW, Taylor AR, Jolly ID, and Davies PJ (2013). Facilitating Long Term Out-Back Water Solutions (G-FLOWS) Task 6: Groundwater recharge characteristics across key priority areas, Goyder Institute for Water Research Technical Report Series No. 13/6, Adelaide, South Australia.
- Major RB and Connor CHH (1993). The Musgrave Block. In JF Drexel, WV Preiss and AJ Parker eds, The geology of South Australia, Volume 1, The Precambrian, Bulletin 54. Geological Survey of South Australia, Adelaide, pp. 156–167.
- Maurer J and Knight R (2016). Models and Methods for Predicting Hydraulic Conductivity in Near-Surface Unconsolidated Sediments Using Nuclear Magnetic Resonance. *Geophysics* 81(5):D503–18.
 doi:10.1190/geo2015-0515.1.
- Moser TJ (1991). Shortest path calculation of seismic rays. *Geophysics* 56: 9–159.
- Moser TJ, Nolet G, and Snieder R (1992). Ray vending revisited. *Bulletin of the Seismological Society of America* 82: 259–288.
- Nelson RG (1974). Geophysics in search of groundwater, Indulkana Aboriginal Reserve. Department of Mines, Report Book RB 74/93.
- Parsekian A, Grombacher D, Davis A, Flinchum B, Munday T, Cahill K (2014). Near-surface geophysics for informed water-management decisions in the Anangu Pitjantjatjara Yankunytjatjara (APY) lands of South Australia. *The Leading Edge* 33(12):1342-1347. <https://doi.org/10.1190/tle33121342.1>

- Parsekian AD, Dlubac K, Grunewald E, Butler JJ, Knight R and Walsh DO. (2015). Bootstrap calibration and uncertainty estimation of downhole NMR hydraulic conductivity estimates in an unconsolidated aquifer. *Groundwater*, 53(1), 111–121. <https://doi.org/10.1111/gwat.12165>
- Pawley MJ, Dutch RA, Werner M and Krapf CBE (2014). Repeated failure: long-lived faults in the eastern Musgrave Province. *MESA Journal* 75:45–55. Department of State Development, South Australia, Adelaide.
- Quentin de Gromard R, Howard HM, Smithies RH, Wingate MTD, and Lu Y (2017). The deep seismic reflection profile 11GA-YO1 in the west Musgrave Province: an updated view, Record 2017/8. Geological Survey of Western Australia, Perth.
- Raiche A, Sugeng F, and Wilson G (2007). Practical 3D EM inversion ? the P223F software suite. *ASEG Extended Abstracts 2007(1)* 1–5.
- Rogers PA (1995). Hamilton Basin. In JF Drexel and WV Preiss eds, *The geology of South Australia, Volume 2, The Phanerozoic*, Bulletin 54. Geological Survey of South Australia, Adelaide, p. 198.
- Rücker C, Günther T, and Wagner F (2017). pyGIMLi: An open-source library for modelling and inversion in geophysics. *Computers & Geosciences* 109: 106–123.
- Ruda T and Farrar J (2006). Environmental drilling for soil sampling, rock coring, borehole logging, and monitoring well installation. In Nielsen DM (ed.) *Practical handbook of environmental site characterization and ground water monitoring*. CRC Taylor & Francis, Boca Raton, pp 297–344.
- Seevers DO (1966). A Nuclear Magnetic Method For Determining The Permeability Of Sandstones. Society of Petrophysicists and Well-Log Analysts (SWLA) 7th Annual Logging Symposium, 9-11 May, Tulsa, Oklahoma.
- Soerensen CC, Munday TJ, Ibrahim T, Cahill K and Gilfedder M (2018). Musgrave Province, South Australia: Processing and inversion of airborne electromagnetic (AEM) data: preliminary results, Technical Report Series 18/06. Goyder Institute for Water Research, Adelaide.
- Stapf S and Han S-I (eds) (2006). *NMR Imaging in Chemical Engineering*, Wiley-VCH, Weinheim.
- Tewkesbury PS and Dodds AR (1996). Oak Valley groundwater investigation. Department of Mines and Energy South Australia.
- Tewkesbury P and Dodds AR (1997). *An appraisal of the water resources of the Musgrave Block, South Australia*, Department of Mines and Energy Resources, Geological Survey of South Australia, Report book 97/22, DME 93/526
- Tiab D and Donaldson EC (2012). *Petrophysics: Theory and Practice of Measuring Reservoir Rock and Fluid Transport Properties*. Third Edition. Elsevier.
- Tidwell VC and Wilson JL (1999). Upscaling experiments conducted on a block of volcanic tuff: Results for a bimodal permeability distribution. *Water Resources Research* 35(11):3375–3387.
- Timur A (1969). Pulsed nuclear magnetic resonance studies of porosity, movable fluid, and permeability of sandstone. *Journal of Petroleum Technology* 21: 755–786.
- Trofimczyk K, Downey M, Hopper T, Neville T, and Birt B (2018). Continuous Hydrogeological Characterisation in Iron Ore Deposits Using Borehole Magnetic Resonance. *ASEG Extended Abstracts 2018*, 1-6. <https://doi.org/10.1071/ASEG2018abP084>
- Vilhelmsen TN, Behroozmand AA, Christensen S, and Nielsen TH (2014). Joint inversion of aquifer test, MRS, and TEM data. *Water Resources Research* 50: 3956–3975. <https://doi.org/10.1002/2013WR014679>
- Walsh D (2008). Multi-channel surface NMR instrumentation and software for 1D/2D groundwater investigations. *Journal of Applied Geophysics* 66: 140–150.
- Walsh D, Grunewald E, Turner P, and Frid I (2010). Javelin: A slimhole and microhole NMR logging tool. *Fast Times* 15(3): 67–72.

- Walsh D, Turner P, Grunewald E, Zhang H, Butler JJ jr, Reboulet E, Knobbe S, Christy T, Lane JW jr, Johnson CD, Munday T, and Fitzpatrick A (2013). A Small-Diameter NMR Logging Tool for Groundwater Investigations. *Groundwater* 51: 914–926.
- Watt EL and Berens V (2011). Non-prescribed groundwater resources assessment – Alinytjara Wilurara Natural Resources Management Region. Phase 1 – Literature and Data Review, DFW Technical Report 2011/18, Government of South Australia, through Department for Water, Adelaide.
- Werner M, Dutch R, Pawley M, and Krapf C (2018). Amata Dolerite, Musgrave Province: connections to Neoproterozoic mantle plume magmatism within Rodinia. *MESA Journal* 87: 34–45.
- Woodhouse AJ, and Gum JC (2003). Musgrave Province — geological summary and exploration history, Report Book 2003/00021. Department of Primary Industries and Resources South Australia, Adelaide.
- Zonge International (2011a). NanoTEM: A very fast turn-off TEM system. Web source: http://www.zonge.com/PDF_Papers/Nano.pdf.
- Zonge International (2011b). GDP-32II Manual. Web source: <http://www.zonge.com/RxManuals.html>.



The Goyder Institute for Water Research is a partnership between the South Australian Government through the Department for Environment and Water, CSIRO, Flinders University, the University of Adelaide, and the University of South Australia.